| REPORT DOCUMENTATION PAGE | Form Approved OMB No. 0704-0188 |
|---|---|

Public reporting burden for this collection of information is estimated to average 1 hour per response, including the time for reviewing instructions, searching existing data sources, gathering and maintaining the data needed, and completing and reviewing the collection of information. Send comments regarding this burden estimate or any other aspect of this collection of information, including suggestions for reducing this burden, to Washington Headquarters Services, Directorate for Information Operations and Reports, 1215 Jefferson Davis Highway, Suite 1204, Arlington, VA 22202-4302, and to the Office of Management and Budget, Paperwork Reduction Project (0704-0188), Washington, DC 20503.

| 1. AGENCY USE ONLY *(Leave blank)* | 2. REPORT DATE | 3. REPORT TYPE AND DATES COVERED | |
|---|---|---|---|
| | September 1997 | Final Technical Report | 1 Jul 94 to 30 Jun 97 |

**4. TITLE AND SUBTITLE**
Experimental and Numerical Studies of Unsteady Heat Transfer in a Transonic Turbine

**5. FUNDING NUMBERS**
F49620-94-1-0367

**6. AUTHOR(S)**
Professor Wing Ng

**7. PERFORMING ORGANIZATION NAME(S) AND ADDRESS(ES)**
Virginia Polytechnic Institute & State Univ
Department of Mechanical Engineering
Blacksburg, VA 24061-0238

**8. PERFORMING ORGANIZATION REPORT NUMBER**

**9. SPONSORING/MONITORING AGENCY NAME(S) AND ADDRESS(ES)**
AFOSR/NA
110 Duncan Avenue, Rm B115
Bolling AFB, DC 20332-8050

**10. SPONSORING/MONITORING AGENCY REPORT NUMBER**
F49620-94-1-0367

**11. SUPPLEMENTARY NOTES**

19971119 064

**12a. DISTRIBUTION AVAILABILITY STATEMENT**
Approved for public release; unlimited distribution.

**12b. DISTRIBUTION CODE**

**13. ABSTRACT** *(Maximum 200 words)*

The effects of a shock wave passing through a blade passage on surface heat transfer to turbine blades were measured experimentally. The experiments were performed in a transonic linear cascade which matched engine Reynolds number, Mach number, and shock strength. Unsteady heat flux measurements were made with Heat Flux Microsensors on both the pressure and suction surfaces of a single blade passage. Unsteady static pressure measurements were made using Kulite pressure transducers on the blade surface and end walls of the cascade. The experiments were conducted in a stationary linear cascade of blades with heated transonic air flow using a shock tube to introduce shock waves into the cascade.

A time-resolved model based on conduction in the gas was found to accurately predict heat transfer due to shock heating measured during experimental tests without flow. The model under-predicted the experimental results with flow, however, by a factor of three. The heat transfer increase resulting from shock passing in heated flow averaged over 200 us (typical blade passing period) was found to be a maximum of 60% on the pressure surface near the leading edge. Based on experimental results at different flow temperatures, it was determined that shock heating has the primary effect on heat transfer, while heat transfer increase due to boundary layer disturbance is small.

**14. SUBJECT TERMS**

**15. NUMBER OF PAGES**
267

**16. PRICE CODE**

| 17. SECURITY CLASSIFICATION OF REPORT | 18. SECURITY CLASSIFICATION OF THIS PAGE | 19. SECURITY CLASSIFICATION OF ABSTRACT | 20. LIMITATION OF ABSTRACT |
|---|---|---|---|
| Unclassified | Unclassified | Unclassified | UL |

Standard Form 298 (Rev. 2-89) (EG)
Prescribed by ANSI Std. 239.18
Designed using Perform Pro, WHS/DIOR, Oct 94
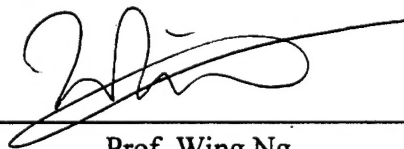
# Final Technical Report

AASERT Grant Number: F49620-94-1-0367

Funding Period: July 1, 1994 to June 30, 1997

Grant Title:

## Experimental and Numerical Studies of Unsteady Heat Transfer in a Transonic Turbine

Principle Investigators

Prof. Wing Ng
Chris Kraft Professor of Engineering
Virginia Tech
Department of Mechanical Engineering
Blacksburg, VA 24061-0238
540-231-7274
Fax 540-231-9000
email: wng@vt.edu

September 1997

# Effects of Shock Wave Passing on Turbine Blade Heat Transfer in a Transonic Turbine Cascade

by

Andrew Carl Nix

Dr. Thomas E. Diller and Dr. Wing F. Ng, Co-chairmen

Mechanical Engineering

(ABSTRACT)

The effects of a shock wave passing through a blade passage on surface heat transfer to turbine blades were measured experimentally. The experiments were performed in a transonic linear cascade which matched engine Reynolds number, Mach number, and shock strength. Unsteady heat flux measurements were made with Heat Flux Microsensors on both the pressure and suction surfaces of a single blade passage. Unsteady static pressure measurements were made using Kulite pressure transducers on the blade surface and end walls of the cascade. The experiments were conducted in a stationary linear cascade of blades with heated transonic air flow using a shock tube to introduce shock waves into the cascade.

A time-resolved model based on conduction in the gas was found to accurately predict heat transfer due to shock heating measured during experimental tests without flow. The model under-predicted the experimental results with flow, however, by a factor of three. The heat transfer increase resulting from shock passing in heated flow averaged over 200 $\mu$s (typical blade passing period) was found to be a maximum of 60% on the pressure surface near the leading edge. Based on experimental results at different flow temperatures, it was determined that shock heating has the primary effect on heat transfer, while heat transfer increase due to boundary layer disturbance is small.

# Acknowledgments

I would like to take this opportunity to thank all the people who contributed to my graduate studies and research and have made my time at Virginia Tech a rewarding experience. First, I would like to express special thanks to the faculty of my research group, Dr. Wing F. Ng, Dr. Tom Diller, and Dr. J. Schetz. The combination of these three minds contributed greatly not only to my research, but to my overall learning experience and intellectual growth. Their combined experience and wealth of information in fluid mechanics, heat transfer, and turbomachinery was invaluable in my research. I am sincerely grateful to Dr. Ng and Dr. Diller for their invaluable guidance and advice in my graduate studies and future plans. In addition, I would like to thank Dr. Clinton L. Dancey for agreeing to serve on my graduate advisory committee. My knowledge of compressible flow stems mainly from Dr. Dancey's instruction.

I would also like to thank the graduate students composing the workhorse of our research group, Angela Wesner, David Holmberg, Jamie Hale, and Terry Reid. Their help and support in getting up to speed with the test facility and instrumentation, and their support in completing my research is greatly appreciated. Special thanks goes to Hume Peabody and Billy Ambrose for their help in taking the data for this thesis. Their willingness to help me in the tunnel (and change diaphragms in the shock tube) at all hours of the day and for their support and close friendship is worth more than words can express. Also, I would like to thank my friends, and officemates, Tom Leitch, Kevin Miller, David White, Todd Ninneman, Joe Cahill, Jeremy Chan, Randy Hibshman, and Chris Saunders. They made my graduate studies more enjoyable and provided me with more than a few diversions from my studies.

I am eternally grateful to my parents, Bob and Pat, and my brother Mike, whose emotional and financial support throughout my undergraduate and graduate studies have made everything possible. Finally, and most importantly, I would like to thank my girlfriend and best friend, Cheryl Gaumer, whose love and support have helped me through difficult times.

# Table of Contents

# List of Illustrations

# List of Tables

# List of Symbols

$c_{ax}$      blade axial chord

$E_p$      pressure transducer voltage output

$E_q$      heat flux sensor voltage output

$E_{ref}$      reference voltage

$E_T$      temperature sensor voltage output

$E_{TT}$      total temperature probe voltage output

$E_{PT}$      total pressure gage voltage output

$f$      frequency

$G_p$      pressure transducer gain

$G_q$      heat flux sensor gain

$G_T$      temperature sensor gain

$h$      convection heat transfer coefficient

$I$      current

$k$      thermal conductivity

$M$      Mach number

$p$      pressure

$q''$      heat flux

$q''_f$      heat flux due to flow temperature difference

$q''_s$      heat flux after shock passing

$q''_g$      predicted gage heat flux response

$q''_s$      theoretical model heat flux

$r$      recovery factor

$R$      ideal gas constant

$R_{ref}$      reference resistance

$S$      heat flux gage sensitivity

$S_p$      pressure transducer sensitivity

| St | Strouhal number |
|----|-----------------|
| t | time |
| T | temperature |
| $T_r$ | recovery temperature |
| TR | temperature ratio of shock |
| $U_\infty$ | freestream velocity |
| V | velocity |
| $V_s$ | shock velocity |
| V' | velocity in transformed reference frame |
| W | blade inlet relative velocity |
| x | horizontal direction component |
| y | vertical direction component |

## Greek symbols

| $\alpha$ | thermal diffusivity |
|----------|---------------------|
| $\delta$ | thickness of resistance layer |
| $\gamma$ | specific heat ratio |
| $\nu$ | kinematic velocity |
| $\pi$ | Pi |
| $\rho$ | density |
| $\tau$ | time constant of gage |

## Superscripts

| - | averaged |
|---|----------|

## Subscripts

| | |
|---|---|
| 1 | gage location 1 |
| 2 | gage location 2 |
| 3 | gage location 3 |
| 4 | gage location 4 |
| a | ambient conditions |
| BL | refers to boundary layer |
| f | refers to flow |
| s | refers to shock |
| T | total conditions |
| w | state at wall |
| $\infty$ | stagnant gas property |

# Chapter 1.0

## Introduction

### 1.1 Turbine Blade Heat Transfer

The efficiency of gas turbine engines due to unsteady flow conditions is of particular importance in current research efforts. Improvements in the efficiency of gas turbines under steady flow conditions have been studied extensively, however, the effects of unsteady phenomena such as freestream turbulence, wake impingement, and shock wave passing on gas turbine performance have begun to draw considerable attention. Recent research has suggested that significant fluctuations in heat transfer exist due to freestream turbulence and the impingement of wakes and shock waves from upstream blade rows. Understanding of the unsteady flow field and its effects on heat transfer in high pressure gas turbine stages are, therefore, of utmost importance.

Increasing the efficiency of gas turbines and the thrust to weight ratio increases the thermal loads and thermal stresses on the blading in the turbine section due to higher combustor temperatures. Higher combustor temperatures increase the heat transfer between the flow through the turbine and the turbine blades. The increase in thermal load then makes it necessary to understand the effects that unsteady flow phenomena have on the heat transfer in the turbine. Predicting blade temperatures in the high pressure turbine stages, where hot combustor gases enter the turbine, is of primary importance. These blades operate near their thermal limits, and any increase in blade temperature due to unsteady flow phenomena needs to be quantified. Analysis of the heat transfer increase due to unsteady flow phenomena in these stages will help in prediction of blade temperatures. Cooling schemes can then be implemented to decrease blade temperatures, therefore decreasing the thermal loads and stresses on the turbine blading and avoiding engine failure. Blade cooling schemes were first implemented in the early 1950's (Hale, 1996). The use of blade cooling schemes in conjunction with advances in blade materials

has allowed the gas temperature at the inlet to the high pressure turbine to increase from approximately 1050 K in the 1950's to approximately 1800 K in the 1980's (Sieverding, 1995).

The unsteady flow factors which affect turbine blade heat transfer, as mentioned earlier, include freestream turbulence, wakes, and shock waves generated by upstream blade rows. Of particular importance is the effects which shock waves passing through the turbine blade passages have on heat transfer to the turbine blading. Studies have been performed which focus on the effects that shocks coupled with wakes have on turbine blade heat transfer by passing a rotating bar along the leading edge of a cascade of turbine blades. However, to date, studies which uncouple the effects of wake passing and shock impingement on turbine blade heat transfer have not been performed.

## 1.2 Objective

Testing of gas turbine heat transfer using instrumentation mounted into an actual high pressure turbine is difficult and is complicated by the rotating blade rows and extreme temperatures. Experimentation is therefore performed in either rotating rigs or stationary cascades with conditions (Reynolds number, Mach number, and temperature ratios) similar to those seen in an actual working gas turbine. The focus of this thesis is the measurement of the time-resolved heat flux resulting from weak shock waves passing through the blade rows in a stationary, linear turbine cascade. The cascade of turbine blades is subjected to a moving shock wave propagating tangentially along the leading edge of the cascade (Figure 1.1). This simulates the interaction between an upstream nozzle guide vane and a downstream rotor in a stage or the interaction between a rotor and downstream stator in successive turbine stages (Figure 1.2). The common method for producing shocks for cascade tests is to pass a rotating bar along the leading edge of the cascade. This method, however, introduces wakes in addition to shock waves. The shock waves in the present work were produced using a shock tube and shock shaper

**From Shock Tube**

**Moving Shock**

**Inlet Flow**

**Exhaust**
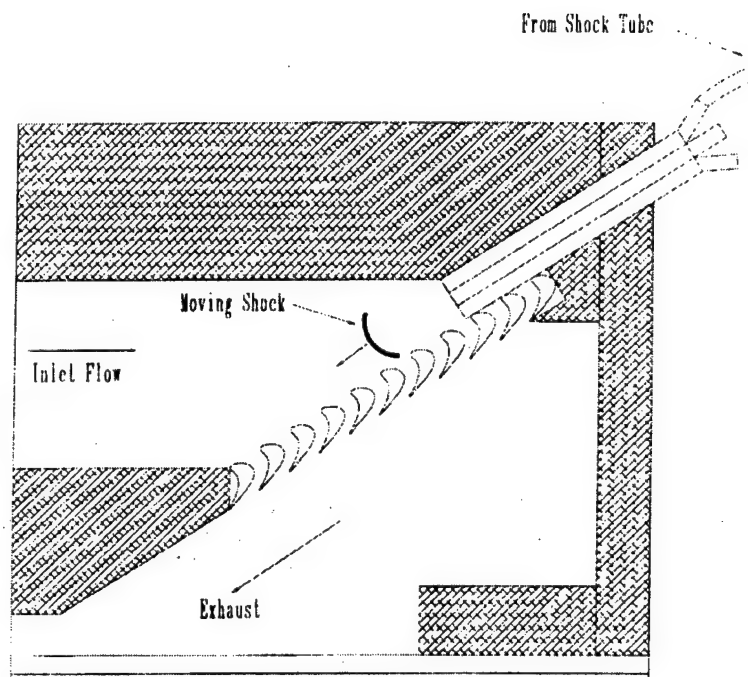
Figure 1.1  Schematic of Shock Wave Moving through Cascade
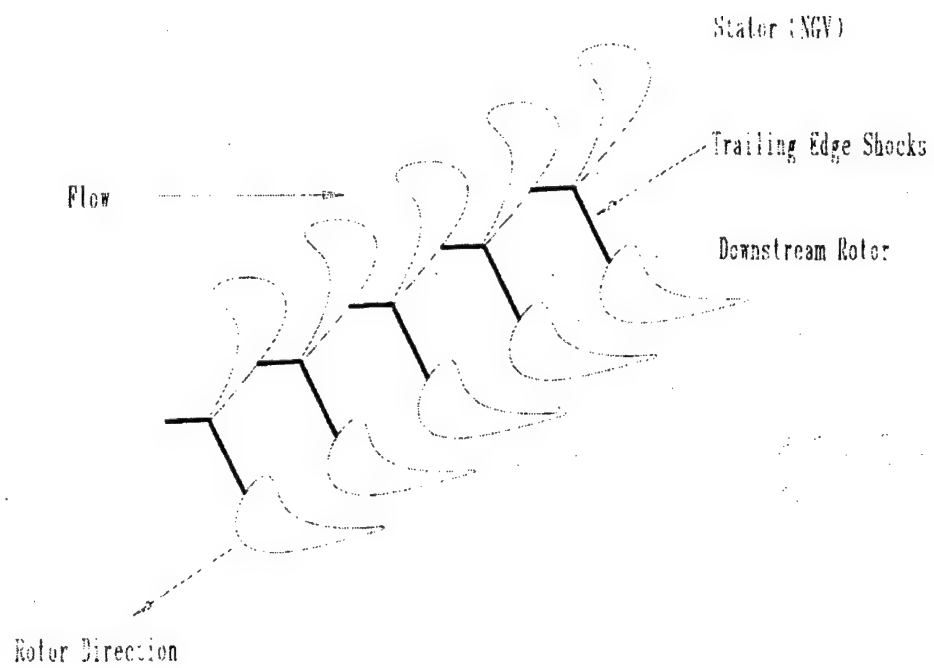
Figure 1.2  Shock Interaction between NGV (or Stator) and Rotor

configuration. The shock shaper is responsible for changing the geometry of the shock wave introduced into the test section such that it is a roughly planar shock. This configuration has the advantage of allowing an isolated shock wave to be introduced into the cascade without a wake present as seen in the rotating bar mechanism.

Unsteady blade surface heat flux and temperature measurements were made using new thin film gages. The gage used was the Heat Flux Microsensor (HFM-6) manufactured by Vatell Corporation. The HFM gage is capable of measuring both heat flux and surface temperature simultaneously, at frequencies of up to 100 kHz. The heat flux sensors were located at four positions in a single blade passage, one on the suction surface and three on the pressure surface. The new thin film heat flux microsensor is described in detail in Chapter 2, along with background on previous studies and moving shock theory. The blow down test facility, cascade and test section, instrumentation, data acquisition system, and testing and data reduction procedures are described in detail in Chapter 3. A theoretical model developed for this work to predict unsteady heat transfer due to shock wave passing (or impingement) is presented in Chapter 4. Experimental data analysis and results are presented in detail in Chapter 5. Chapter 6 provides a detailed discussion of the results. Chapter 7 contains conclusions and recommendations for future work. The appendices contain data plots for each individual run, computer programs, and a detailed analysis of the progression of shock waves and reflections through the turbine cascade blade passages.

# Chapter 2.0

## Background

### 2.1 Previous Studies

In the last decade, researchers have been focusing on understanding shock wave progression through turbine cascades and analyzing the unsteady effects of shock waves on heat transfer in gas turbines. The majority of the studies to date have employed a high speed rotating disk with radial bars attached to the circumference which pass along the leading edge of a turbine cascade to produce shocks and wakes. This rotating bar mechanism simulates the effects of a nozzle guide vane (NGV) on the downstream rotor. This mechanism, however, cannot produce shocks independent of wakes generated by the rotating bars.

Oxford researchers, Doorly and Oldfield (1985) employed the rotating bar mechanism to study the effects of isolated wakes and weak shock waves on rotor heat transfer. Their primary findings were that shock-boundary layer interaction did not have a direct effect on heat transfer. Instead, they reported that the incident shock wave produces a separation "bubble" which forms near the leading edge of the suction surface and collapses after propagating a short distance along the suction surface. They concluded that the disintegration of this separation bubble produces a turbulent patch which is responsible for fluctuations in transient heat transfer as it is swept down the boundary layer. They also concluded that successive disturbances may eventually merge, forming a continuously turbulent boundary layer.

Ashworth, et al. (1985) conducted experiments with a rotating bar mechanism which produced stronger shock waves (blade relative Mach number of 1.165). They reported the shock waves, coupled with wakes, to have a profound effect on suction surface heat transfer along approximately 35% of the blade from the leading edge. The

heat transfer increase was thought to be caused by separation and reattachment of the boundary layer as a result of shock impingement. The increase in heat transfer caused by this separation-reattachment process was shown to be preceded by a decrease in heat transfer from the mean level, however, the cause of this effect was not identified.

Johnson et al. (1989) studied surface heat transfer fluctuations on turbine rotor blades due to upstream shock passing using a rotating bar mechanism. They developed a theoretical model for predicting the unsteady heat transfer due to a step change in gas temperature resulting from shock wave passing using theory for one-dimensional unsteady heat transfer in solids. They identified five mechanisms by which the shock waves affect rotor blade surface heat transfer. The two primary mechanisms they identified were shock heating (increase in heat transfer due to shock temperature ratio) and boundary layer disruption. They suggested that the shock wave compresses the boundary layer, increasing the pressure gradient and thus increasing the temperature gradient and subsequent heat transfer. These two effects, shock heating and boundary layer modulation, were assumed to be additive to give the total increase in heat transfer due to shock wave passing. They also concluded that the effects of shock passing on heat transfer will persist until the arrival of the next rotating bar shock wave.

Numerical work by Saxer and Felici (1994) focused on three-dimensional hot streak migration and shock interaction in a rotor passage. The numerical work tracked the progression of gas hot streaks caused by shock passing in the blade passage. Numerical results determined that the increase in time averaged rotor stagnation temperature was larger on the pressure side than on the suction side of the passage.

## 2.2 Moving Shock Theory

In order to simplify later discussion of shock progression, pressure ratios, and temperature ratios, a brief overview of moving shock theory will be discussed.

Shock waves are essentially discontinuities in flow properties of infinitesimal thickness (Zucker, 1977). The thickness of shock waves has been shown through experiments to be on the order of a few mean free molecular path lengths (Shapiro, 1954). In other words, the properties of a moving fluid change from one value to the next discontinuously. This discontinuity is then a shock process. The process of moving across a standing normal shock is non-isentropic. Only one fluid property remains constant across a normal shock, the total temperature ($T_t$), and, assuming constant specific heats, the total enthalpy ($h_t$). A complete discussion of the physics of shock waves through the analysis of continuity, and conservation of energy and momentum will not be discussed here, rather the equations for calculating the fluid properties across a shock wave will be presented. The governing equations for a standing normal shock wave for a perfect gas are as follows:

$$\frac{p_1 M_1}{\sqrt{T_1}} = \frac{p_2 M_2}{\sqrt{T_2}} \qquad [2.1]$$

$$TR \text{ (Temperature Ratio)} = \frac{T_2}{T_1} = \frac{\left[1 + \frac{(\gamma - 1)}{2} \cdot M_1^2\right]}{\left[1 + \frac{(\gamma - 1)}{2} \cdot M_2^2\right]} \qquad [2.2]$$

$$PR \text{ (Pressure Ratio)} = \frac{p_2}{p_1} = \frac{\left[1 + \gamma \cdot M_1^2\right]}{\left[1 + \gamma \cdot M_2^2\right]} \qquad [2.3]$$

where p is the static pressure of the flow, T is the static temperature of the flow, M is the Mach number of the flow, and $\gamma$ is the specific heat ratio of the gas. The subscripts, 1 and 2, refer to the state before and after the shock wave, respectively. These equations can be solved if either the state before or after the shock (p, T, and M) is known and at least one

property is known on the other side of the shock. Analysis of moving shock waves can be simplified such that standing, normal shock equations can be used as follows:

Figure 2.1 (taken from Zucker, 1977) shows a moving shock traveling into standard sea level air in the same direction as the flow with the ground as a reference point. In order to transform this picture such that we can apply standing normal shock equations, a flow field of velocity $V_s$ (velocity of the moving shock wave) is superimposed to the right. An alternative way of accomplishing this is to move the reference point from the ground and "ride along" with the shock wave. Figure 2.2 (taken from Zucker, 1977) demonstrates the results of transforming the frame of reference in this way. What is left is a standing normal shock. The normal shock equations presented earlier can then be used by adding the following equations:

$$V_2' = V_s - V_2 \qquad\qquad [2.4]$$

$$M = \frac{V}{\sqrt{\gamma RT}} \qquad\qquad [2.5]$$

where $V_2$ is the velocity behind the shock, $V_2$' is the velocity behind the shock in the transformed reference frame, M is the Mach number, and T is the static temperature at one state for the flow. R and $\gamma$ are the ideal gas constant and specific heat ratio of the gas, respectively. Using the above equations and changing the reference frame of the shock wave allow the properties of the flow across a moving shock wave to be calculated, including the pressure and temperature ratios of the moving shock. The shock waves seen in this work, due to their curvature, are not one-dimensional; however, to simplify analysis, they were assumed to be roughly one-dimensional for a small segment.

A useful tool for visualizing shock waves is through the use of flow visualization techniques. Two common forms of flow visualization which capture changes in density

$$V_s = 1800 \text{ ft/sec}$$

Moving shock

$p_1 = 14.7$ psia
$T_1 = 520\,^{\circ}\text{R}$
$V_1 = 0$

$p_2 = ?$
$T_2 = ?$

$V_2 = ?$
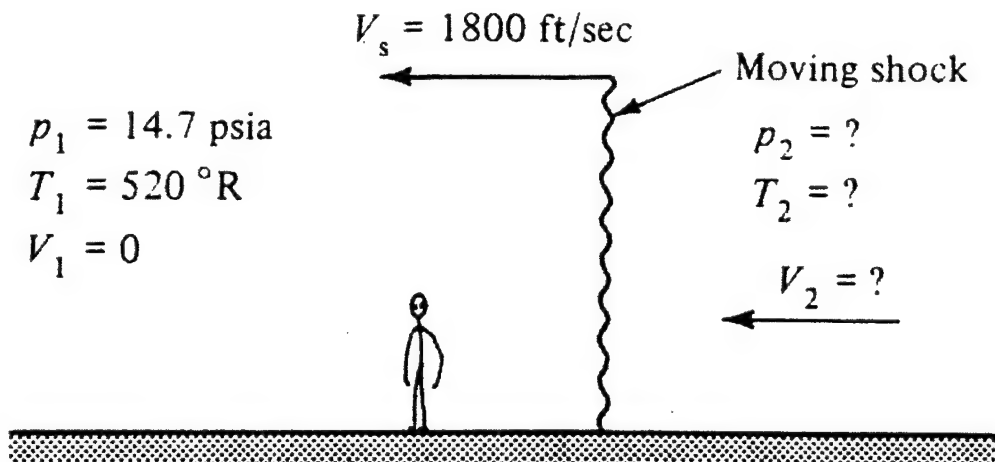
Figure 2.1  Moving Normal Shock with Ground (Lab) as Reference

Standing normal shock

$p_{1'} = 14.7$ psia
$T_{1'} = 520\,^{\circ}\text{R}$
$V_{1'} = V_s = 1800$ ft/sec

$p_{2'} = ?$
$T_{2'} = ?$
$V_{2'} = V_s - V_2$
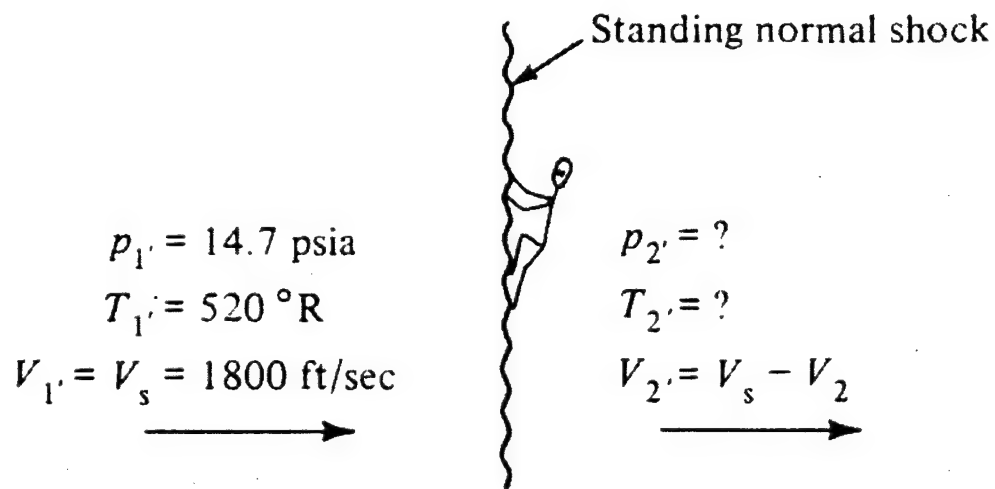
Figure 2.2  Moving Normal Shock Transformed into Stationary Shock

are Schlieren photographs and shadowgraphs. The technique used in the present research was the shadowgraph technique. The procedure and set-up for producing flow shadowgraphs is described in Shapiro (1953). Figure 2.3 shows a shadowgraph of a moving shock and reflections of this shock as they propagate through a blade passage in the cascade. The shock and reflections are seen as dark lines where there is a discontinuity in the density field of the flow. The use of these shadowgraphs allowed the progression of shock waves in the test section to be analyzed as an aid in interpreting pressure and heat flux data.

## 2.3 High Speed Flow Heat Transfer

In order to analyze effects of shock wave passing on unsteady heat transfer in the blade passage it is necessary to define and calculate a temperature difference driving the heat transfer before the shock passing. For low speed flows, the boundary layer energy equation in terms of enthalpy is:

$$\rho \cdot \left( u \frac{\partial h_f}{\partial x} + v \frac{\partial h_f}{\partial y} \right) = k \frac{\partial^2 T}{\partial y^2}$$  [2.6]

where $h_f$ is the enthalpy of the flow, u is the velocity in the x direction, v is the velocity in the y direction, and k is the thermal conductivity of the fluid. For compressible, high speed flows, the kinetic energy of the flow becomes important and the total enthalpy is used. Also, due to the speed of the flow, frictional heating can be significant and the viscous dissipation term must be considered. The energy equation in terms of total enthalpy for high speed flows then becomes:

$$\left( u \frac{\partial h_t}{\partial x} + v \frac{\partial h_t}{\partial y} \right) = \alpha \frac{\partial^2 h_t}{\partial y^2} + v \frac{\partial^2}{\partial y^2} \left( \frac{u^2}{2} \right) \left( 1 - \frac{1}{Pr} \right)$$  [2.7]
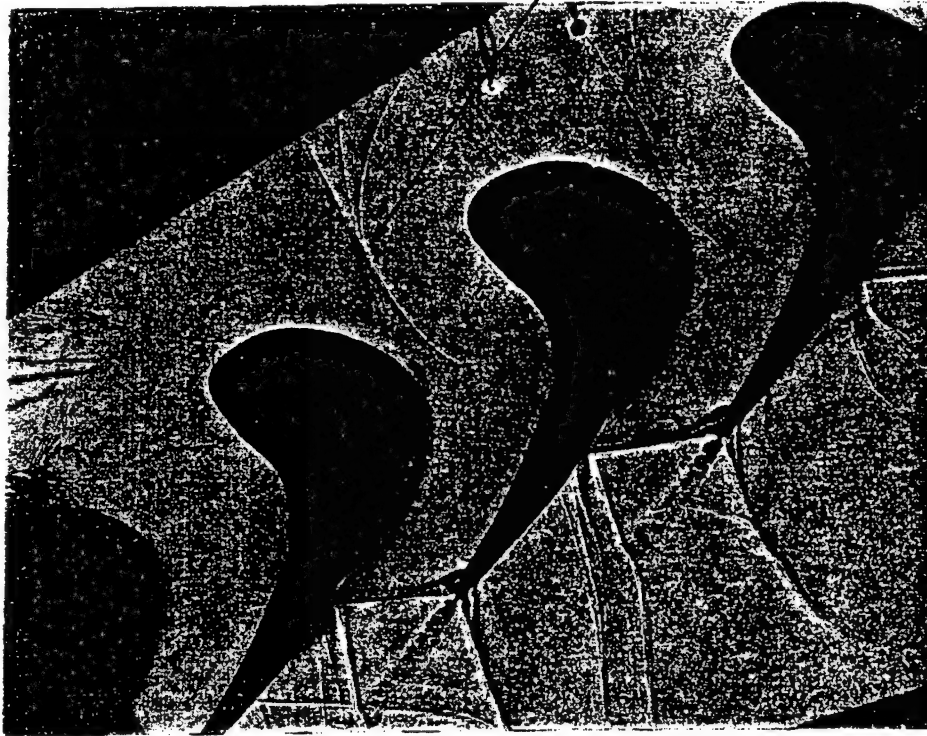
Figure 2.3  Flow Shadowgraph Picture in Cascade

where $h_t$ is the total enthalpy of the flow, $\alpha$ is the thermal diffusivity of the gas, $\nu$ is the kinematic viscosity of the flow, and $Pr=\nu/\alpha$ is the Prandtl number. When $Pr=1$, the last term goes to zero and the energy equation is the same as the low speed equation and heat transfer between the air and the blades would be the same whether the flow total temperature or static temperature were used:

$$q'' = h \cdot (T_\infty - T_s) = h \cdot (T_t - T_s) \qquad [2.8]$$

where h is the convection heat transfer coefficient, $T_t$ is the total temperature of the flow, $T_\infty$ is the flow static temperature, and $T_s$ is the surface temperature of the blades (measured at each gage location). When the Prandtl number is not equal to one $(Pr \neq 1)$ then a proper temperature must be defined for the flow. The temperature typically used is the adiabatic wall or recovery temperature $(T_r)$. The recovery temperature is the temperature the wall would attain if q"=0. The heat transfer is then given by:

$$q'' = h \cdot (T_r - T_s) \qquad [2.9]$$

The recovery temperature $(T_r)$ is calculated using:

$$T_r = T_\infty + r \cdot \frac{U_\infty^2}{2 \cdot C_p} \qquad [2.10]$$

where $U_\infty$ is the freestream velocity of the flow, and r is the recovery factor. The recovery factor for laminar flows is approximated by $r = \sqrt{Pr}$, while $r = Pr^{1/3}$ for turbulent flow. The recovery temperature can be calculated using the flow total temperature and the Mach number to find the freesteam velocity, $U_\infty$. Using the total temperature, the static temperature can be calculated using:

$$T_\infty = \frac{T_t}{\left[1 + \frac{\gamma - 1}{2} M^2\right]} \qquad [2.11]$$

where $\gamma$ is the specific heat ratio of the gas and M is the mach number of the flow at each gage location. The Mach numbers determined for the flow in the cascade used in the present research are shown in Table 2.1:

Table 2.1  Mach Numbers at Gage Locations

| Gage Number | #1 (Suction) | #2 (Pressure) | #3 (Pressure) | #4 (Pressure) |
|---|---|---|---|---|
| Mach Number | 0.52 | 0.25 | 0.209 | 0.32 |

Using the static temperature, $T_\infty$, and the Mach number, the freestream velocity, $U_\infty$, can be calculated at each gage location using:

$$U_\infty = M \cdot \sqrt{\gamma R T_\infty} \qquad [2.12]$$

Using these equations for compressible flow and high speed flow heat transfer, the temperature difference for the flow ($\Delta T_f = T_r - T_s$) at each gage location can then be calculated.

## 2.4  Heat Flux Microsensor

Recent studies and advances in heat flux measurement have resulted in the development of a new thin film heat flux sensor. The gage operates by measuring the transient temperatures on the surfaces of a thermal resistance layer placed on a substrate (Figure 2.4). If the thermal properties of the resistance layer and substrate are known, the surface heat flux can be determined since the difference between the two surface
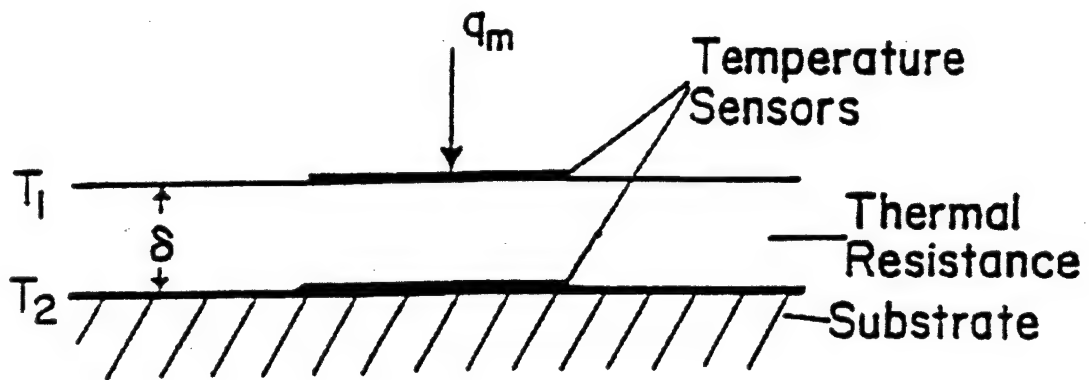
Figure 2.4  Resistance Layer for Heat Flux Gage

temperatures is directly proportional to the heat flux. The microsensor is produced by fabricating a thermal resistance layer with thermocouples on either side. The microfabrication techniques used to produce the gage are discussed in detail by Hager et al. (1991a). Using microfabrication allows a thermal resistance layer of less than 1 μm to be deposited on the substrate. This very thin resistance layer allows a fast time response and greatly reduces the possibility of disruption of the physical and thermal properties of the surface, even for very high heat flux levels. However, the temperature differences measured across the resistance layer are typically very small. The voltage signal is therefore amplified by connecting many thermocouple pairs in series across the resistance layer, creating a differential thermopile which will produce a measurable signal (Figure 2.5). The heat flux gage actually consists of two different sensors, a heat flux sensor (HFS) and resistance temperature sensor (RTS). The HFS sensor described above is surrounded by a sensor which measures surface temperature from the electrical resistance of the sensor material.

Thin film gages have been used successfully by many researchers to make high frequency heat flux measurements. Transient heat transfer measurements in shock-boundary layer interaction in supersonic flow were made using thin film gages by Hayashi et al. (1989). Holmberg and Diller (1995) made heat transfer measurements in a shock tunnel and determined the time response for the heat flux microsensor to be approximately 6 μs (better than 100 kHz frequency response). Simmons et al. (1991) measured time-resolved surface heat flux due to freestream turbulence at the stagnation point of a cylinder. Johnson and Diller (1995) measured the effects of freestream turbulence on the surface heat transfer of turbine blades in a stationary cascade. Other studies of thin film heat flux gage measurements and calibration are presented in Hager et al. (1991b), Baker and Diller (1993), and Diller (1993).

Lead
Connection

Lower
Thermocouple

Upper
Thermocouple

Thermal
Resistance
Layers
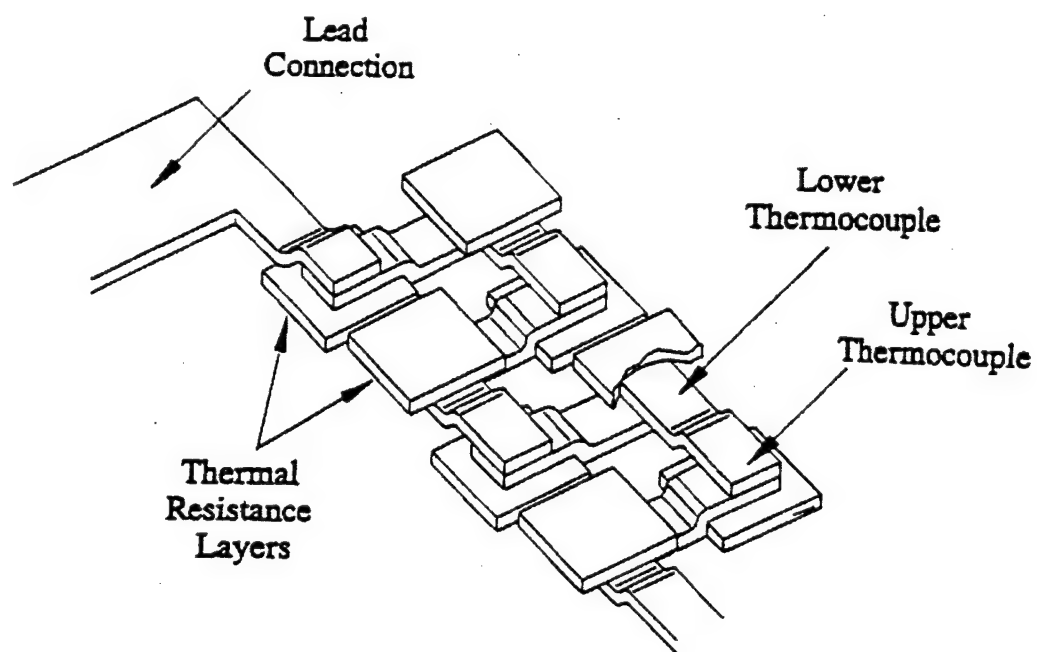
Figure 2.5  Detail of Heat Flux Sensor Thermopile

# Chapter 3.0

## Experimental Set-up and Procedure

This chapter provides a description of the test facilities, equipment, and procedure used to perform these experiments. The section is broken up into a description of the wind tunnel facility, test section and cascade, shock wave production setup, HFM-6 heat flux microsensors, Kulite pressure transducers, and data acquisition system and run procedure. Also included, is a description of the set-up used to do some simplified bench tests.

### 3.1 Wind Tunnel Test Facility

The experiments for this work were conducted in the Virginia Polytechnic Institute Cascade Wind Tunnel. The facility is a blow down wind tunnel which is capable of run times of approximately 40 seconds. The facility is capable of providing heated flow by way of a heating loop incorporated into the tunnel. Figure 3.1 shows a schematic of the wind tunnel facility and test section. Following is a description of the production of the air used in the facility and the path it takes through the facility.

The air to be used in the tunnel is compressed via a four stage reciprocating compressor with a heat exchanger to cool the air. The compressed air travels through an activated alumina drying unit which removes moisture and contaminants from the air before use in the tunnel. The compressed air is then stored in two large reservoir tanks awaiting introduction into the wind tunnel through 35.6 cm (14.0 in) diameter pipes. The air is compressed and stored in the tanks at a pressure of approximately 827 kPA (120 psig). The air travels through two valves, a safety valve which will trip and shut down tunnel operation when a gage pressure of 207 kPa (30 psig) is reached, and a control valve which controls tunnel inlet pressure. The control valve is manipulated via a BASIC
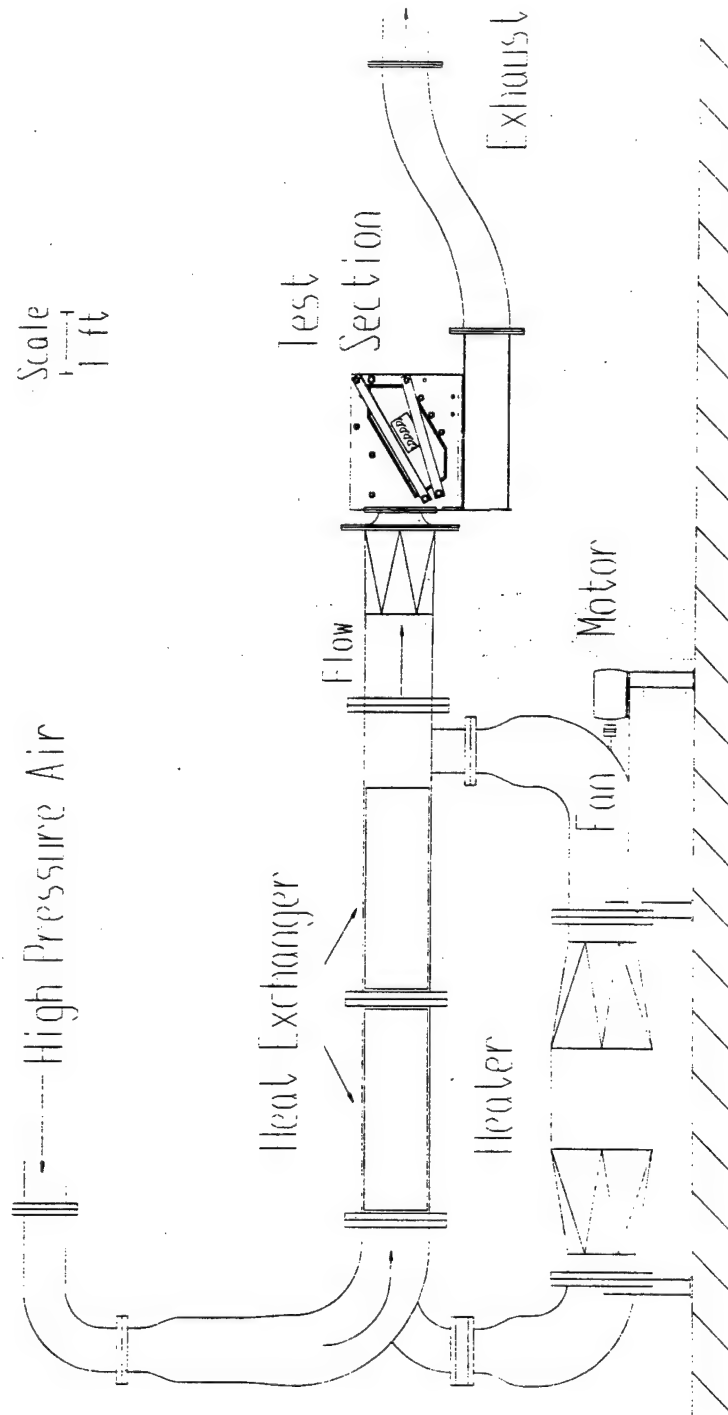
Figure 3.1 Virginia Tech Cascade Wind Tunnel

program which maintains a relatively constant total pressure in the test section throughout a single run based on feedback received from a pressure transducer located upstream of the test section. As pressure in the storage tanks decreases, the BASIC program actuates the control valve in order to maintain a constant total pressure at the tunnel inlet. The air then travels through a 90 degree bend and a flow straightener before entering the test section. The flow straightener also contains a heat exchanger consisting of an array of copper tubes, providing the option of heated or unheated runs. The flow is then introduced into the test section.

The heating loop upstream of the test section consists of two bundles of copper heat exchanger tubes, an electric heater, and an axial flow fan. When heated runs are desired, two manual valves are manipulated to allow heating of the copper heat exchanger tubes. The first valve is a flapper valve just upstream of the test section which cuts off any flow from the heating loop from entering the test section. The second valve is a butterfly valve which closes the heating loop off from the pipes connecting the tunnel to the storage tanks and completes a closed loop (Figure 3.2 and Figure 3.3). In order to charge the heat exchanger tubes, a 36 KW electric heater is turned on and an axial fan circulates the air through the heating loop at approximately 2 m/s. The heat from the circulating air is stored in the array of copper tubing, awaiting the inlet flow to the tunnel during a single run. Three thermocouples are located within the heating loop to monitor various temperatures. The temperature of the tubing is monitored by a type K thermocouple, the hot gas temperature in the loop is monitored by a type K air thermocouple probe, and a third thermocouple monitors the temperature of the electric heater. The type K air probe also monitors the total temperature of the inlet air during a run.

The process of heating the tubes in the heat exchanger in preparation for a run is as follows. The two manual valves are opened and closed, respectively, to isolate the

# Heat Exchanger Loop
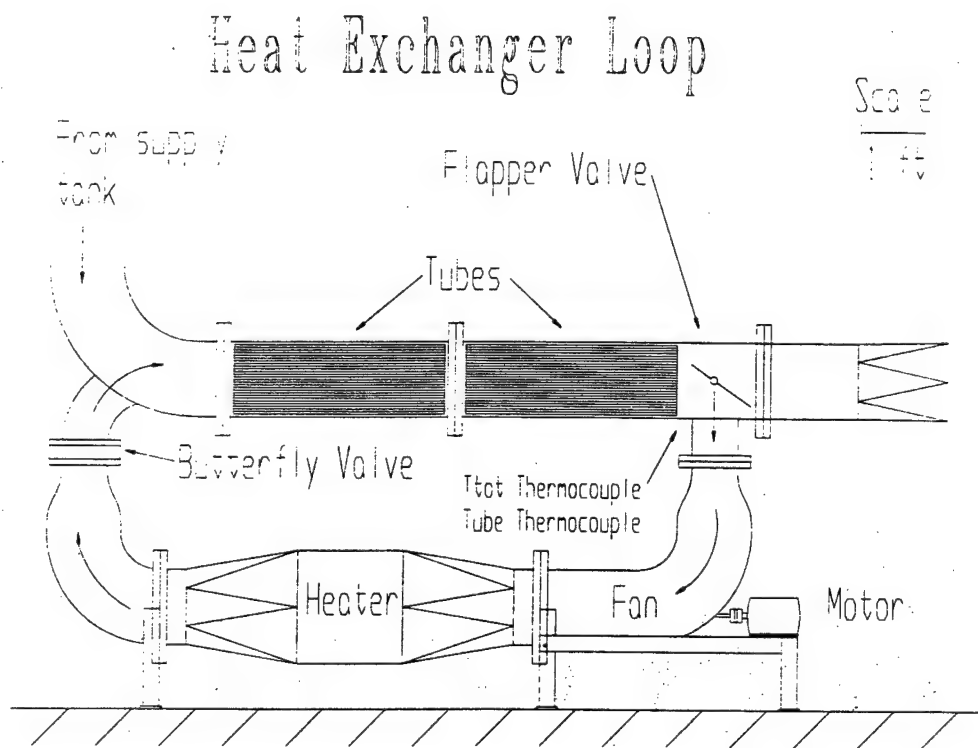


Figure 3.2  Wind Tunnel Heat Exchanger Loop Schematic
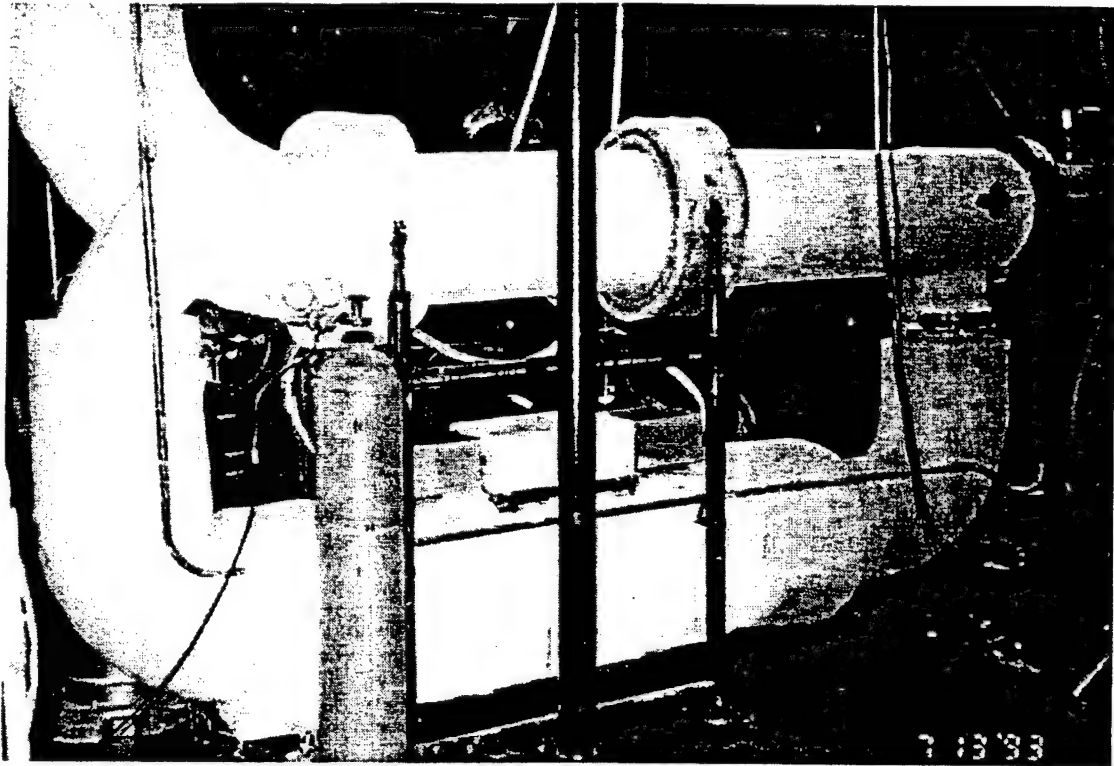
Figure 3.3  Wind Tunnel Heat Exchanger Loop Photo

heating loop from the rest of the facility. The fan and heater are turned on and allowed to run until the temperature of the heat exchanger tubes reach approximately 220°F (105°C). Once the tubes reach this temperature, the electric heater is turned off and the fan is left running to insure even distribution of heat through the heat exchanger tubes. Once the tube temperature reaches approximately 210°F (99°C), the fan is turned off and the two manual valves are closed and opened, respectively. This setup allows for flow temperatures of approximately 190°F (88°C). The flow from the heat exchanger and flow straightener enters the test section through a circular to rectangular transition piece.

The flow enters the test section and cascade at Mach 0.36, is accelerated as it is turned by the cascade blading, and exits the cascade at a design Mach number of 1.26. The air is then exhausted from the test section, passes through a diffuser and muffler and is vented to the atmosphere.

## 3.2 Test Section and Cascade

The turbine blade cascade used in the facility consists of 11 aluminum turbine blades supported by two Plexiglas end walls and two aluminum endblocks. The blading is held in place and stabilized between the endwalls using a pin and screw combination. Two grooved aluminum doors hold the endwalls in place within the test section. The doors are secured via two steel bars which are then bolted to the outside of the test section (Figure 3.4 and Figure 3.5). The aluminum doors have a rectangular opening which expose a section of the Plexiglas allowing for flow visualization techniques such as shadowgraphs to be employed in analyzing the flow and shock progression through the cascade. (Figure 3.6). The blades used in the cascade are 5.08 cm (2.0 in) in span and 4.5 cm (1.77 in) aerodynamic chord and are spaced 3.81 cm (1.5 in) apart. The blading is at an angle of 32 degrees to the inlet flow, allowing for a similar relative flow angle seen by moving turbine blading in a real gas turbine. Instrumentation is located in the middle (approximately midspan) of the blades in the centermost blade passage to avoid any
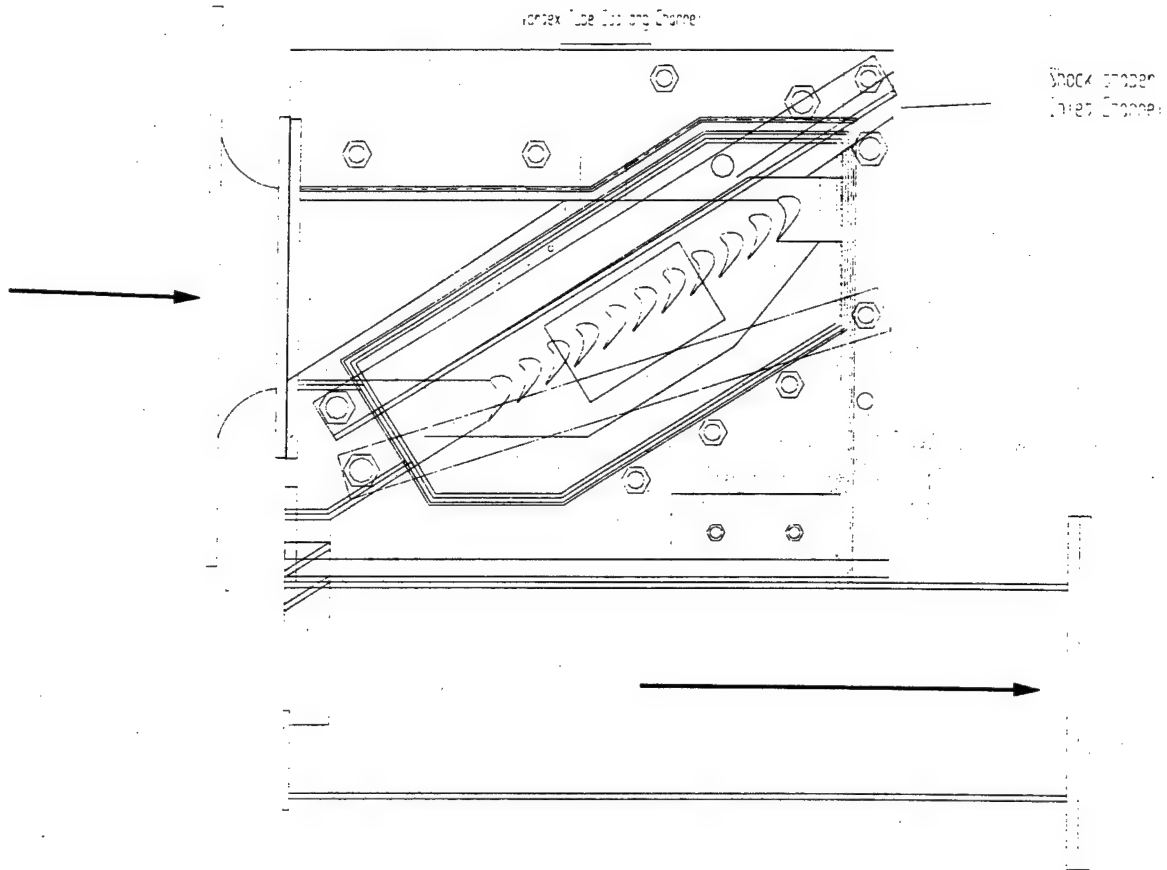
Figure 3.4  Wind Tunnel Test Section and Cascade
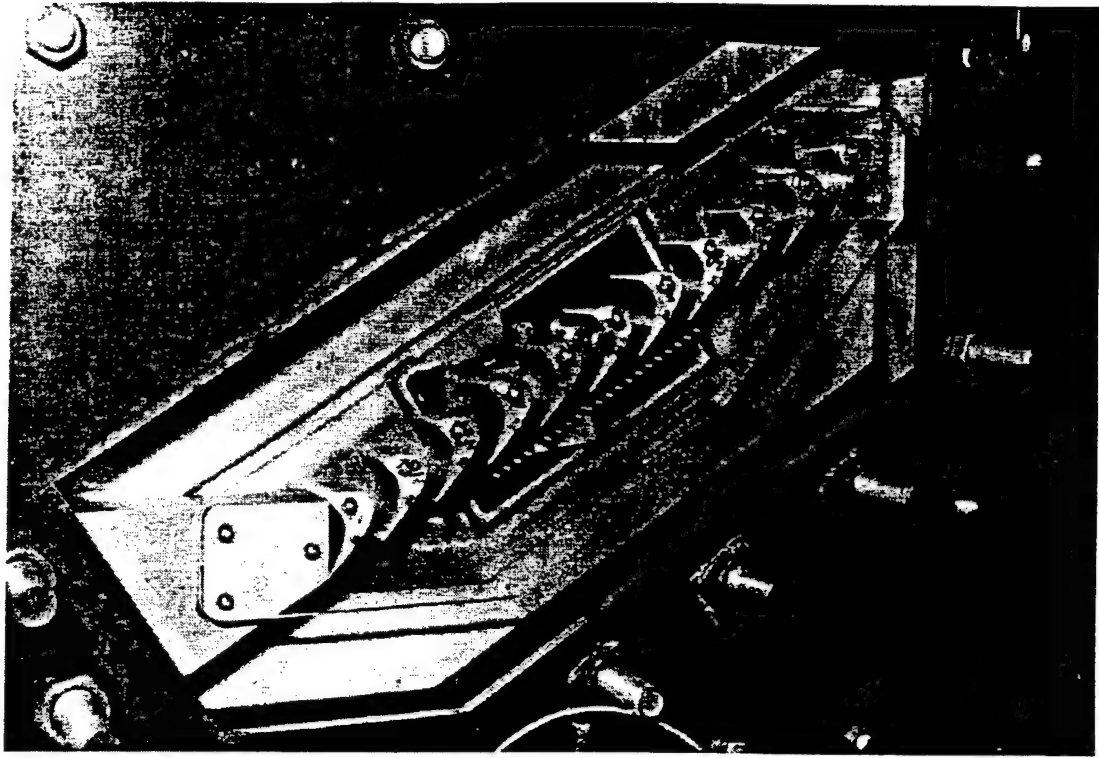
Figure 3.5  Wind Tunnel Cascade Photo
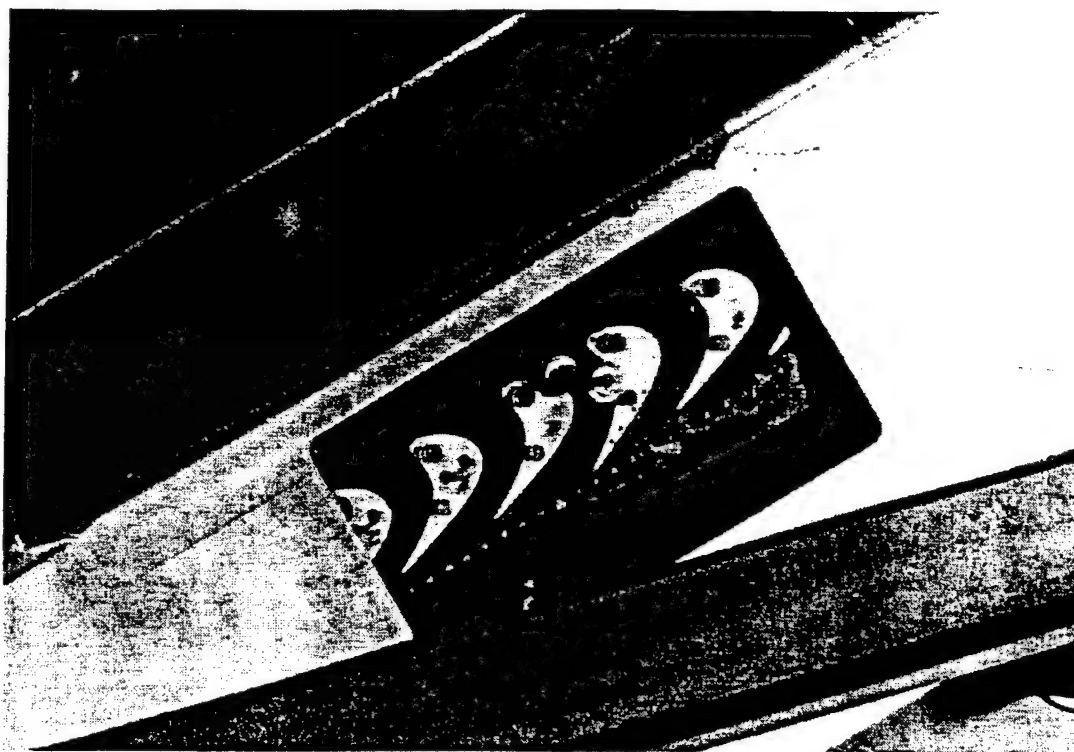
Figure 3.6  Flow Visualization Windows in Test Section

effects from the endwalls. The test section is equipped with a vortex cooling tube in order to cool the test section and blades between heated runs. The far end of the test section contains an opening for the insertion of a shock shaper which introduces a moving shock into the cascade (Figure 3.7).

## 3.3 Shock Tube and Shaper

The production and introduction of a moving shock into the test section is accomplished via a shock tube and shock shaper. The shock tube (Figure 3.8) is a 4.57 m (15.0 ft) long section of heavy duty schedule 120 steel consisting of two sections, a driver section and a driven section. The driver section is 1.52 m (5 ft) in length and the driven section is 3.05 m (10.0 ft). The two sections are connected by standard 600 pound flanges at the end of each section and are separated internally by a diaphragm. The flanges are held together during operation of the shock tube by eight 1.905 cm (0.75 in) steel bolts. A gasket is located between the two flanges which allows for air tight sealing of the two sections.

The driver section of the shock tube is connected via copper tubing to both a tank of compressed helium and a vacuum pump. An inline manual valve selects between the vacuum pump and the compressed helium tank. The driver section also has a pressure gage connected inline to measure the pressure within. In addition to this manual valve, another manual valve and a pneumatic valve are connected in parallel with each other, allowing helium to be introduced into the driver section either manually or automatically (Figure 3.9). The driven section has an endcap with three 12.7 mm (1/2 in) outlets allowing for the production of up to three individual shock waves. These outlets are connected via flexible pressure rated tubing to the shock shaper and test section.

The procedure by which a moving shock is produced in the shock tube is as follows: A diaphragm of a given thickness depending on the strength of the shock
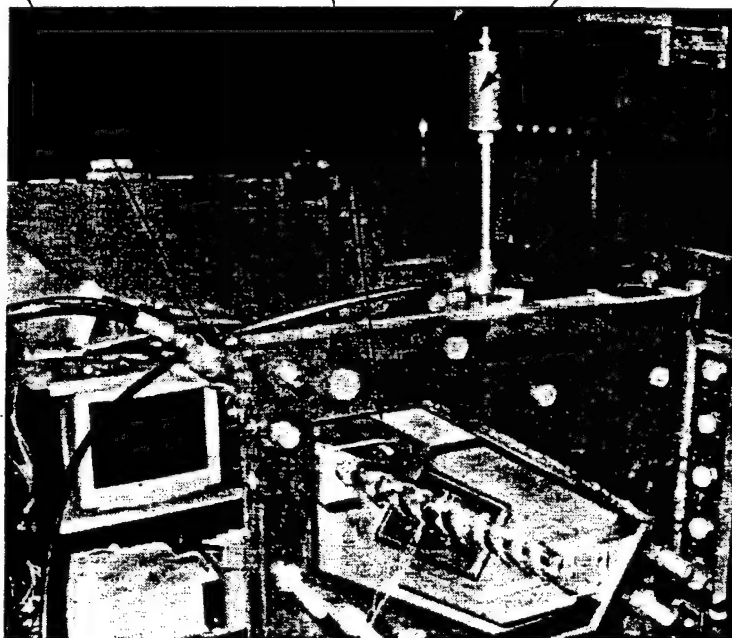
Figure 3.7  Shock Shaper and Vortex Tube Entering Test Section
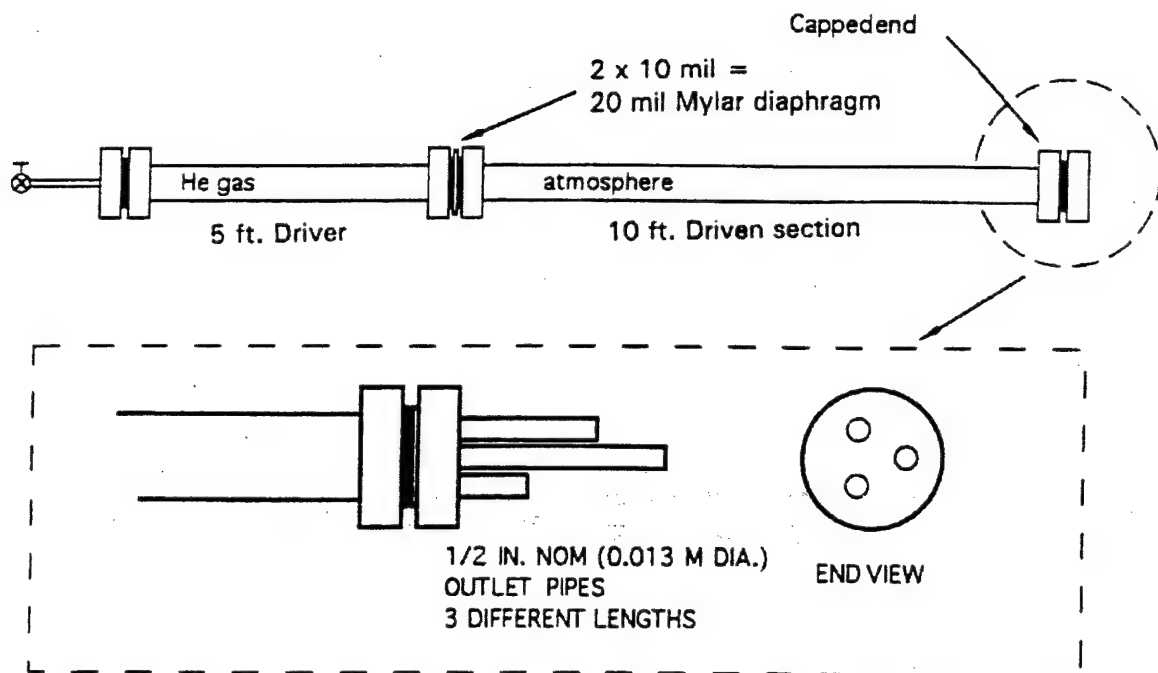
Figure 3.8  Shock Tube Schematic
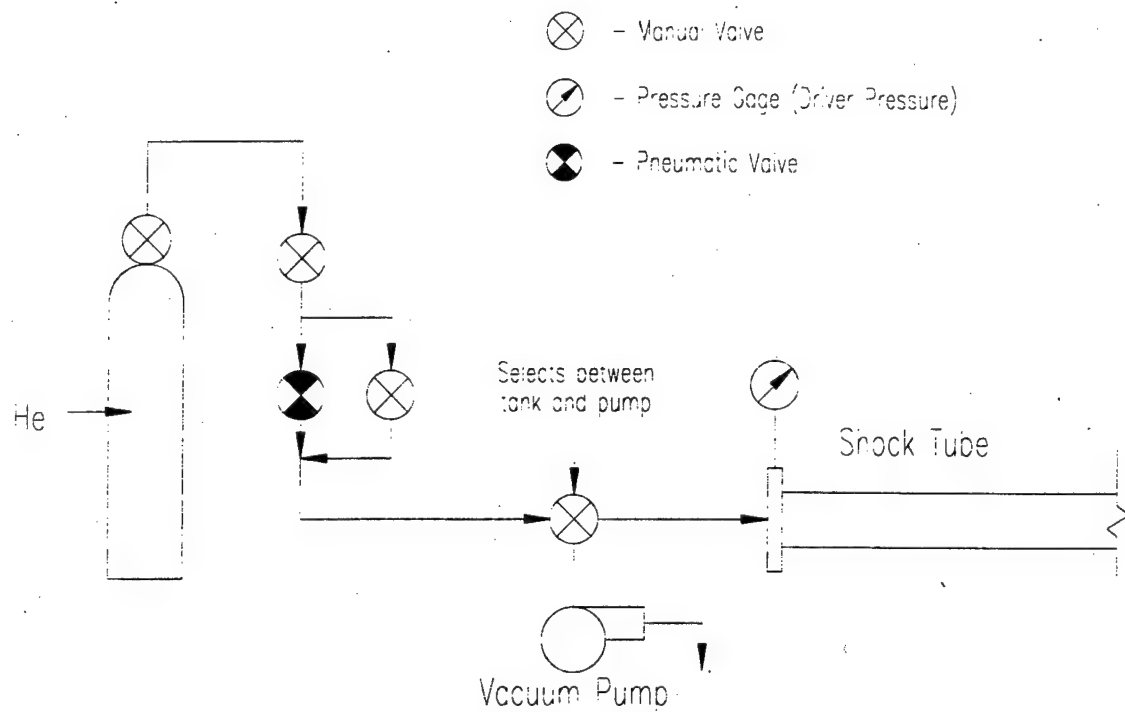
Figure 3.9  Schematic of Valves for Shock Tube Operation

desired is placed in front of the gasket between the two flanges and the connection between the flanges is sealed. The manual valve is manipulated to connect the vacuum pump to the shock tube driver section and all of the air is pumped out of the driver section. This ensures that the driver gas consists completely of helium. Helium was used as the driver gas instead of air to increase the shock pressure ratio (Doughty, et. al., 1995). The manual valve is then used to connect the helium tank to the driver section and the driver section is pumped up manually to a pressure equal to approximately one half of the burst pressure of the diaphragm. The burst pressure for a given diaphragm thickness has been estimated by previous experiments with the shock tube. The present experiments used two 10 mil (20 mil total thickness) Mylar diaphragms which gives a burst pressure of approximately 3445 kPa (500 psig). The pressure is then increased via the pneumatic valve which is powered by shop air located out of the vicinity of the shock tube for safety purposes. Upon reaching the estimated burst pressure, the diaphragm will rupture causing a moving shock wave to propagate through the driver section. The shock will then exit through one or more of the outlets in the endcap and will enter the test section through the shock shaper.

The primary purpose of the shock shaper is to change the geometry of the shock entering the test section. After traveling through tubing with a circular cross section, the shock takes on a roughly spherical shape which is undesirable for use in the test section. The shock shaper (Figure 3.10 and Figure 3.11) introduces the shock to a diverging passage which effectively increases the radius of curvature of the shock wave (Doughty, 1994). This increase in radius of curvature is such that the test section and cascade will then be introduced to an approximately planar shock wave as seen at the trailing edge of real turbine blading in a gas turbine. The shock shaper can have up to three inlet tubes connected to it and has three of these diverging passages connected in parallel, allowing for the introduction of up to three separate moving shock waves into the test section.

SECTION   A-A

MATERIAL: 1.6 mm (1/16")
Mild   Steel

A                    A

1/2 inch
Sch. 40 black
iron  pipe

0.294 m

0.146 m

FRONT   VIEW

0.049 m
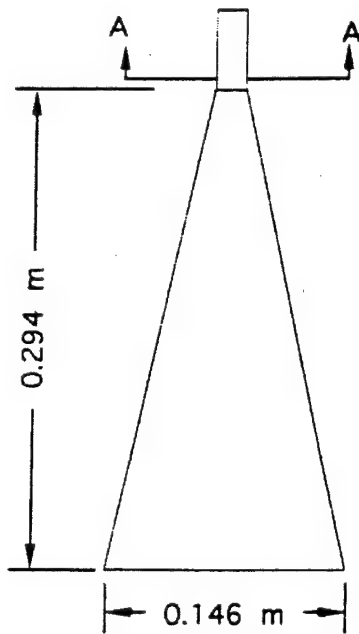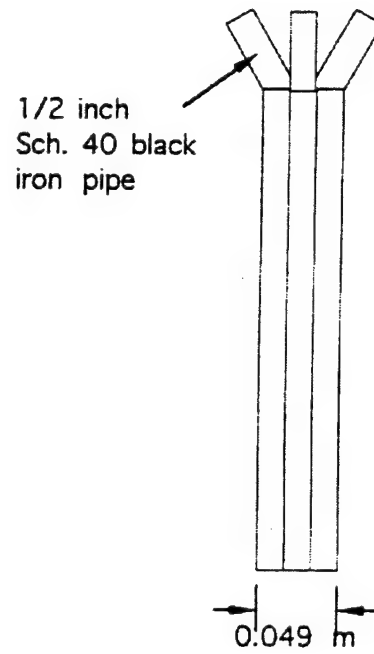
SIDE   VIEW

Figure 3.10  Schematic of Shock Shaper
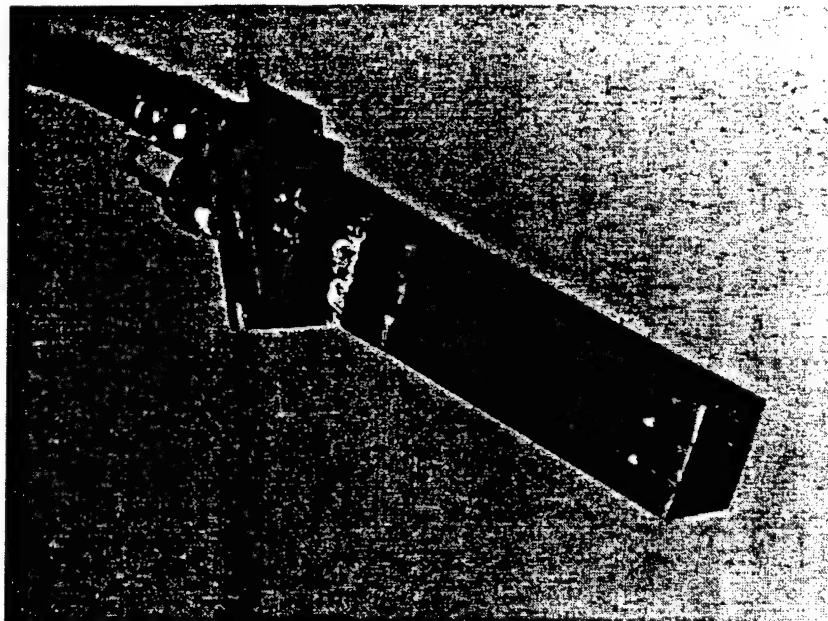
Figure 3.11  Shock Shaper Photo

## 3.4 HFM-6 Heat Flux Gage

In the experiments performed, four HFM-6 Heat Flux Microsensors were used to measure unsteady heat flux and surface temperature at various locations during runs. The HFM-6 gage is documented in published papers by Holmberg and Diller (1995), Hager, et al. (1991a), and Baker and Diller (1993). Two types of gages were used, insert gages and a gage deposited on the blade surface via a sputtering process (Figure 3.12 and Figure 3.13). Gage 1 was located on the suction surface of a blade, while gages 2 through 4 were located on the pressure surface of a blade. All four gages were located in the same blade passage. Gage 1 was varied between a sputtered gage and an insert gage in the same location for two sets of experiments in order to compare the response of the two types of gages. The insert gages were 6.32 mm (0.249 in) in diameter and 24.5 mm (0.965 in) in length. The thickness of the insert gage itself was 1.91 mm (0.075 in). The sputtered gage diameter was the same as the insert gage, minus the gage housing. The gages were numbered in the following way (Figure 3.14a and Figure 3.14b): HFM-6 gage 1 was on the suction surface of a blade 0.94 cm (0.37 in) from the leading edge, HFM-6 gage 2 was located on the pressure surface of a blade 0.43 cm (0.17 in) from the leading edge, HFM-6 gage 3 was located 1.47 cm (0.58 in) from the leading edge, and HFM-6 gage 4 was located 2.46 cm (0.97 in) from the leading edge of the blade.

The leads for each gage exit the blade through a 5.08 mm (0.20 in) hole drilled into the side of the blade and exit the test section through a hole of equal diameter drilled in the Plexiglas endwalls. The leads for each gage, 2 for the heat flux signal (HFS) and two for the temperature signal (RTS), were soldered to a female Limo plug. An aluminum bracket holding the four female Limo connectors, one for each gage, was affixed to the cascade endwalls via the allen screws which hold the blading. The gages were connected to HFM-6 signal amplifiers (Figure 3.15) using male Limo connectors.
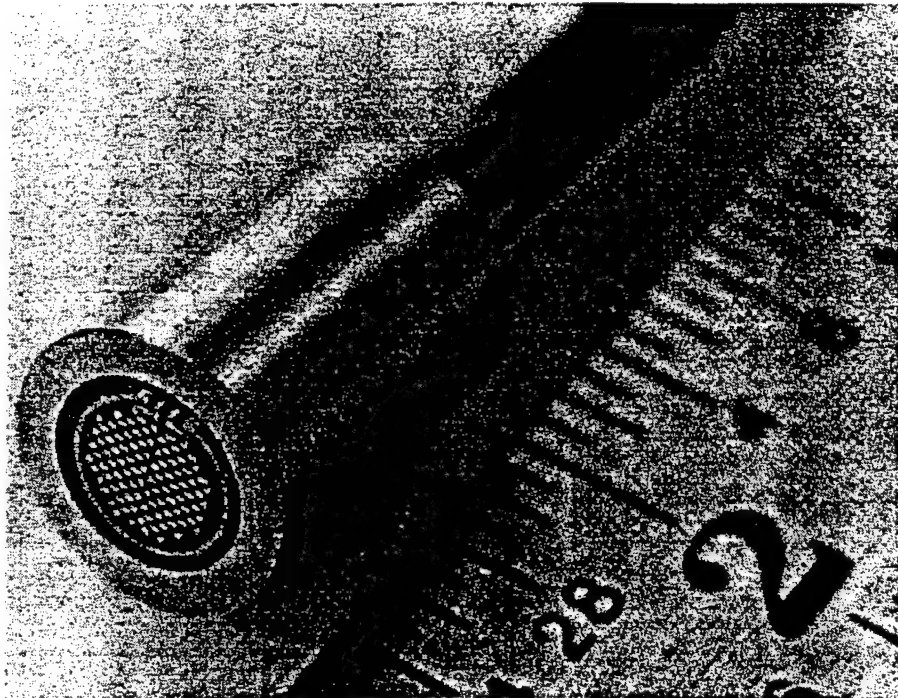
Figure 3.12  HFM-6 Insert Gage
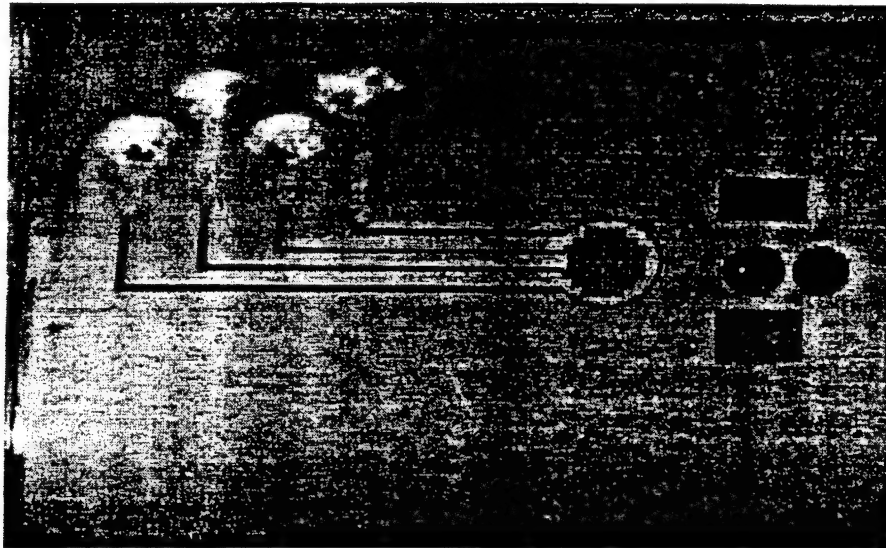
Figure 3.13  Sputtered Heat Flux Gage Photo
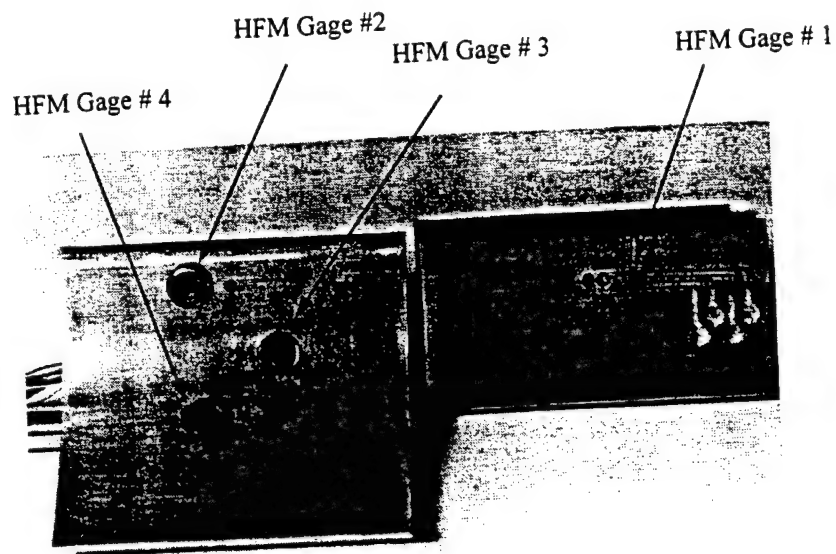
Figure 3.14a Heat Flux Gage Locations (Pressure and Suction Surfaces) Photo
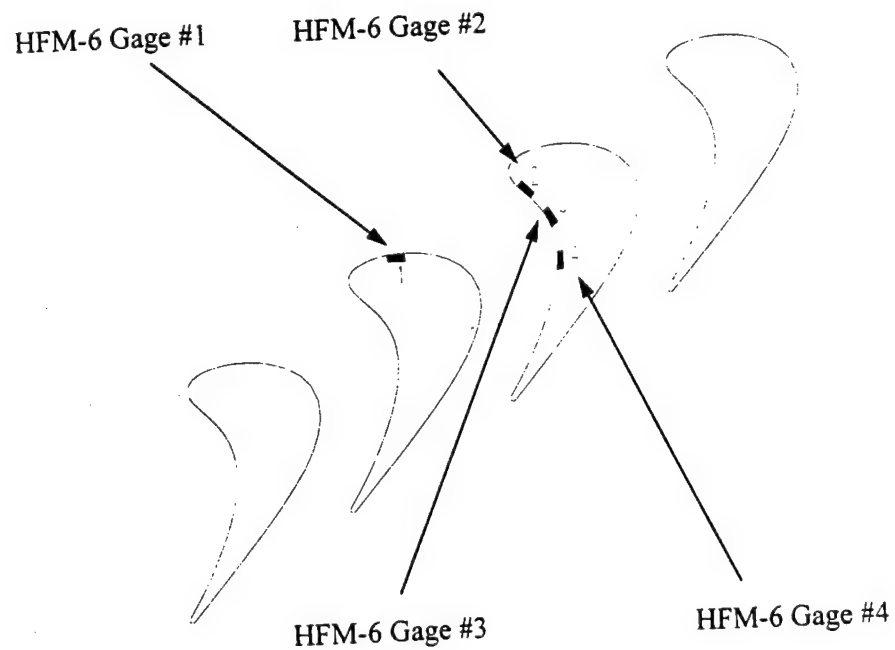


Figure 3.14b Heat Flux Gage Locations (Pressure and Suction Surfaces) Schematic
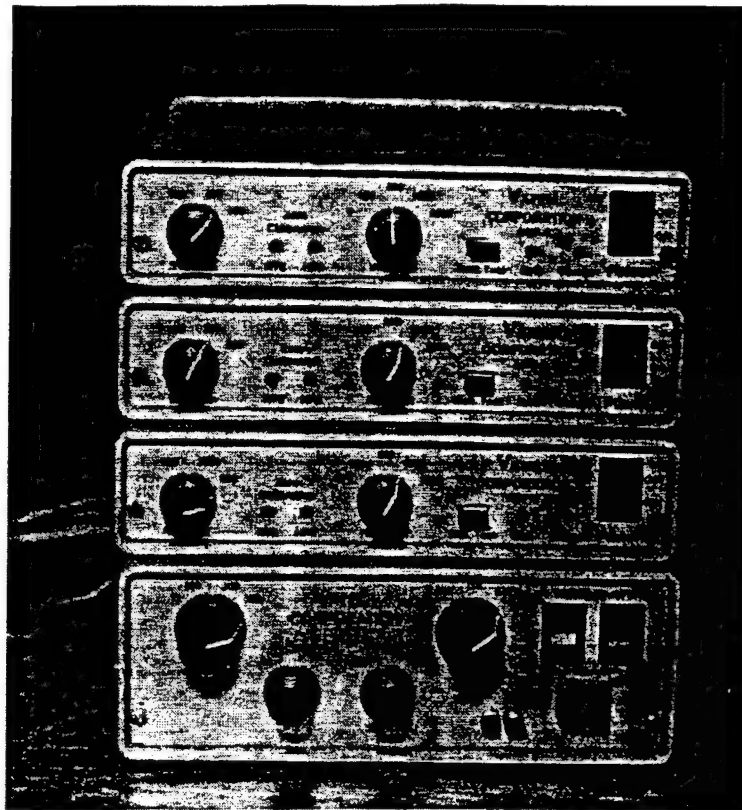
Figure 3.15  HFM-6 Amplifiers

The signals from the HFM-6 microsensors, resistance temperature sensor (RTS) and heat flux sensor (HFS), were reduced into a usable form via a spreadsheet to produce graphical results of the experiments. The procedure for the data reduction for each type of signal was as follows.

The signal for the resistance temperature sensor was recorded as a voltage and converted to a temperature in degrees Celsius. Before each series of runs, the resistance of the sensor ($R_{ref}$) and its corresponding voltage output ($E_{ref}$) were measured at ambient conditions. These values of resistance and voltage were used as references. For a single run, the difference in voltage between the run output and the reference voltage ($\Delta V = E_T - E_{ref}$) was calculated and converted to a change in resistance ($\Delta R = E_T - E_{ref}/I \cdot G_T$) in ohms using a known current and gain. This resistance change was then added to the reference resistance to find the resistance of the sensor during a run. Before the first run of a given day, the RTS voltage signal was zeroed to give the smallest $E_{ref}$ possible. The equations for finding the temperature for each RTS gage are then as follows:

HFM-6 Gage 1(s) $\qquad T_1(^\circ C) = 2.990(^\circ C / \Omega) \cdot \left( \dfrac{(E_T - E_{ref})}{I \cdot G_T} + R_{ref} \right) - 467.60^\circ C \quad$ [3.1]

HFM-6 Gage 1(i) $\qquad T_1(^\circ C) = 3.270(^\circ C / \Omega) \cdot \left( \dfrac{(E_T - E_{ref})}{I \cdot G_T} + R_{ref} \right) - 486.1^\circ C \quad$ [3.2]

HFM-6 Gage 2 $\qquad T_2(^\circ C) = 2.534(^\circ C / \Omega) \cdot \left( \dfrac{(E_T - E_{ref})}{I \cdot G_T} + R_{ref} \right) - 415.9^\circ C \quad$ [3.3]

HFM-6 Gage 3 $\qquad T_3(^\circ C) = 2.655(^\circ C / \Omega) \cdot \left( \dfrac{(E_T - E_{ref})}{I \cdot G_T} + R_{ref} \right) - 412.3^\circ C \quad$ [3.4]

HFM-6 Gage 4    $T_4(^\circ C) = 2.602(^\circ C / \Omega) \cdot \left( \dfrac{(E_T - E_{ref})}{I \cdot G_T} + R_{ref} \right) - 440.9^\circ C$    [3.5]

where $E_T$ is the amplified voltage of the RTS sensor, $E_{ref}$ is the amplified voltage measured at ambient conditions (zero voltage), $G_T$ is the gain setting for the RTS (all sensors were set to a gain of 500), I is the current, and $R_{ref}$ is the reference voltage measured at ambient conditions. The (s) and (i) refer to the sputtered and insert gages at location 1, respectively. Using the calculated RTS temperature, the sensitivity of the heat flux gage, which is temperature dependent, could then be calculated and used to find the heat flux (q"). The equations for calculating the sensitivity for each gage are as follows:

HFM-6 Gage 1(s)    $S_1(T) = 0.0377 \cdot T_1(^\circ C) + 11.332(\mu V / W / cm^2)$    [3.6]

HFM-6 Gage 1(i)    $S_1(T) = 0.0350 \cdot T_1(^\circ C) + 21.330(\mu V / W / cm^2)$    [3.7]

HFM-6 Gage 2    $S_2(T) = 0.0343 \cdot T_2(^\circ C) + 14.80(\mu V / W / cm^2)$    [3.8]

HFM-6 Gage 3    $S_3(T) = 0.0318 \cdot T_3(^\circ C) + 14.13(\mu V / W / cm^2)$    [3.9]

HFM-6 Gage 4    $S_4(T) = 0.0295 \cdot T_4(^\circ C) + 5.27(\mu V / W / cm^2)$    [3.10]

Using the sensitivity, S, for each gage, the heat flux (q") is then found using:

$$q"(W / cm^2) = \frac{E_q(\mu V)}{G_q \cdot S}$$    [3.11]

where $E_q$ is the amplified output voltage of the heat flux sensor (HFS), and $G_q$ is the gain of the HFS. All heat flux sensor gains were set to 1000. Before the first run of a given day, the HFS voltage signal of each gage was zeroed to insure that zero voltage corresponded to no heat flux. The heat flux signal for each gage could be plotted versus time to find the time history of heat flux due to shock wave passing.

## 3.5 Kulite Pressure Transducers

The pressure transducers used in this experiment were XCQ-062-50 high-response miniature transducers (Figure 3.16). The transducers have a diameter of 1.7 mm (0.067 in) and are of varying length. Each transducer is equipped with a B-screen which protects the internal diaphragm from being damaged by debris moving through the test section.

Seven Kulites were used in the experiments, four for measuring blade static pressure, two for measuring wall static pressure (used to calculate shock speed and strength), and one as an external trigger for the data acquisition system. The blade Kulites were located in close proximity to the heat flux gages used in the experiments (Figure 3.17). Gage 1 was located on the suction surface of a blade, 0.76 cm (0.30 in) from the leading edge of the blade. Gages 2 through 4 were located on the pressure surface of a blade. Gage 2 was located 0.43 cm (0.17 in) from the leading edge of the blade, Gage 3 was located 1.47 cm (0.58 in) from the leading edge, and Gage 4 was located 2.46 cm (0.97 in) from the leading edge of the blade. The wall Kulites used for measuring static pressure were located just upstream of the instrumented blade passage (Figure 3.18). These Kulites were located 1.27 cm (0.5 in) apart and 1.27 cm (0.5 in) above the blades. The Kulite used as an external trigger for the data acquisition system was located in a piece of Plexiglas connected to an aluminum block with a section of tubing from the shock tube clamped in an opening in the aluminum block. The outlet of the tubing was pointed towards the trigger Kulite (Figure 3.19).
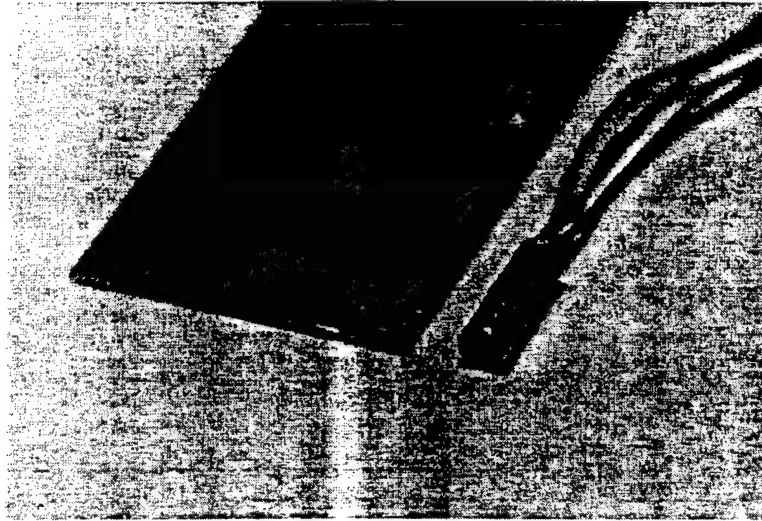
Figure 3.16  Kulite XCQ-062-50 Miniature Pressure Transducer
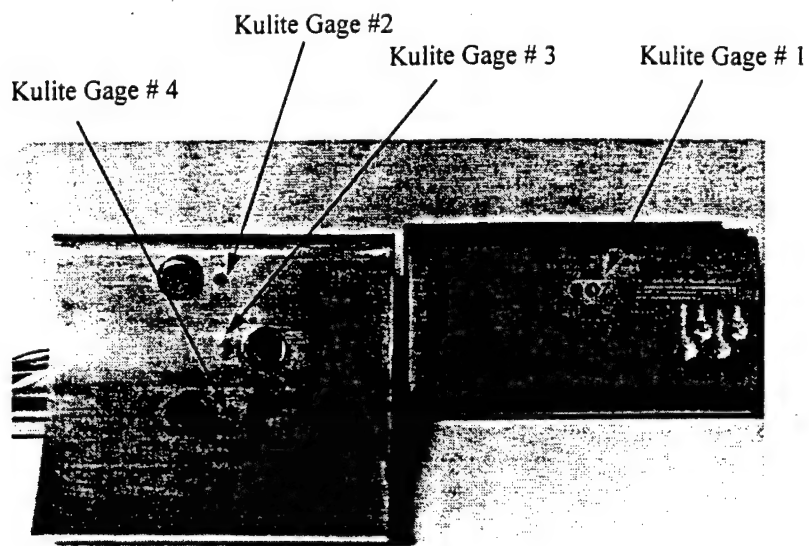
Figure 3.17  Kulite Locations (Pressure and Suction Surfaces) Photo

Wall Kulites    Instrumented Passage
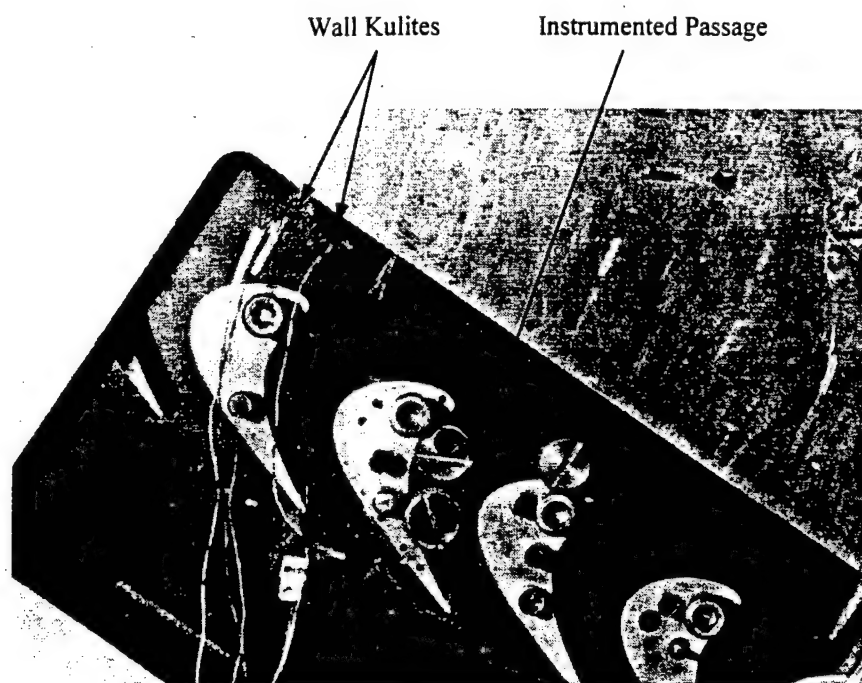
Figure 3.18  Location of Wall Static Pressure Kulites

Trigger Kulite

Tubing from Shock Tube



Figure 3.19  External Triggering Set-up
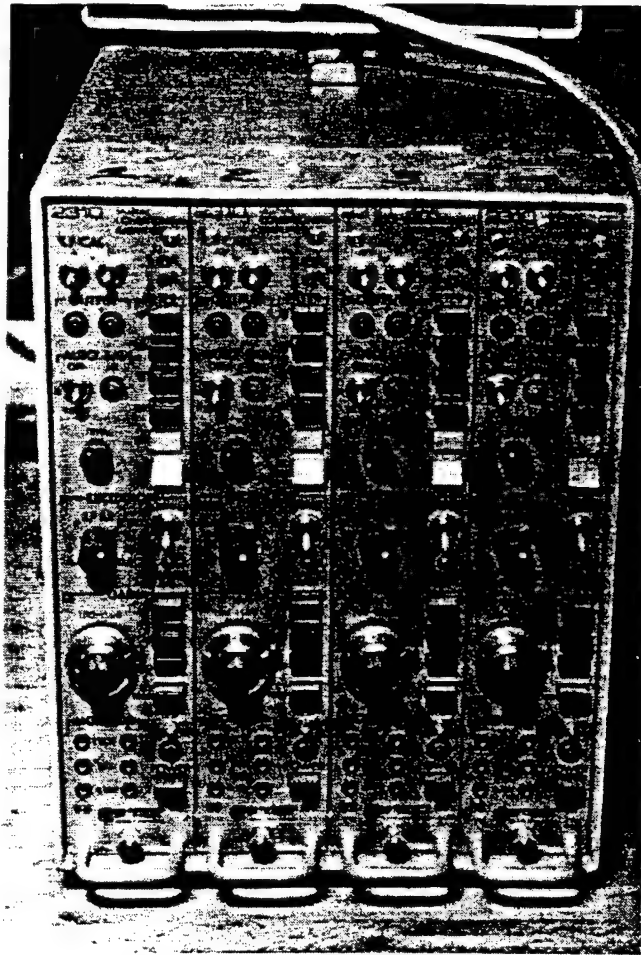
Figure 3.20  Kulite Signal Conditioner/Amplifiers
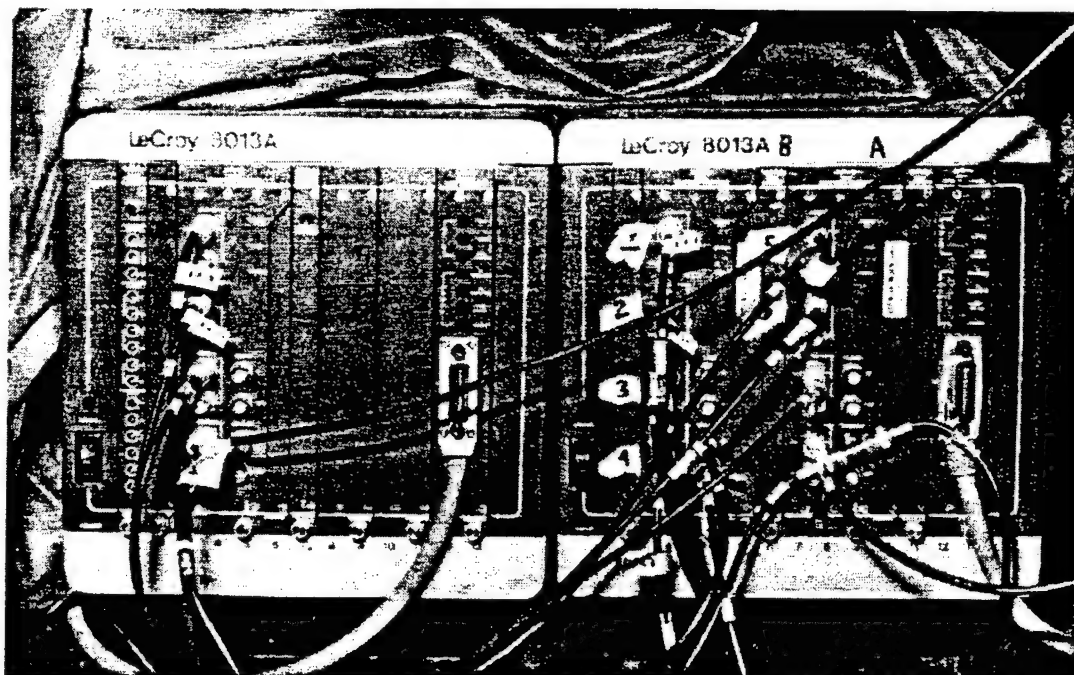
Figure 3.21  Lecroy Waveform Recorders

(sampling rate, number of data points, peak-peak voltage, etc.). The Lecroy modules allow sampling frequencies of up to 1 MHz (1μs sampling period). Data from the Lecroy was stored in a binary file, along with a document file which contains a record of the sampling frequency used, and the number of data points contained in the binary data file. The binary data file was converted to an ASCII format file which was then written into a spreadsheet for data reduction purposes. Each gage/probe output was connected to a single channel of the Lecroy module(s) and a corresponding channel name was assigned to each within the data acquisition software.

The data recorded for each type of run consisted of static pressure data from the Kulite pressure transducers (both blade surface and wall static pressure), heat flux from the HFS on each HFM-6 gage, and blade surface temperature from the RTS on each HFM-6 gage. In addition to pressure, heat flux, and blade temperature, the upstream total temperature and pressure probes were connected to individual channels. The calibration equations used to convert these two signals were as follows:

Total Temperature: $\quad\quad\quad T_T(°C) = 0.245(°C/mV) \cdot E_{TT} + 6.15(°C)$ $\quad\quad$ [3.13]

Total Pressure: $\quad\quad\quad\quad P_T(psi) = 25.128(psi/V) \cdot E_{PT} - 25.11(psi)$ $\quad\quad$ [3.14]

where $E_{TT}$ and $E_{PT}$ are the voltage output from the total temperature and pressure sensors, respectively.

All data channels were sampled at 1 MHz (1μs sampling period), with a total of 4000 points being recorded. The pressure signal from the external trigger was connected to an external trigger channel, which was set to a specific reference voltage. Once this trigger reference voltage was achieved, the data acquisition system would store data. In order to capture the passing shock event, a delay was set such that the data file written would store data for one time segment (approximately 1500 μs) before the data

acquisition system was triggered. Since the Lecroy module is continually receiving data into its buffer, this allows the data acquisition to store data from before and after the shock reached the test section.

The cascade experiments conducted in the wind tunnel facility were of three types: no flow, cold flow (unheated), and heated runs. The basic procedure for each type of test was similar, however, some differences existed which define the type of run. By definition, the no flow cascade tests involved no operation of the tunnel and heated runs had the added procedure of charging the heat exchanger tubes before tunnel operation, which was described previously. The basic procedure for cascade runs follows.

After all sensors and gages were connected to their appropriate channels and the data acquisition software was properly set up, the cascade test was ready to be performed. The diaphragm in the shock tube was changed and the shock tube was set up for operation, awaiting triggering by the pneumatic valve. For flow tests, the compressed air storage tanks were loaded to the appropriate pressure and allowed to equilibrate. If heated runs were being performed, the heat exchanger tubes were heated to the desired temperature and the test section was cooled via the vortex tube. The flow temperature and blade temperatures were allowed to vary between runs to get a range of blade to flow temperature differences. Once tank pressure and cascade and heat exchanger temperatures, if needed, were at their desired values, tunnel start-up was commenced. The tunnel control program continually plots the tunnel pressure and displays a line which represents the target tunnel pressure. Typically, there is some overshoot of the target pressure and a settling of the tunnel pressure as the control algorithm actuates the control valve. The target pressure, under proper control parameters, is typically reached within 10 seconds. Parameters for the control algorithm include a length and magnitude for overshoot control, storage tank temperature, target pressure, ambient pressure, and throat area. The throat area is the combined area of all the blade passages. This area is

adjusted depending on whether the shock shaper is inserted into the test section, since the shaper blocks approximately one and a half blade passages.

Once the tunnel pressure is stabilized, the data acquisition system was armed and the pneumatic valve was engaged, increasing the pressure in the driver section of the shock tube until the diaphragm ruptured. The resulting shock was split at the driven section endcap, sending one shock to the external trigger setup and one shock through the shock shaper and into the test section. The setup was adjusted such that a shock would reach the trigger Kulite at the same instant the shock entering the test section was propagating through the test section towards the instrumented passage. This procedure eliminating having to set a trigger pressure of a Kulite located in the cascade between the tunnel pressure and the pressure resulting from a passing shock, which can be difficult. Once the trigger Kulite was exposed to the pressure of the passing shock, the data acquisition system triggered automatically, capturing all desired data within the test section. After visually verifying that the data was successfully collected, the data for each channel was written to an ASCII file, ready for data reduction and analysis.

## 3.7 Bench Tests

Prior to cascade experiments, tests were performed on a bench test rig external to the wind tunnel facility. The bench test was designed to perform some preliminary analysis of the effects of passing shock on heat flux in a no flow, simple geometry environment. The bench test rig consists of an aluminum block with an opening which holds the shock shaper and a flat 41.9 cm (16.5 in) x 17.78 cm (7.0 in) piece of 3/8 inch Plexiglas (Figure 3.22). Mounted into the Plexiglas flush with the wall were two Kulite pressure transducers and a single insert HFM-6 heat flux gage. Testing on the bench test was done with two different set-ups, one for a shock passing tangentially over the gages and one for a shock impacting normally into the gages. This simulates the two ways in which a shock can contact the blades in the test section. In order to allow the normally

HFM-6 Gage          Wall Kulites          Shock  Shaper from Shock Tube
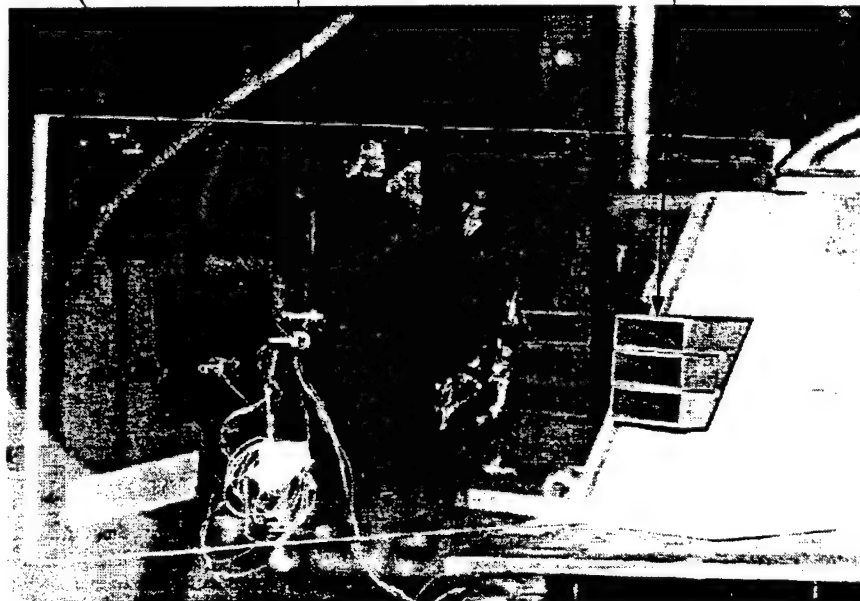


Figure 3.22  Bench Test Rig

impacting shock to be tested, a 10.16 cm (16.5 in) x 17.78 cm (7.0 in) piece of 3/8 inch Plexiglas was attached to the bench test rig such that it is normal to the shock exiting the shock shaper. The method by which the shock is produced and introduced to the bench test rig is the same as for the cascade tests, except the shock shaper is inserted into the bench test. Likewise, the procedure for data collection is similar to the cascade tests, except that only two wall static pressure measurements (the first of which was used as the trigger for the data acquisition system) and one heat flux signal were recorded and saved and no tunnel runs were necessary.

# Chapter 4.0

## Shock Heat Transfer Analysis

In order to gain a better understanding of the heat transfer due to a passing shock, a theoretical model was developed. The model was used to predict unsteady heat transfer due to shock heating, i.e. heat transfer driven by the temperature change introduced by the passing shock, in the absence of a boundary layer. The following sections describe the model developed for both a normally impacting shock and a tangentially passing shock. Figure 4.1 and Figure 4.2 present graphical representations of the normally impacting and tangentially passing shocks in both a flat plate and turbine blade passage.

### 4.1 Normally Impacting Shock

The model developed to predict the time-resolved heat transfer due to a passing shock employs the principal of the semi-infinite solid. The normally impacting shock wave was modeled as a planar shock propagating towards a wall through a stagnant media, reflecting off the wall and then moving off into the direction in which it came. Figure 4.3 depicts in stages the shock wave passing event, along with the resulting temperatures and pressures introduced by the passing shock assuming a given shock strength. From this figure, assuming the reflected shock wave is of approximately equal strength as the original shock before reflection, it can be seen that what remains after the passing shock event is a wall with temperature $T_w$ and a "slug" of stagnant hot gas at temperature $T_\infty$ and pressure $P_\infty$. In order to employ this model, the temperatures of the wall and the hot gas slug, as well as the thermal properties of the gas, needed to be determined. To calculate these quantities, moving shock theory was employed. The wall temperature was assumed to be equal to the ambient temperature in the room (the temperature of the stagnant air prior to shock wave passing). The temperature of the gas behind the shock wave was determined using the shock strength (given as either a Mach number or a pressure ratio) which determines the temperature ratio of the shock. The

Note: Point A on both pictures will see a
normally impacting shock



Flat Plate                          Turbine Blade Passage
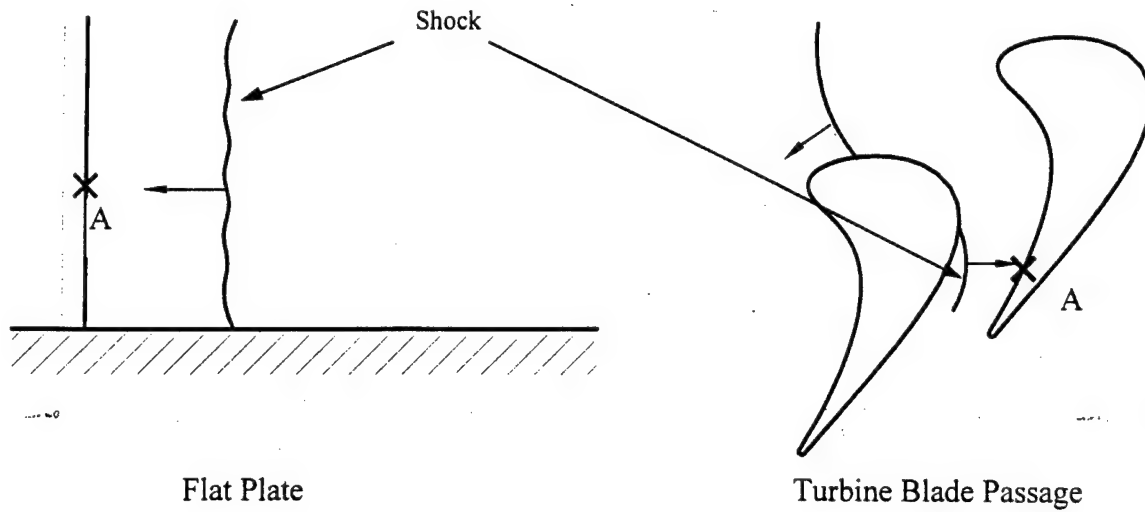
Figure 4.1  Normally Impacting Shock Illustration

Note: Point A on both pictures will see a
tangentially passing shock.
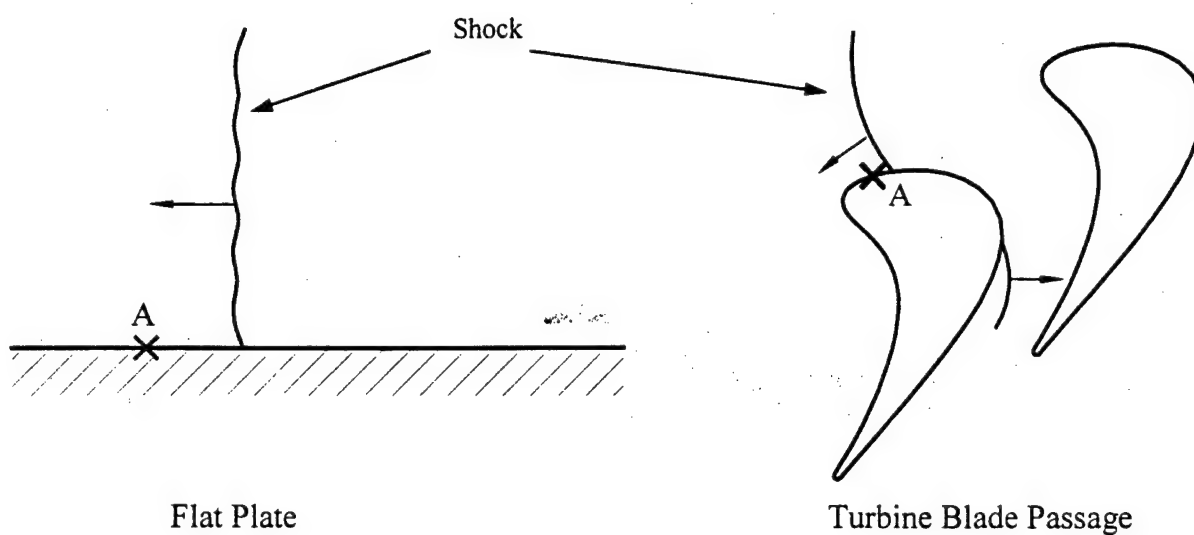


Figure 4.2  Tangentially Passing Shock Illustration

| | | |
|---|---|---|
| $P_1$ | | $P_2$ |
| $T_1$ | ← | $T_2$ |
| $V_1=0$ | | $V_2\neq0$ |
| | $V_s$ | |

Before Shock Impact

| |
|---|
| $P_2$ |
| $T_2$ |
| $V_2\neq0$ |

Instant of Shock Impact

$T_w$

| | | |
|---|---|---|
| $P_3=P_\infty$ | | $P_2$ |
| $T_3=T_\infty$ | → | $T_2$ |
| $V_3\approx0$ | | $V_2\neq0$ |
| | $V_s$ | |

After Shock Impact
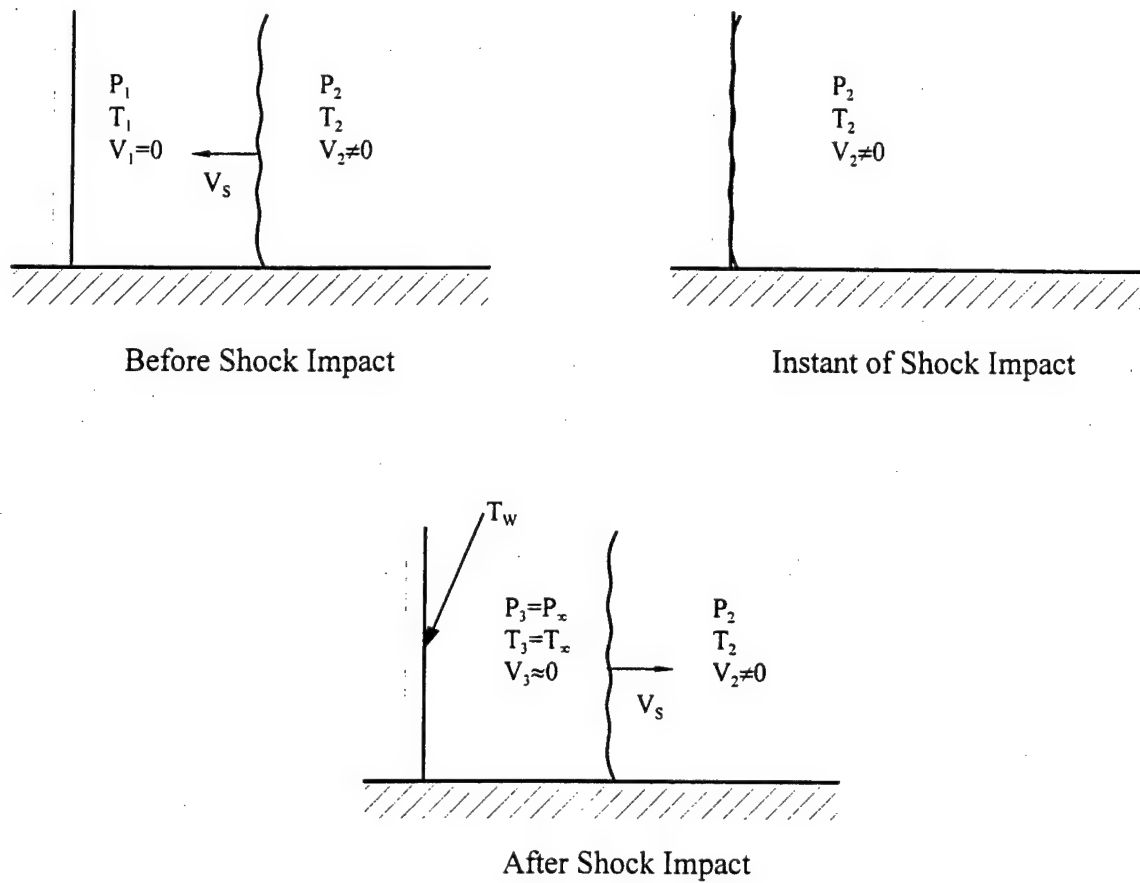
Figure 4.3  Stages of Shock Passing Event (Normally Impacting)

Note:  For tangentially passing shock, there is no reflection, therefore $P_\infty=P_2$ and $T_\infty=T_2$.

temperature behind the shock was then: $T_2 = TR \cdot T_1 = \dfrac{T_2}{T_1} \cdot T_1$, where TR is the temperature ratio of the shock wave, $T_1$ is the temperature of the gas before the shock wave and $T_2$ is the temperature of the gas behind the shock. The temperature of the hot gas was increased again after the reflected shock moves through the gas, as shown in Figure 4.3, thus this equation was applied again the find the temperature, $T_\infty$, after both the incident and reflected shock have passed. The temperature of the wall which the shock impacts was assumed to remain constant during the heat transfer process due to the relatively small temperature increase and the high thermal conductivity of the wall (gage) material.

The model employed consisted of a stationary semi-infinite gas of temperature $T_\infty$ transferring heat to a wall at temperature $T_w < T_\infty$ (Figure 4.4). The equation for the unsteady heat transfer resulting from this model is given by (Incropera and DeWitt, 1990):

$$q_x^{"}(t) = -k \left. \frac{\partial T}{\partial x} \right|_{x=0} = k \cdot \frac{(T_w - T_\infty)}{\sqrt{\pi \alpha t}} \qquad [4.1]$$

where k is the thermal conductivity and $\alpha$ is the thermal diffusivity of the stagnant gas slug. The results of this model yield infinite heat flux at time t=0, followed by heat flux which decays as $\dfrac{1}{\sqrt{t}}$. This theoretical model predicts the heat flux which occurs under these conditions, however, due to the time of the shock event, the response of the heat flux gage required additional analysis.

The response of the heat flux gage was modeled using a first order time response function substantiated by Holmberg and Diller (1995) given by:

HFM-6 Gage

$T_w$=Const.

$T_\infty$ , $P_\infty$ ⟶ $\alpha$ , k

Hot "Slug" of Stagnant Gas -
Semi-infinite
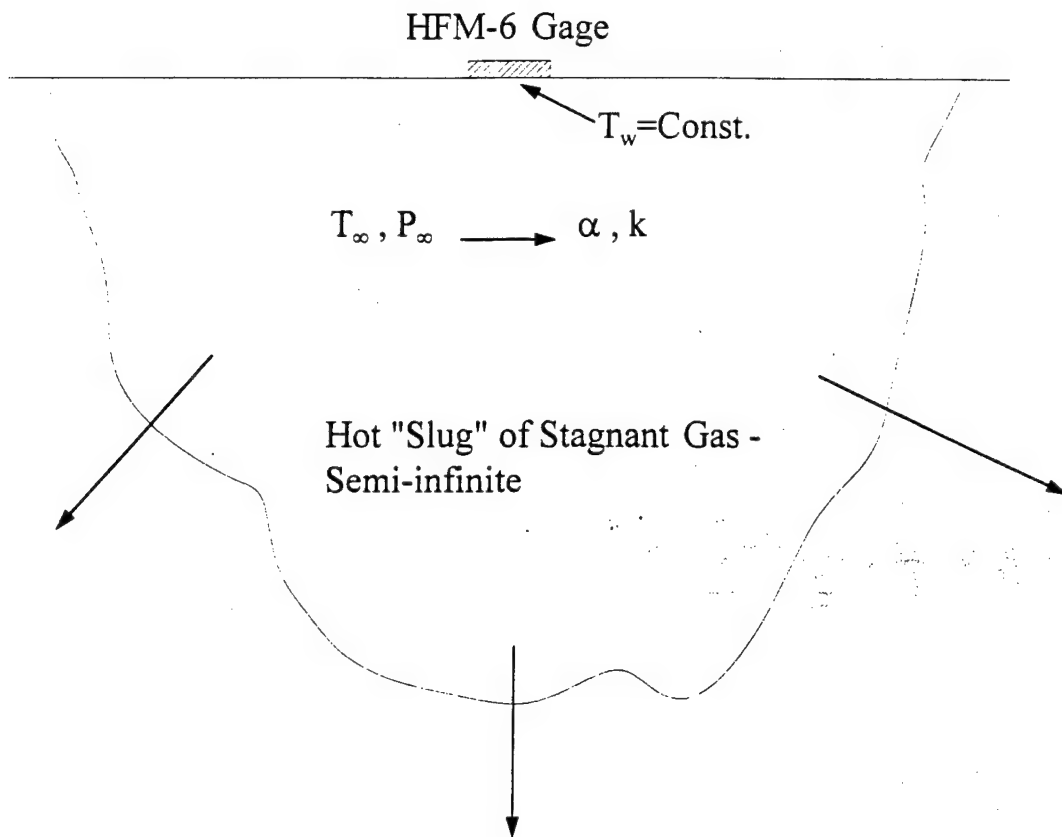
Figure 4.4  Semi-infinite Solid (Gas) with Constant Surface Temperature

$$q_{g}^{"}(t) = q_{s}^{"}(t) \cdot (1 - e^{-t/\tau}) \qquad\qquad [4.2]$$

where $q_{g}^{"}(t)$ is the unsteady heat flux response of the heat flux gage, $q_{s}^{"}(t)$ is the unsteady heat flux resulting from the semi-infinite model, and $\tau$ is the characteristic time constant of the heat flux gage. By applying this response function to each small time segment of the theoretical heat flux predicted by the semi-infinite model, the response of the heat flux gage could then be predicted. The time constant of the HFM-6 heat flux microsensor was determined in shock tunnel experiments by Holmberg and Diller (1995) to be approximately 6 µs. In order to apply this first order response function, a FORTAN code named RESP2REV.FOR (Peabody, 1996) was developed to calculate the gage response from given theoretical semi-infinite model results. The equation for the gage response $q_{g}^{"}(t)$ applied in this FORTRAN code is given by:

$$q_{g}^{"}(t) = \sum_{j=1}^{n} q_{s}^{"}(t_{j}) \cdot e^{t_{n} - t_{j}/\tau} \qquad\qquad [4.3]$$

The code is presented in Appendix D. Figure 4.5 shows a sample of the results of this model applied to a normally impacting shock bench test run. It can be seen from this plot that the theoretical semi-infinite model, coupled with the first order time response function, provides a good approximation of the measured heat flux over a time period of approximately 50 µs.

Before applying this model for comparison with an actual bench test, the shock strength and subsequent temperature and pressure ratios during a bench test needed to be determined. This was accomplished using the two wall Kulite pressure transducers. The distance between the two Kulites was measured using a micrometer, and the time delay between the shock peak of the pressure traces from these two Kulites was used to determine the time it took for the shock to travel this distance. Using these two
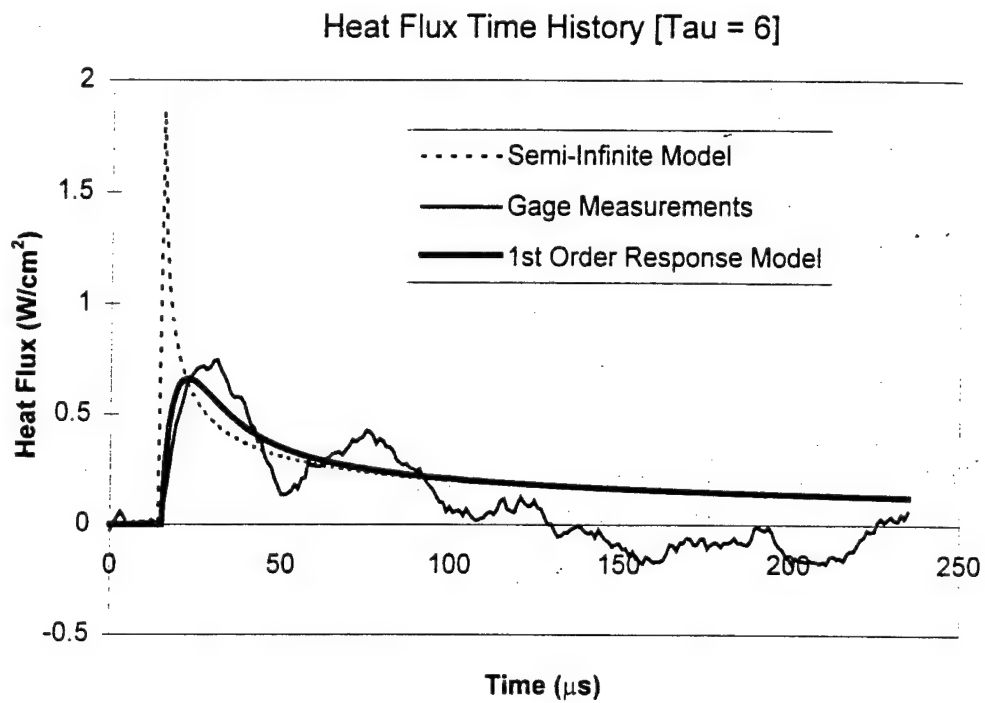
Figure 4.5  Sample Results of Theoretical Response Model - Normally Impacting Shock

quantities, the shock speed was then determined. Using a known temperature for the air into which the shock is moving (ambient), a shock Mach number was then calculated:

$$M_s = \frac{V_s}{\sqrt{\gamma R T_a}} \qquad\qquad [4.4]$$

where $V_s$ is the shock velocity, $\gamma$ is the ratio of specific heats for the gas ($\gamma=1.4$), R is the ideal gas constant, and $T_a$ is the temperature of the gas the shock is moving into. The temperature and pressure ratios of the shock wave could then be determined using moving shock theory (from Chapter 2) and transforming the reference frame. For the reflected shock wave, the process of finding the shock strength was similar, except that the shock wave was propagating through a gas with a higher temperature and pressure, and the gas had a small velocity which was induced by the original (unreflected) shock passing.

## 4.2 Tangentially Passing Shock

The model developed for the tangentially passing shock employed the same principals as the normally impacting shock, however, additional factors of the physics of the shock passing event needed to be considered. The normally impacting shock event could be viewed as an instantaneous process, since the time that the shock is actually in contact with the gage (wall) approaches zero. However, for the tangentially passing shock, the shock must move across the surface of the gage (wall), taking approximately 15 μs based on typical shock velocities in the current experiments (Figure 4.6). The gas left behind the tangentially passing shock is actually not stagnant, rather there is an induced velocity behind the shock. However, the induced velocity is small compared to that of the shock (approximately 7% of the shock velocity), and the gas was therefore assumed to be stagnant for modeling purposes. Because the gage has approximately 100 thermocouple pairs, each generating its own voltage response, it could be modeled in
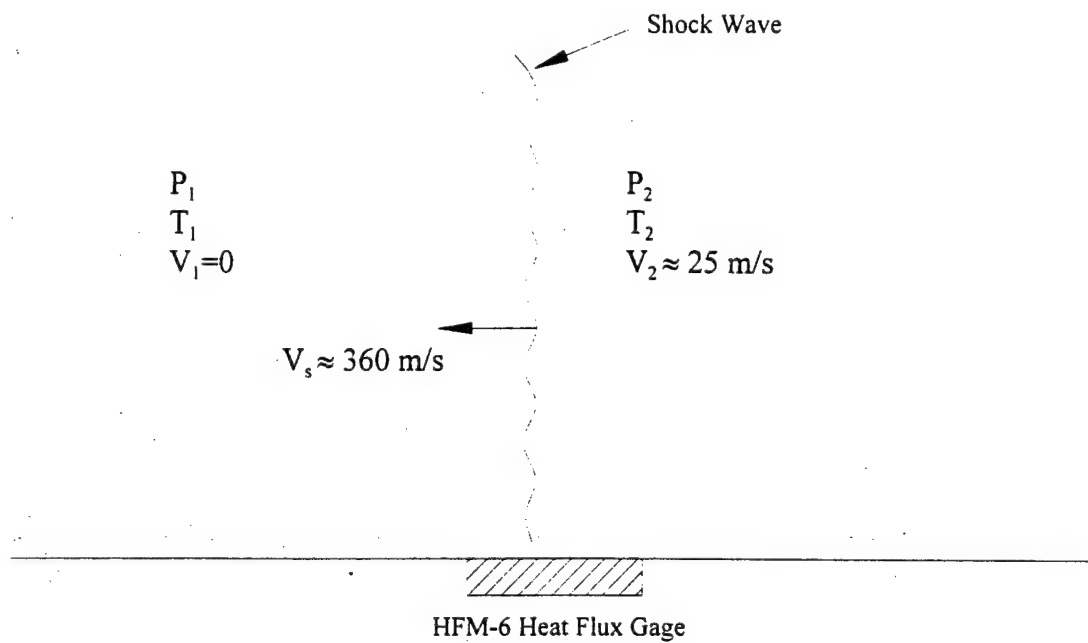
Figure 4.6  Moving Shock Passing Tangentially over HFM-6 Gage

segments. The time that the shock takes to pass over the gage was accounted for by breaking the gage up into small increments and determining the semi-infinite model unsteady heat flux for each small segment. The segment size was selected such that it would take approximately 1 μs for the shock to travel across each segment. For simplicity in the calculations, the gage was assumed to be square, so each segment was of equal area and length in the shock propagation direction. The theoretical model results for each small segment were then incorporated into the first order gage response function. The gage response of each small segment was multiplied by the fraction of the gage area each segment represents. The weighted responses of each gage segment were then added together with the proper time offset to determine the unsteady heat flux response of the entire heat flux gage due to a tangentially passing shock:

$$q_g^{"}(t) = \sum_{i=1}^{m} \left[ \sum_{n=1}^{15} \left( q_n^{"}(i\Delta t) \cdot e^{t_m - i\Delta t / \tau} \cdot \frac{1}{15} \right) \right] \qquad [4.5]$$

where q"$_g$(t) is the unsteady response of the entire heat flux gage, and q"$_n$(t) is the response from the semi-infinite model coupled with the first order time response function of each segment, n, at a given time, t, and Δt is 1 μs. The gage response was typically calculated for about 500 μs (m=500). Figure 4.7 shows a sample of the results of this model applied to a tangentially passing shock bench test run. Additional results for both types of shock passing, along with some analysis and additional results will presented in Chapter 5.
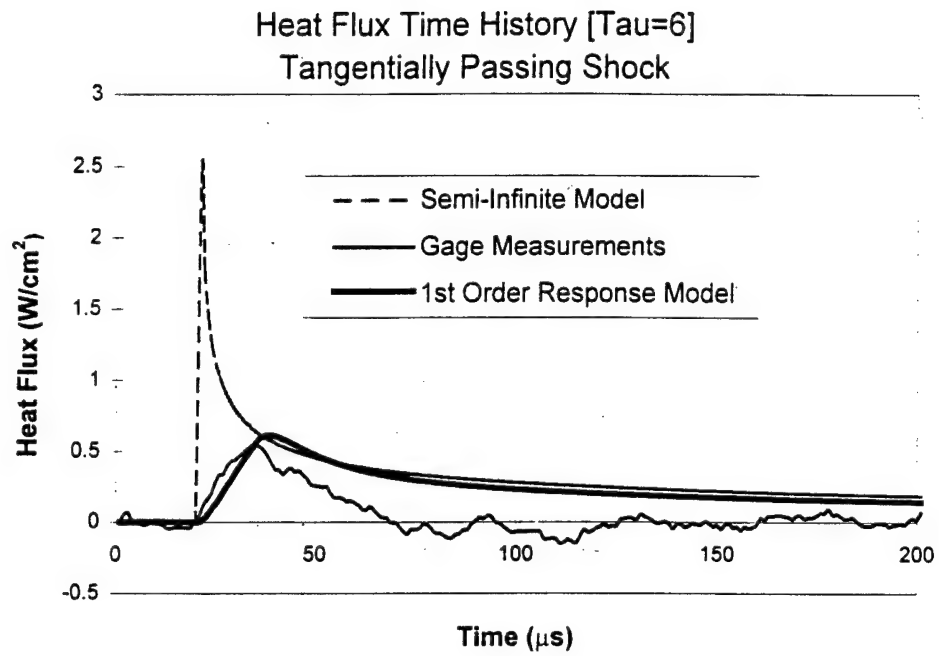
Figure 4.7  Sample Results of Theoretical Response Model - Tangentially Passing Shock

# Chapter 5.0

## Results

The following sections report the results for the experiments performed, both bench tests and cascade tests. A discussion of the results from each experiment is presented in the individual sections and in Chapter 6.

### 5.1 Bench Tests

The primary purpose of the bench tests was to obtain an understanding of the unsteady heat flux occurring due to a passing shock without the complications of a boundary layer. This was accomplished using the bench test rig described in Chapter 3. The pressure data from the two Kulites and the heat flux data from the HFM-6 insert gage mounted in the wall of the bench test rig were reduced and analyzed. Figure 5.1 and 5.2 show sample plots of the heat flux and pressure data obtained during a normally impacting shock bench test, respectively. Sample plots of tangentially passing shock data are shown in Figure 5.3 and Figure 5.4. Results from additional bench test runs are shown in Appendix A.

The results from the bench tests were compared to the theoretical shock heat transfer analysis discussed in Chapter 4. The results of the theoretical response model were plotted for each bench test to demonstrate the applicability of the model. Inclusion of the time constant of the HFM-6 heat flux gages was achieved by plotting the response of the gage for both cases for time constants ($\tau$) of 5, 6, and 7 $\mu$s. The gage response time constant was included because the shock event occurs very fast, even for measurements using the HFM-6 gages. The gage time constant is present in the equation from Chapter 4 for the first order time response function of the heat flux gage:
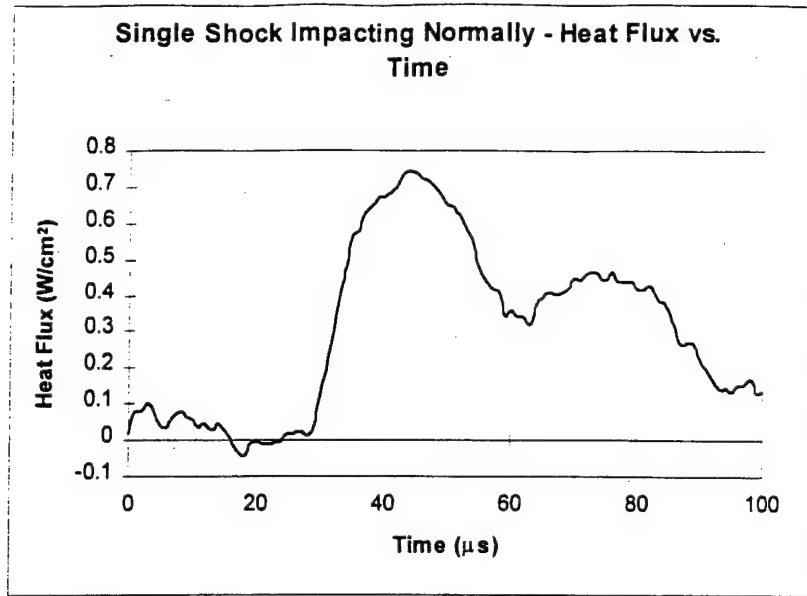
Figure 5.1  Sample Plot of Heat Flux for Normally Impacting Shock Bench Test
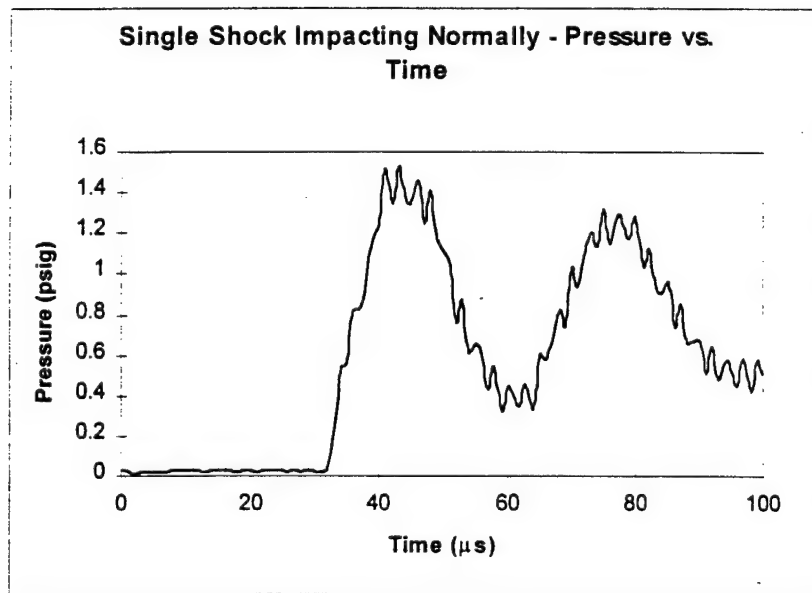


Figure 5.2  Sample Plot of Pressure for Normally Impacting Shock Bench Test
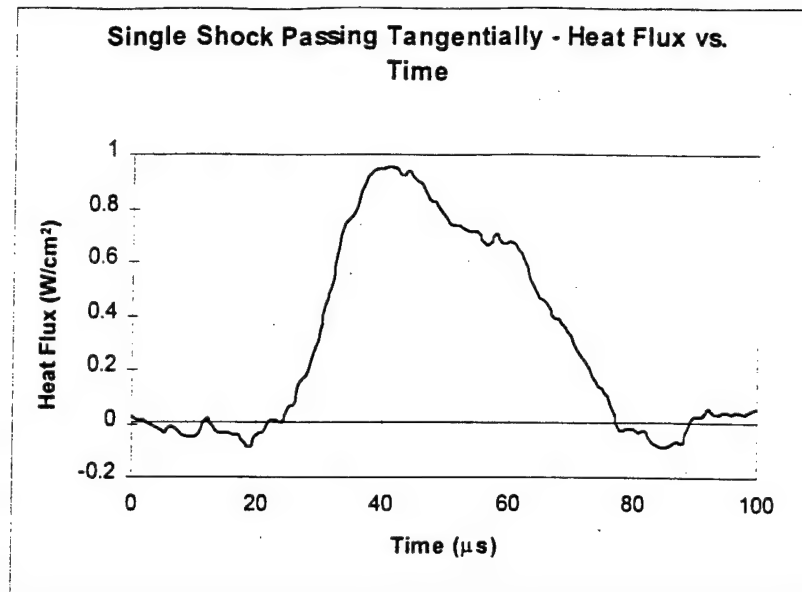
Figure 5.3  Sample Plot of Heat Flux for Tangentially Passing Shock Bench Test
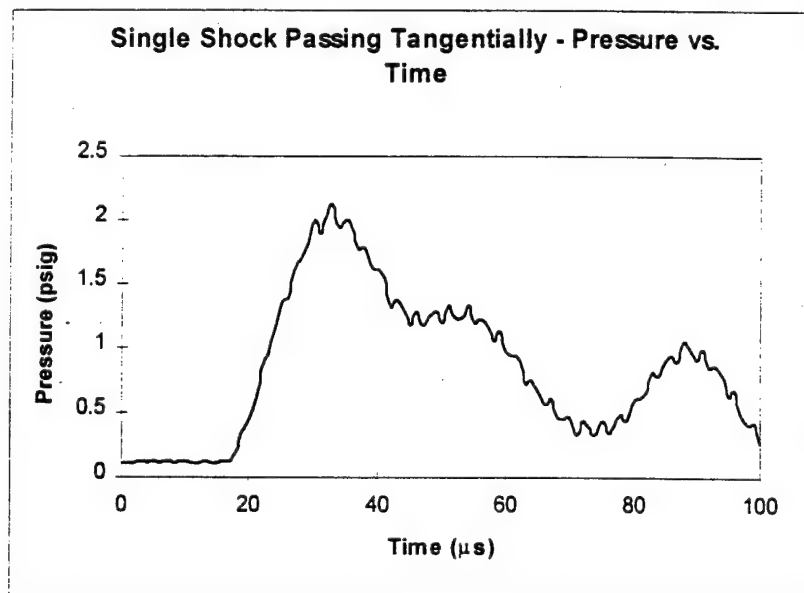


Figure 5.4  Sample Plot of Pressure for Tangentially Passing Shock Bench Test

$$q_g''(t) = \sum_{j=1}^{n} q_s''(t_j) \cdot e^{t_n - t_j / \tau} \tag{5.1}$$

for the normally impacting shock, and,

$$q_g''(t) = \sum_{i=1}^{m} \left[ \sum_{n=1}^{15} \left( q_n''(i\Delta t) \cdot e^{t_m - i\Delta t / \tau} \cdot \frac{1}{15} \right) \right] \tag{5.2}$$

for the tangentially passing shock. These two equations differ since the tangentially passing shock includes a summation over a series of 15 small segments to account for the time it takes the passing shock wave to travel across the surface of the gage.

Figure 5.5 and Figure 5.6 show the theoretical response obtained by applying the semi-infinite model developed, coupled with the first order response function for the heat flux gage, for a normally impacting shock and a tangentially passing shock, respectively. The effect that different time constants of the gage have on the theoretical response function is seen in the heat flux magnitude and in the rise time of the heat flux peak. Higher time constants yield a slower rise time, which has the effect of spreading the peak out. The rise time difference between the time constants considered is relatively small, therefore the magnitude of the heat flux response is the primary concern when comparing theoretical and experimental results. These plots demonstrate that the magnitude of the theoretical response of the heat flux gage are in better agreement with experimental results for the normally impacting shock case for a time constant of 5 μs. Conversely, the magnitude of the theoretical response for the tangentially passing shock is in better agreement with experimental results for a time constant of approximately 7 μs. The 6 μs time constant of Holmberg and Diller (1995) appears to match well for both cases and was therefore used for all comparisons.
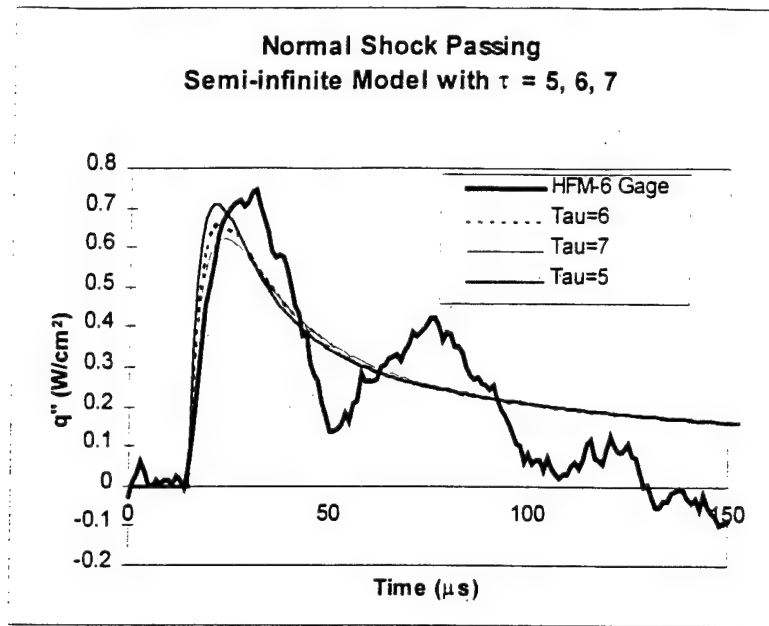
Figure 5.5  Theoretical Response Model for Normally Impacting Shock with Varying Time Constant
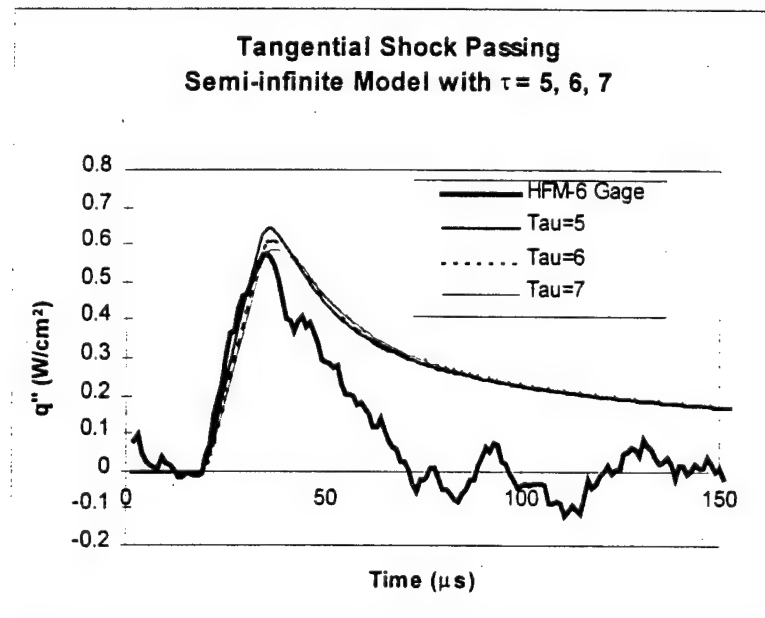


Figure 5.6  Theoretical Response Model for Tangentially Passing Shock with Varying Time Constant

## 5.2 Cascade Tests

The cascade tests performed were of three types: no flow, unheated (cold) flow, and heated flow tests. Each test was performed by introducing a moving shock of similar strength into the test section. Following is a description of the results obtained from each type of cascade test.

### 5.2.1 No flow Runs

The data from the cascade tests without flow (i.e. no-flow runs) were used to test the applicability of the theoretical response model developed for predicting heat transfer due to a passing shock in an actual cascade of blades without the complication of a boundary layer. The theoretical model discussed in Chapter 4 was developed for a flat plate as seen in the bench test rig. The applicability of this model to a more complicated geometry was tested by applying this model to the data from the no-flow runs for a heat flux gage on the pressure surface of a blade. The shock strength (in terms of pressure ratio) was determined using the two wall static pressure Kulites, and moving shock theory was applied to determine the temperature change due to the passing shock. Using the pressure and temperature information, the physical properties of the gas behind the shock were determined in order to apply the theoretical response model. Due to the complicated geometry of the blade passage, and due to residual heat flux from the initial shock passing event, the theoretical response model was not applied to subsequent reflected shock passing events in the cascade. From knowledge of the progression of the moving shock through the passage, it was determined that the initial shock passing through the cascade at gage location #2 (pressure surface) is a tangentially passing shock (Figure 5.7). This shock will effect all gage locations as a tangentially passing shock. The progression of shock waves through the cascade was analyzed through the use of shadowgraph flow visualization techniques. Further discussion of shock progression through the cascade will be presented in the flow cascade test results section. A complete

Shock Wave Passing Tangentially along Pressure Surface

Approximate Gage #2 Location

Note: Arrows indicate snock propagation direction.
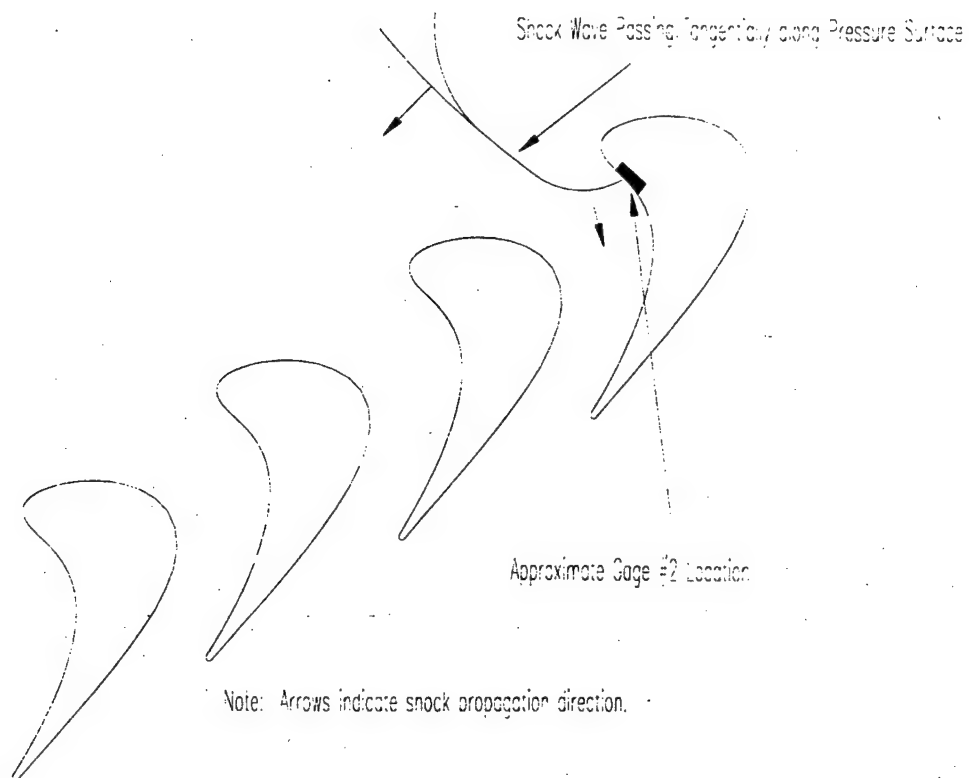
Figure 5.7  Illustration of Initial Tangentially Passing Shock

analysis of the progression of shock waves through the cascade is presented in Appendix C.

The results of the theoretical model applied to a no-flow cascade test are shown in Figure 5.8 for a sensor time constant of 6 μs at gage location #2. This location was selected at random for a test comparison to the theoretical model, and is the only location presented. The plot demonstrates that there is good agreement between the theoretical model and the experimental results. The theoretical model overpredicts the heat flux peak measured experimentally by approximately 15-20%, however, the time history of unsteady heat flux during the following 50 μs is in excellent agreement between the theoretical model and the experimental data. These results suggest that the theoretical model may be applied to a more complicated geometry and the curvature of the blades seems to have only a small effect on the theoretical model.

Comparing the results obtained for the no-flow case with the results from the bench tests demonstrate that the theoretical model better predicts the peak heat transfer in the bench test case. However, the decay of the heat flux curve obtained from the theoretical model applied to no-flow tests is in better agreement than in the bench tests for the next 100 μs. The bench tests showed good agreement in both rise time and magnitude in the peak region between 0 and 25 μs, but after this time, there is a significant difference between the experimental and theoretical results.

### 5.2.2 Unheated Runs

Unheated tunnel runs in the cascade were performed to determine the heat flux resulting from a passing shock and its corresponding reflections in the cascade in the absence of a significant temperature difference ($\Delta T_f$) between the blade surface and the flow. The unheated runs are actually "cold" runs, since typically the temperature of the flow coming from the compressed air storage tanks is slightly lower (about 2 or 3°C) than the turbine blade and cascade temperature. The unsteady pressure and heat flux time
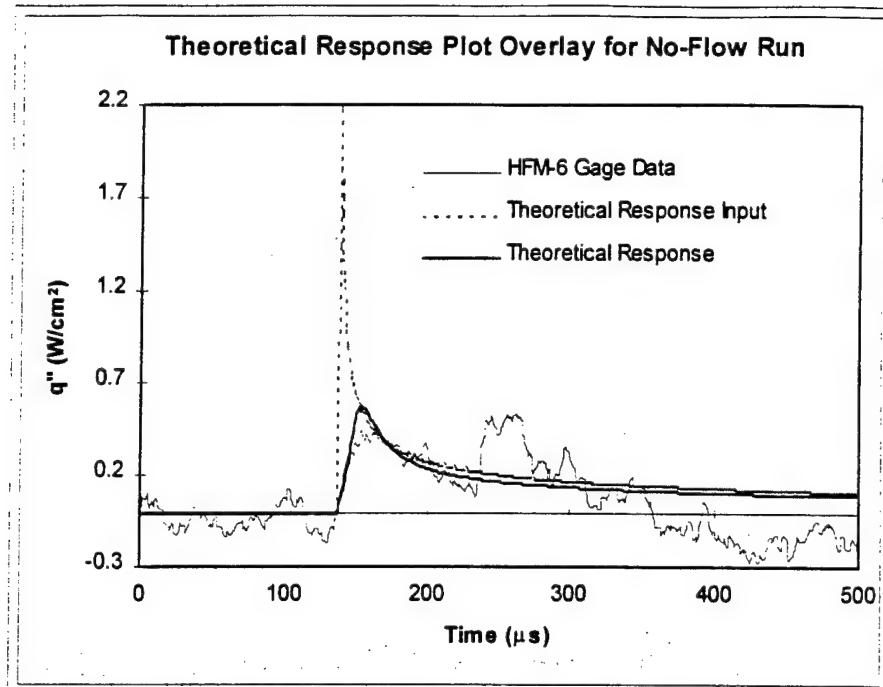
Figure 5.8 Theoretical Model Applied to No-Flow Cascade Run

history was recorded for the gage positions discussed in Chapter 3. Two of these locations, however, were discovered after experimentation to have either bad gages, or gages with a sensitivity that was insufficient to give a clean, readable signal. Due to these gage problems, data are not reported for Kulite #2 or HFM-6 gage #4. Both of these gages are on the suction surface of a blade and will be affected by a similar series of shocks and reflections as the other two gages on the same surface, therefore, it was not essential that these two gages be replaced. Sample plots of unsteady pressure and heat flux for the remaining gage locations are shown in Figures 5.9-5.14. Although heat flux data for HFM-6 gage #4 is not presented, the pressure data for this location is presented in order to demonstrate the similarity in the effects the shock wave passing event has on the different pressure surface gages. Also note that data for the sputtered heat flux gage are not presented. The sputtered gage was determined experimentally to be ineffective for capturing the passing shock. The gage is currently being studied to determine the reason for it's inability to capture shock wave passing events. The unsteady pressure, heat flux, and blade temperature data for all unheated cascade runs performed are presented in Appendix A.

The repeatability of the cascade tests was an issue to be investigated before analyzing the results of the cascade tests. To demonstrate repeatability, the pressure traces for several tests for a selected gage were overlaid on one plot to compare the results between individual cold flow cascade runs. The tunnel pressure deviates slightly between runs, typically no more than 3-4%, therefore the pressure traces were normalized by dividing by the background tunnel pressure for each run. Figure 5.15 shows the normalized unsteady pressure traces for four unheated runs overlaid for Kulite location #3. As can be seen from the plot, there is excellent repeatability in the pressure traces between cascade runs. All of the pressure peaks due to shock impact and reflections are of similar magnitudes and the time spacing between each peak for different runs is similar. These results demonstrated excellent repeatability between cascade runs.
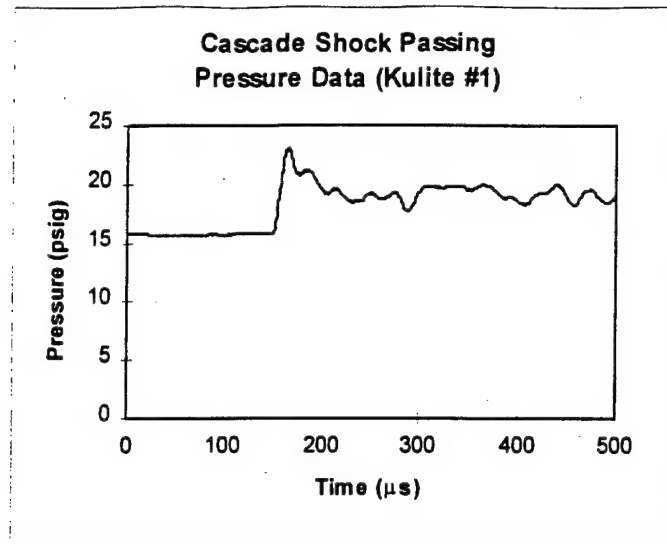
Figure 5.9  Sample Pressure Data for Kulite # 1 (Unheated Flow)
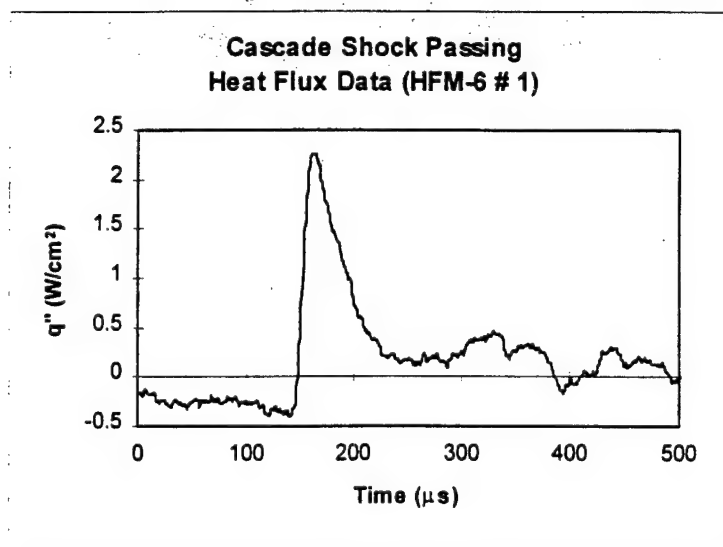


Figure 5.10  Sample Heat Flux Data for HFM #1 (Unheated Flow)
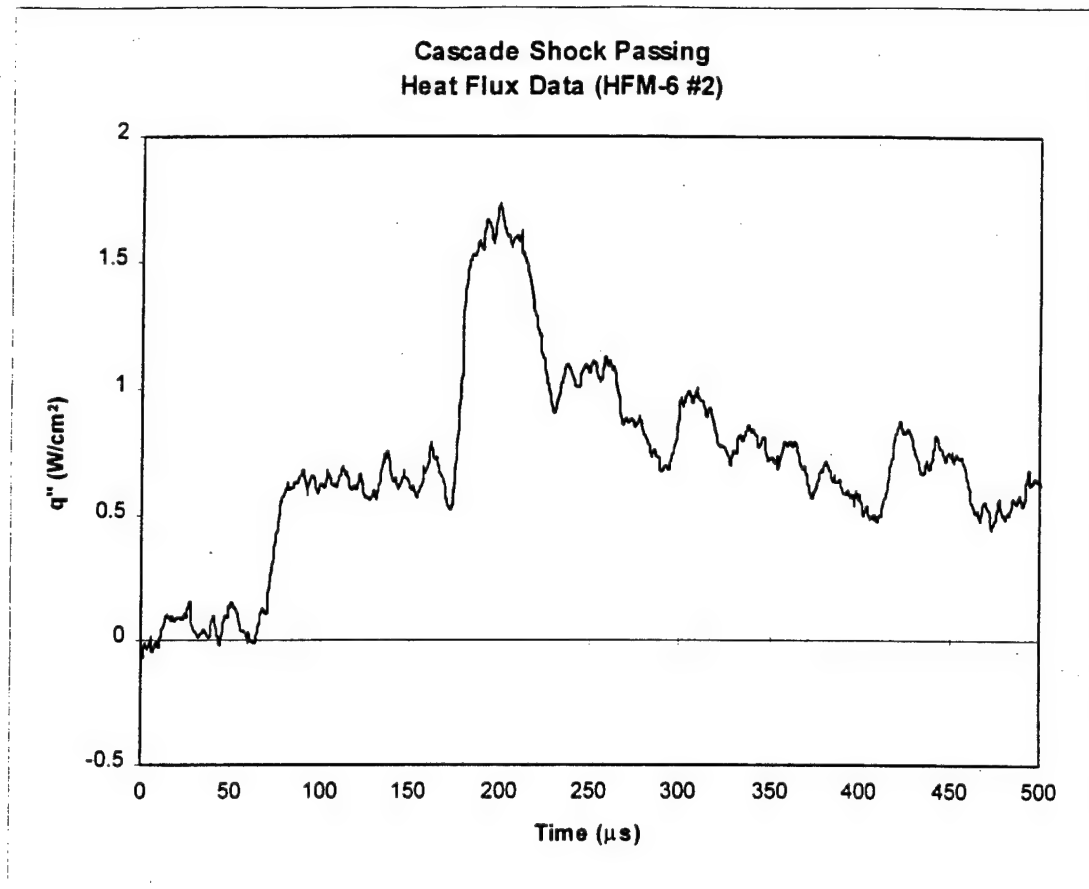
Figure 5.11 Sample Heat Flux Data for HFM #2 (Unheated Flow)

**Cascade Shock Passing**
**Pressure Data (Kulite #3)**
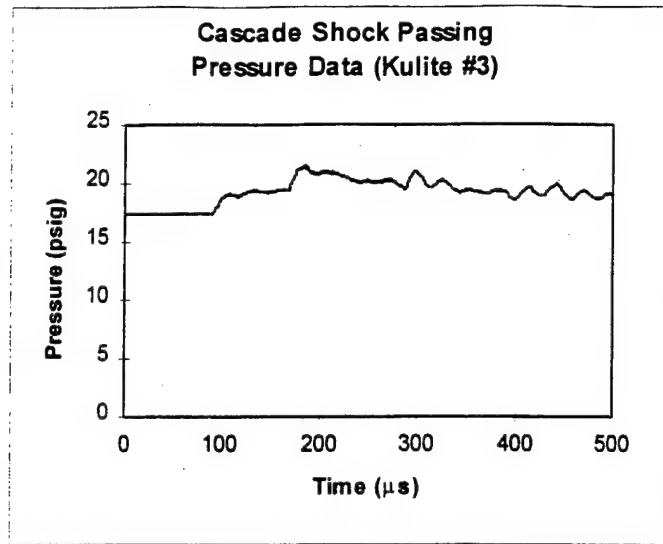
Figure 5.12  Sample Pressure Data for Kulite # 3 (Unheated Flow)

**Cascade Shock Passing**
**Heat Flux Data (HFM-6 #3)**
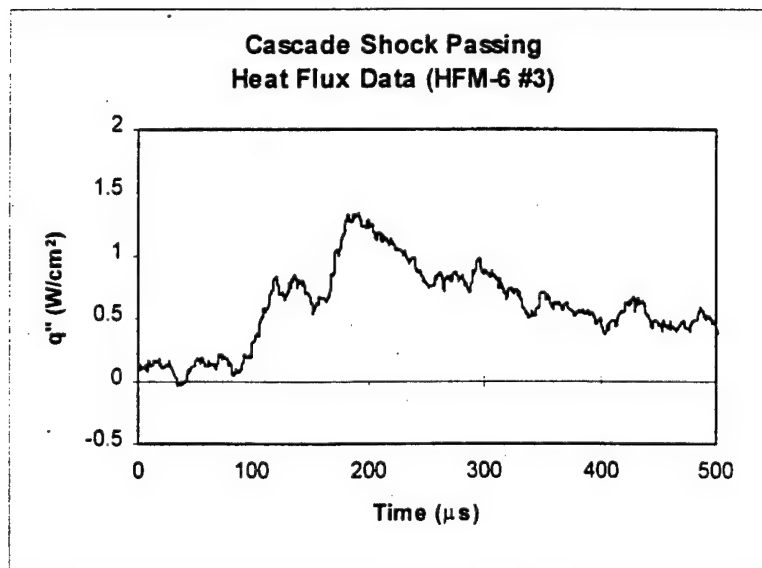
Figure 5.13  Sample Heat Flux Data for HFM #3 (Unheated Flow)
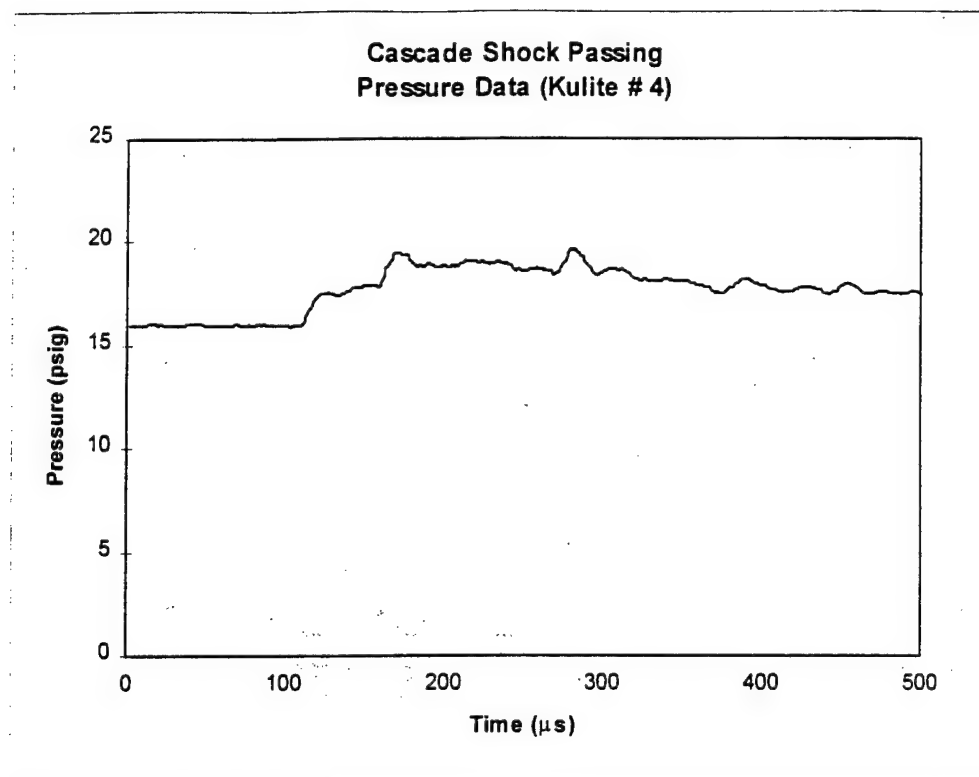
Figure 5.14  Sample Pressure Data for Kulite # 4 (Unheated Flow)
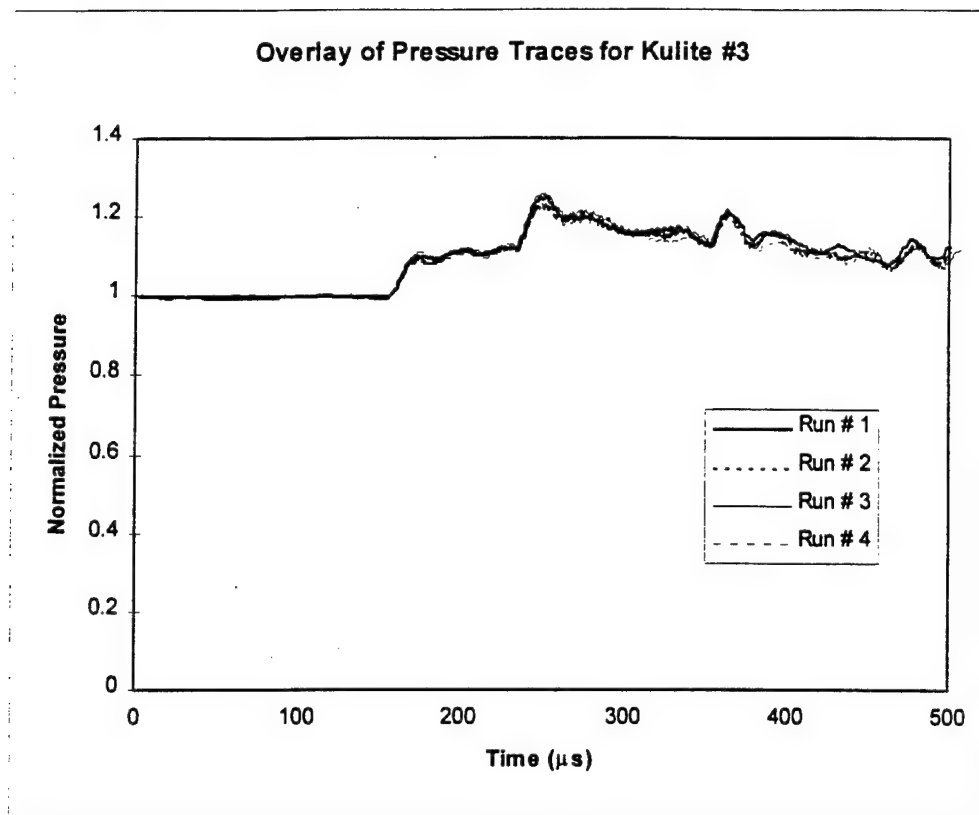
Figure 5.15  Overlay of Pressure Traces for Kulite #3

The increase in heat flux due to the passing shock was the primary concern in analyzing the unsteady heat flux data. In order to quantify the increase in heat flux, an average increase in heat flux over a given time period ($\overline{\Delta q''}$) was determined for each gage. This average increase in heat flux was calculated using the following equation:

$$\overline{\Delta q''} = \frac{\sum\limits_{i=1}^{n}\left(q''_{s_i} - \overline{q''_f}\right)}{n} \qquad [5.3]$$

where $q''_{s_i}$ is the heat flux at a given time, i, after the shock impacts the gage, n is the number of data points being used in the summation (each data point corresponds to 1 μs), and $\overline{q''_f}$ is the average heat flux between the flow and the blades before the shock passing. This average heat flux before the shock passing event was calculated using:

$$\overline{q''_f} = \frac{\sum\limits_{j=1}^{m} q''_{f_j}}{m} \qquad [5.4]$$

where $q''_{f_j}$ is the heat flux between the flow and the blades at a given time j before the shock wave passing event. Each data point corresponds to 1 μs, and a total of 150 μs of data were used to determine the average heat flux before the shock passing event (m=150). The time period used to calculate the average increase in heat flux after shock impact was determined by the time between shock passing events in a rotor with the blade profile used in this work. The time period of the shock wave passing relative to the flow in the passage is characterized by the Strouhal number which is defined by Doughty (1994):

$$St = \frac{f \cdot c_{ax}}{W}$$

[5.5]

where f is the upstream blade passing frequency (frequency of shock passing), $c_{ax}$ is the blade axial chord, and W is the blade inlet relative velocity. The Strouhal number is approximately 2.25 for a typical low pressure nozzle and 1.8 for a typical high pressure rotor (Shelton, communication w/ Doughty). Using the inlet relative Mach number of 0.36 to calculate the relative velocity, and using the axial chord of 5.08 cm (2.0 in) yields a shock passing period (1/f) of approximately 200 μs. The blade passages in the rotor of the gas turbine would see a new shock passing event every 200 μs. The unsteady heat flux increase was then averaged over this time period to determine $\overline{\Delta q''}$ since after this time a new shock wave would enter the blade passage.

The analysis discussed above was applied to HFM-6 gages #1-3 for each cascade run performed. The graphical data for each run performed is presented in Appendix A. The results for each run and each gage are shown in Tables 5.1, 5.2, and 5.3, along with the temperature difference ($\Delta T_f$) before the shock wave passing (Note that $\Delta T_f$ is relatively small and is negative):

Table 5.1  Heat Transfer Results for HFM-6 Gage #1 (Unheated Runs)

| HFM Gage # 1 (Unheated Runs) | | |
|---|---|---|
| Run # | $\Delta T_f$ (K) | $\Delta q''$ (W/cm²) |
| 1 | -3.65 | 0.7624 |
| 2 | -3.26 | 0.8344 |

Table 5.2  Heat Transfer Results for HFM-6 Gage #2 (Unheated Runs)

| HFM Gage #2 (Unheated Runs) | | |
|---|---|---|
| Run # | $\Delta T_f$ (K) | $\Delta q''$ (W/cm²) |
| 1 | -1.96 | 1.0081 |
| 2 | -3.23 | 0.7870 |
| 3 | -3.65 | 0.7236 |
| 4 | -2.06 | 0.8308 |
| 5 | -2.04 | 0.8311 |
| 6 | -2.31 | 0.8540 |
| 7 | -2.3 | 0.9444 |

Table 5.3  Heat Transfer Results for HFM-6 Gage #3 (Unheated Runs)

| HFM Gage #3 (Unheated Runs) | | |
|---|---|---|
| Run # | $\Delta T_f$ (K) | $\Delta q''$ (W/cm²) |
| 1 | -1.65 | 0.7398 |
| 2 | -1.89 | 0.7133 |
| 3 | -2.33 | 0.6311 |
| 4 | -1.74 | 0.7370 |
| 5 | -1.83 | 0.7478 |
| 6 | -2.03 | 0.6649 |

From the plots of heat flux (Figures 5.10, 5.11, and 5.13) it can be seen that there is still a residual quantity of heat flux 200 μs after the initial shock impact. Therefore, the blade passage does not see each shock passing as a separate event. Residual effects from the reflections of the previous shock are still present when the next shock enters the blade passage. The results show that the greatest increase in average heat flux over this time period occurs on the pressure surface near the leading edge (Gage location #2), where the average value of $\overline{\Delta q''}$ was determined to be approximately 0.86 W/cm².

## 5.2.3 Heated Runs

Heated tunnel runs in the cascade were performed to determine the heat flux resulting from a passing shock and its corresponding reflections in the cascade in the

presence of a significant temperature difference ($\Delta T_f$) between the blade surface and the flow. The temperature difference was varied between runs from approximately 22 K to 42 K in order to obtain a range of cases and examine the effects of flow temperature variation on shock heat transfer. Sample plots of unsteady pressure and heat flux are shown in Figures 5.16-5.21. The graphical data for all heated runs are presented in Appendix A.

The procedures for calculating the flow temperature difference, $\Delta T_f$, discussed in Chapter 2 and $\overline{\Delta q''}$, discussed in the unheated flow section, were applied to each heated run for gage locations #1-#3 to determine the average increase in heat transfer over a period of 200 μs after shock impact. The results are presented in Tables 5.4-5.6:

Table 5.4 Heat Transfer Results for HFM-6 Gage #1 (Heated Runs)

| HFM Gage # 1 (Heated Runs) | | | |
|---|---|---|---|
| Run # | $\Delta T_f$ (K) | $\Delta q''$ (W/cm²) | % Increase |
| 1 | 28.88 | 0.6060 | 40.0 |
| 2 | 32.69 | 0.7373 | 36.2 |

Table 5.5 Heat Transfer Results for HFM-6 Gage #2 (Heated Runs)

| HFM Gage #2 (Heated Runs) | | | |
|---|---|---|---|
| Run # | $\Delta T_f$ (K) | $\Delta q''$ (W/cm²) | % Increase |
| 1 | 38.77 | 1.4846 | 47.7 |
| 2 | 31.85 | 1.2049 | 50.9 |
| 3 | 27.98 | 0.9475 | 44.6 |
| 4 | 22.19 | 0.9671 | 117.3 |
| 5 | 42.44 | 1.3505 | 40.9 |
| 6 | 35.82 | 1.0736 | 45.6 |
| 7 | 30.91 | 1.0785 | 70.0 |

**Cascade Shock Passing - Heated Flow
Heat Flux Data (HFM-6 #2)**
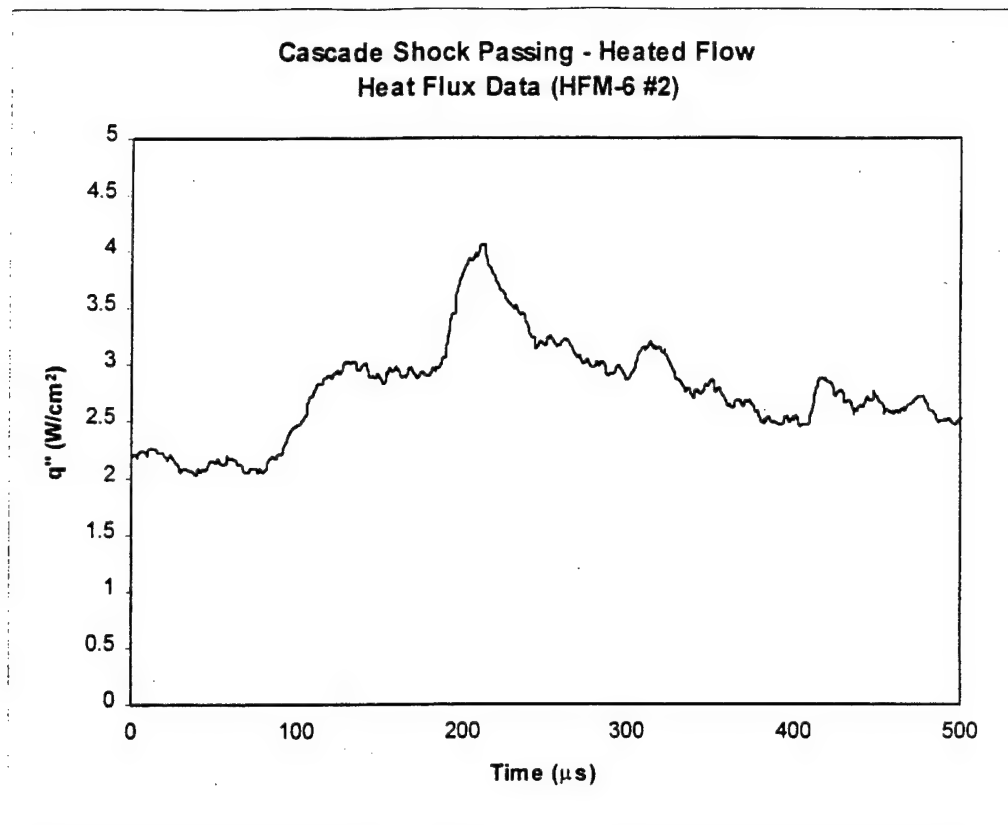
Figure 5.18 Sample Heat Flux Data for HFM #2 (Heated Flow)

**Cascade Shock Passing - Heated Flow**
**Pressure Data (Kulite #3)**
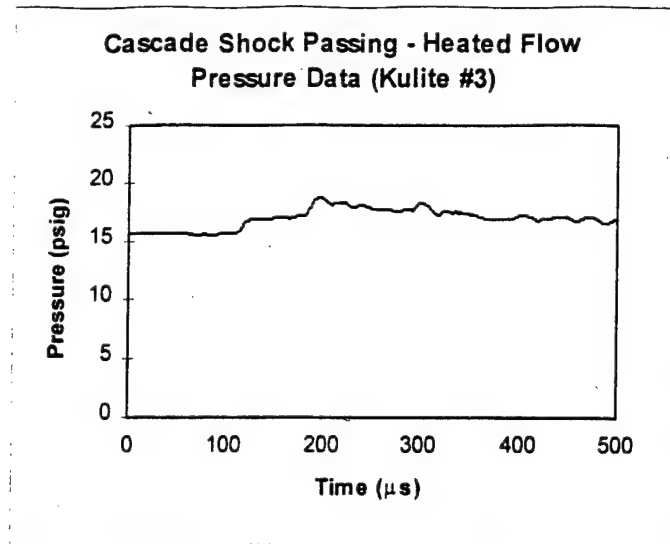
Figure 5.19  Sample Pressure Data for Kulite # 3 (Heated Flow)

**Cascade Shock Passing - Heated Flow**
**Heat Flux Data (HFM-6 #3)**
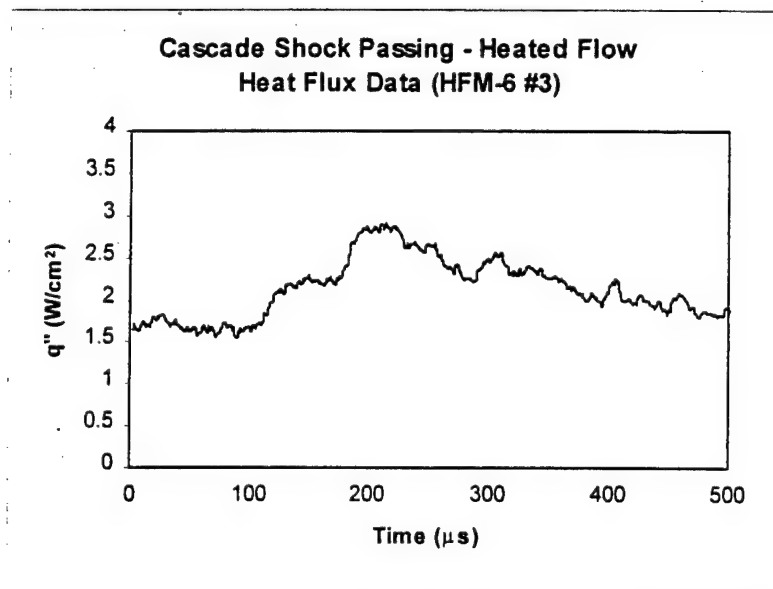
Figure 5.20  Sample Heat Flux Data for HFM #3 (Heated Flow)
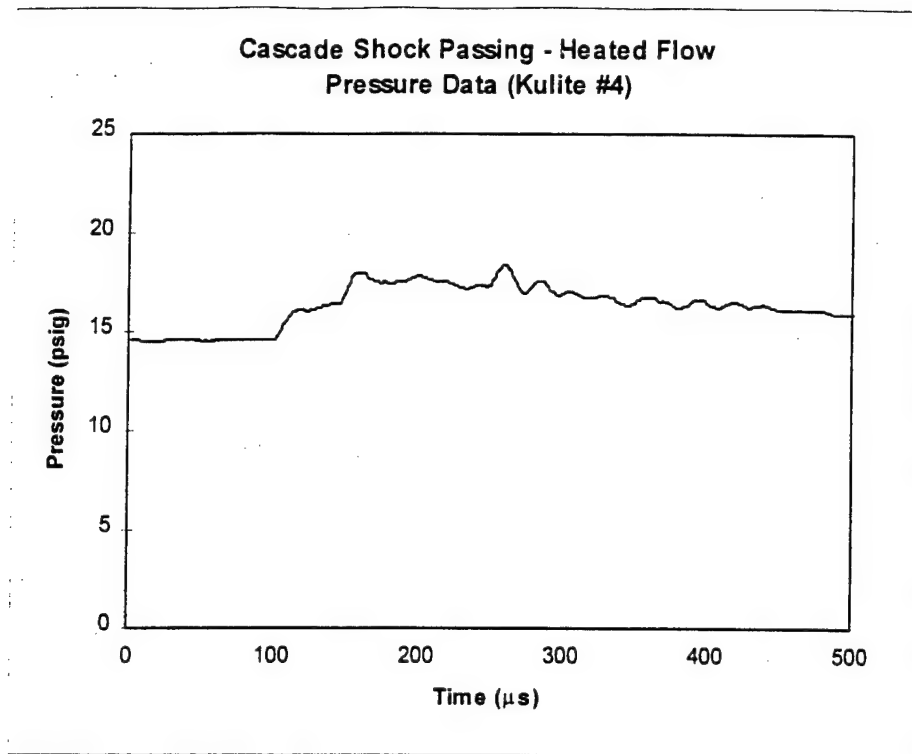
Figure 5.21  Sample Pressure Data for Kulite # 4 (Heated Flow)

Table 5.6  Heat Transfer Results for HFM-6 Gage #3 (Heated Runs)

| HFM Gage #3 (Heated Runs) | | | |
| --- | --- | --- | --- |
| Run # | $\Delta T_f$ (K) | $\Delta q"$ (W/cm$^2$) | % Increase |
| 1 | 37.93 | 1.2012 | 51.7 |
| 2 | 33.04 | 0.8556 | 45.8 |
| 3 | 29.03 | 0.7929 | 40.7 |
| 4 | 21.93 | 0.9262 | 114.7 |
| 5 | 41.69 | 1.0144 | 40.9 |
| 6 | 35.16 | 0.9896 | 53.1 |

The heated flow $\overline{\Delta q"}$ represents an average increase in heat transfer over the mean value of heat transfer before shock passing of 38.1% for gage location #1, 59.6% for gage location #2, and 58.6% for gage location #3.  Thus it can be seen that the maximum increase in heat transfer due to unsteady shock passing occurs on the pressure surface near the leading edge (Gage location #2).

# Chapter 6.0

## Discussion

### 6.1 Bench Tests

The results of the bench tests provide some insight into the heat flux resulting from a passing shock in the absence of flow and a boundary layer. Comparing the heat flux traces for the normal impacting and tangentially passing shock cases (Figure 5.1 and Figure 5.3) shows that the effects of the shock passing event persist for a longer time period in the normally impacting shock case. This is likely due to the fact that there are shock reflections present in the normally impacting shock case. The heat flux for the normally impacting shock case can also be seen to rise quicker than in the tangentially passing case. This rise time agrees with the model developed for the shock passing in relation to the heat flux gage. For the tangentially passing case, the shock must move across the surface of the gage, while the normally impacting shock is seen by the heat flux gage as a nearly instantaneous event. The experimental results validate the theoretical model and suggest that the model accurately represents the actual physics of the shock passing event. The comparison of experimental and theoretical results for the bench tests (Figures 5.5 and 5.6) demonstrate that the theoretical model and it's corresponding assumptions provide a good approximation of the experimental data and suggest that conduction through the gas as a stationary semi-infinite media is the dominant heat transfer mechanism. Johnson et al. (1989) found similar results using a model based on the same theory. Their model, however, accounted for temperature changes in the substrate (wall) due to the lower thermal conductivity of the material. They also did not incorporate a gage response model when comparing theoretical results to experimental results.

## 6.2 Cascade Tests

The results from the unheated and heated flow cascade tests presented in Chapter 5 demonstrate that there is a significant difference in the average increase in heat transfer after shock impact in the presence of a flow temperature difference ($\Delta T_f$) for pressure surface heat flux gages #2 and #3 compared to the unheated cases which have essentially no flow temperature difference.

For heated flow at gage location #2, $\overline{\Delta q''}$ is an average of 35.6% higher than the unheated flow cases at this location, and 36.5% higher at gage location #3. For the heated flow runs, there does not appear to be a direct correlation between the average increase in heat transfer ($\overline{\Delta q''}$) and the magnitude of the flow temperature difference. Figure 6.1 shows a plot of $\overline{\Delta q''}$ versus $\Delta T_f$ for all gage locations. Because $\Delta T_f$ is assumed to be a major driving force behind the heat transfer, this is a surprising result. The highest average increase in heat flux over a period of 200 µs for heated flow was seen on the pressure surface gages, with the greatest effect near the leading edge. This agrees with the numerical results of Saxer and Felici (1996), where it was determined in studies of hot streak migration due to shock passing that the time-averaged rotor stagnation pressure was larger on the pressure surface of the passage than on the suction surface.

The heated flow $\overline{\Delta q''}$ results for suction surface heat flux gage #1 (Table 5.4) demonstrate that the average increase in heat flux over a time period of 200 µs after shock impact is actually greater for the unheated flow cases (Table 5.1). This is apparently due to a greater magnitude of residual heat flux after the initial shock peak compared to the heat flux before the shock passing in the unheated runs. While the actual heat flux peak due to shock passing is greater in the heated flow case, the residual heat flux after shock passing compared to the average before shock passing is actually less in the heated case. To demonstrate this, the unsteady heat flux traces for an unheated run and a heated run
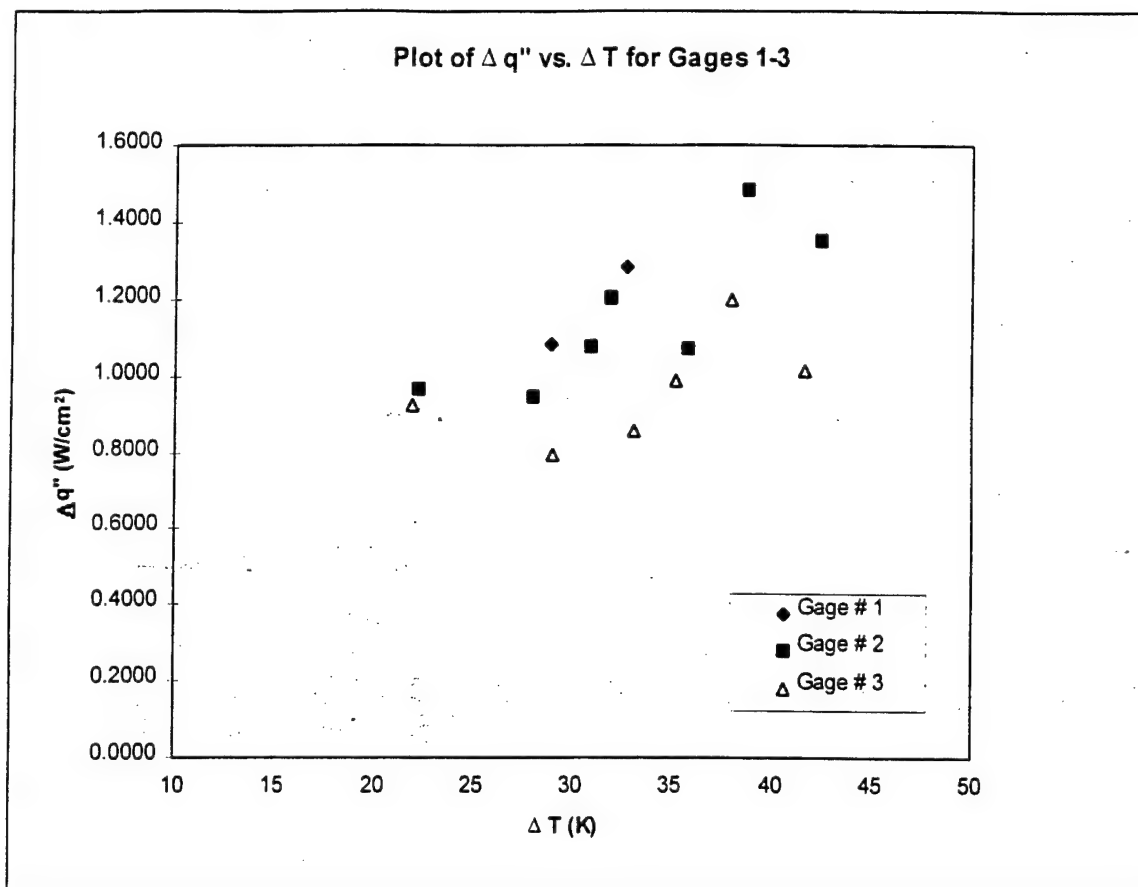
Figure 6.1 Plot of $\overline{\Delta q''}$ vs. $\Delta T_f$ for HFM-6 Gages #1-3 (Heated Flow)

Note: Gage #1 Data is averaged over 100 μs

were overlaid by offsetting the trace for the unheated run for direct comparison of the two traces (Figure 6.2). The plot demonstrates that the heated run peak in heat flux is in fact greater, but the unheated run has a higher level of residual heat flux after the peak. Therefore, when the data is averaged over a period of 200 μs, the average heat flux increase for the unheated run is greater. The heat flux peak for both types of cascade run can be seen to persist for approximately 100 μs, therefore this time period was used at gage location #1 to determine the average increase in the heat transfer for each type of run. This average will then present the magnitude of the first peak alone. Table 6.1 and 6.2 present the results for unheated and heated cascade runs, respectively:

Table 6.1  Heat Transfer Analysis Results for HFM-6 Gage #1

(Unheated Runs, 100 μs averaging period)

| HFM Gage # 1 (Unheated Runs) | | |
|---|---|---|
| Run # | $\Delta T_f$ (K) | $\Delta q$" (W/cm$^2$) |
| 1 | -3.65 | 1.0689 |
| 2 | -3.26 | 1.0676 |

Table 6.2  Heat Transfer Analysis Results for HFM-6 Gage #1

(Heated Runs, 100 μs averaging period)

| HFM Gage # 1 (Heated Runs) | | |
|---|---|---|
| Run # | $\Delta T_f$ (K) | $\Delta q$" (W/cm$^2$) |
| 1 | 28.88 | 1.0860 |
| 2 | 32.69 | 1.2836 |

These results demonstrate that the difference in heat flux increase due to shock effects between heated flow and cold flow are not as large for the suction surface gage as the pressure surface gages. This may be due to the very high acceleration of the flow on the suction surface near the crown of the blade. When averaged over 100 μs, the $\overline{\Delta q''}$
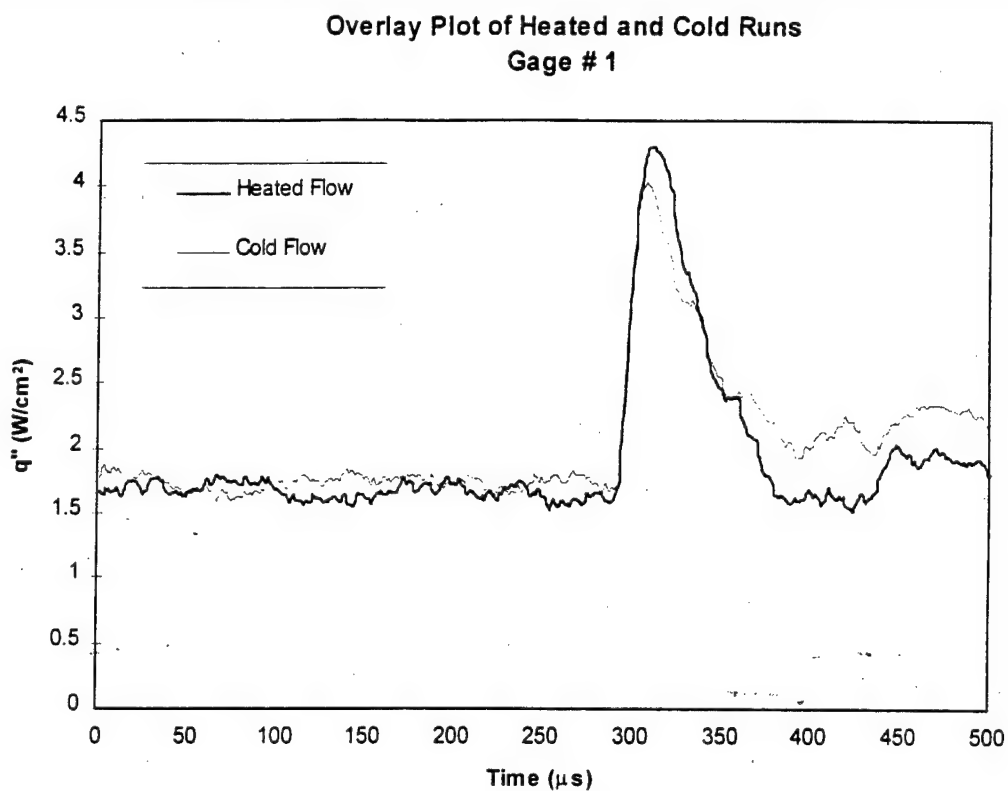
Figure 6.2  Overlay Plot of Heated and Unheated Cascade Runs for HFM-6 Gage #1

for the suction surface gage represents an increase in heat transfer of 79.5% over the mean value before shock passing. This demonstrates that the heat transfer increase due to shock impact on the suction surface near the leading edge is very high, but has a very fast decay time compared to the pressure surface gages.

## 6.3 Shock Heat Transfer

To further understand the shock passing events, it was assumed that the effects on heat transfer of a shock impacting a surface are two-fold. First is the increase in temperature of the gas behind the shock, which will be referred to as shock heating. Second is the physical disruption of the boundary layer, which will increase the normal boundary layer heat transfer. This will be termed boundary layer disturbance. In an attempt to quantify the increase in heat transfer due to boundary layer disturbance and understand the mechanisms of shock heat transfer, an analysis was performed on the data employing the unheated and heated cascade runs coupled together. Heat transfer in the unheated flow cases is assumed to be a result of shock heating only. The heat transfer occurring before shock passing is very small and was therefore neglected. Heat transfer due to shock heating for the unheated flow cases can be written as follows:

$$q''_{shock} \text{ (Unheated Flow)} = q''_{\Delta T_s} \qquad [6.1]$$

where $q''_{\Delta T_s}$ is the heat transfer due to the temperature increase across the shock (shock heating), including heat transfer due to boundary layer disturbance with $\Delta T_s$ as the driving force. Assuming the effects of shock heating and boundary layer disturbance can be separated and are additive, the heat transfer for the heated cases can be written as:

$$q''_{shock} \text{ (Heated Flow)} = q''_{\Delta T_s} + q''_{\Delta T_f} + q''_{BL_f} \qquad [6.2]$$

where $q''_{\Delta T_f}$ is the heat transfer which is present before the shock passing due to a flow temperature difference and $q''_{BL_f}$ is the increase in heat flux due to boundary layer disturbance by the shock impact with the flow temperature difference ($\Delta T_f$) as the driving force. If the unheated flow case were subtracted from the heated flow case, the result would have the effect of removing the heat transfer due to shock heating. Thus what remains would be approximately equivalent to the heat transfer due to the flow temperature difference before shock passing and the increase in heat transfer due to boundary layer disturbance:

$$q''_{shock}\ (\text{Heated - Unheated Flow}) = q''_{\Delta T_f} + q''_{BL_f} \qquad\qquad [6.3]$$

In order to obtain this result, the shock heating in unheated and heated flow was assumed to be the same. Figures 6.3-6.5 graphically demonstrate the application of this analysis. The plots present the unsteady heat flux traces for heated runs, unheated runs, and the difference between the two runs. Results for all data runs are presented in Appendix A. If the analysis described in Chapter 5 for calculating $\overline{\Delta q''}$ is then applied, the $q''_{\Delta T_f}$ term will be subtracted off since this term is the average heat transfer occurring before shock passing, leaving only the average increase due to boundary layer disturbance with the flow temperature difference as the driving force ($\overline{q''_{BL_f}}$). This analysis will then separate out the boundary layer disturbance effects from the shock heating effects.

The difference between the unsteady heat flux traces for heated and unheated flow (Figures 6.3-6.5) was calculated by subtracting the $\overline{\Delta q''}$ results for unheated flow (Tables 6.1, 5.2, and 5.3) from the results for heated flow (Tables 6.2, 5.5, and 5.6). The $\overline{\Delta q''}$ calculated for each type of run then corresponds to the analysis presented above in the following way:
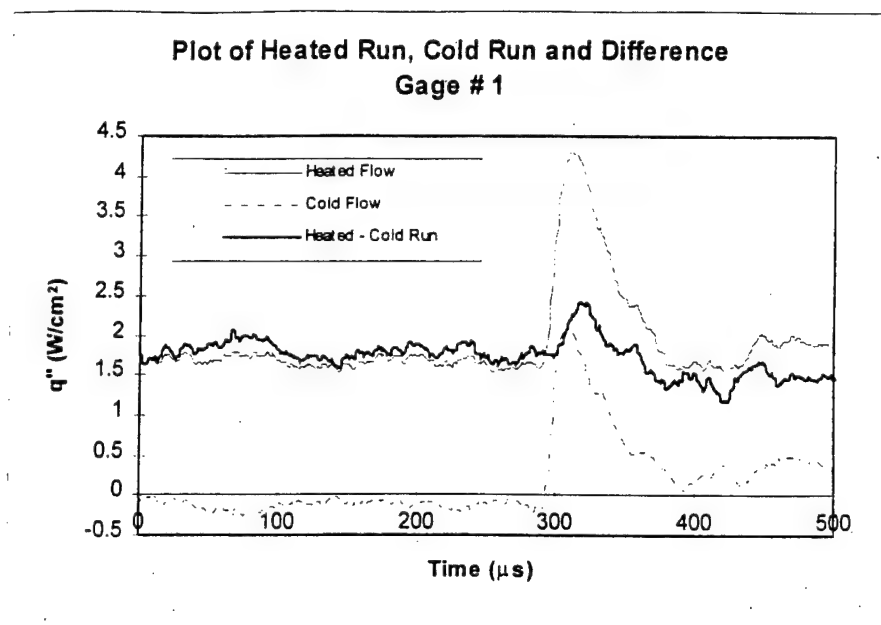
**Plot of Heated Run, Cold Run and Difference**
**Gage # 1**



Figure 6.3 Plot of Heat Flux for Heated Runs, Unheated runs, and Difference for HFM-6
Gage #1

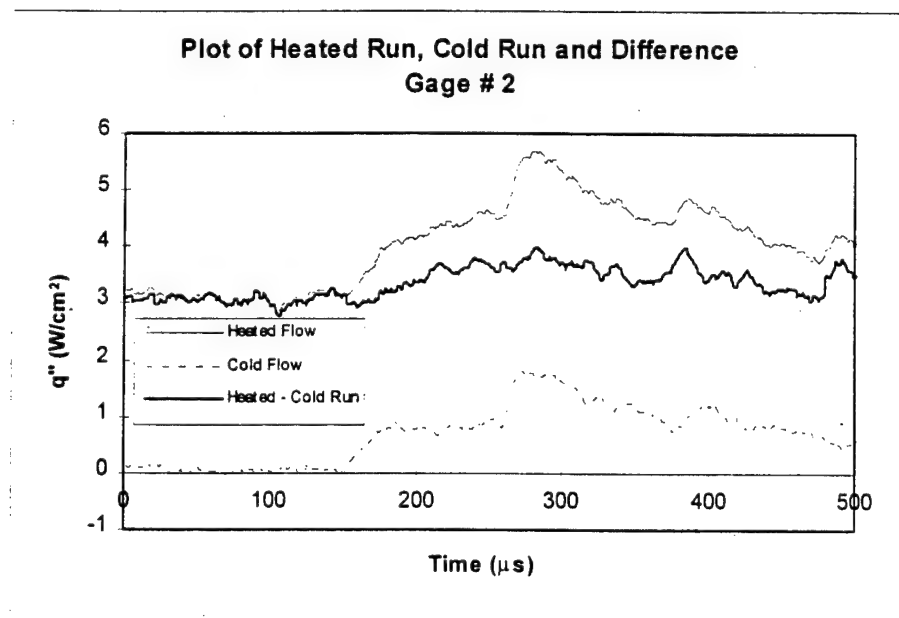**Plot of Heated Run, Cold Run and Difference**
**Gage # 2**



Figure 6.4 Plot of Heat Flux for Heated Runs, Unheated runs, and Difference for HFM-6
Gage #2

**Plot of Heated Run, Cold Run and Difference**
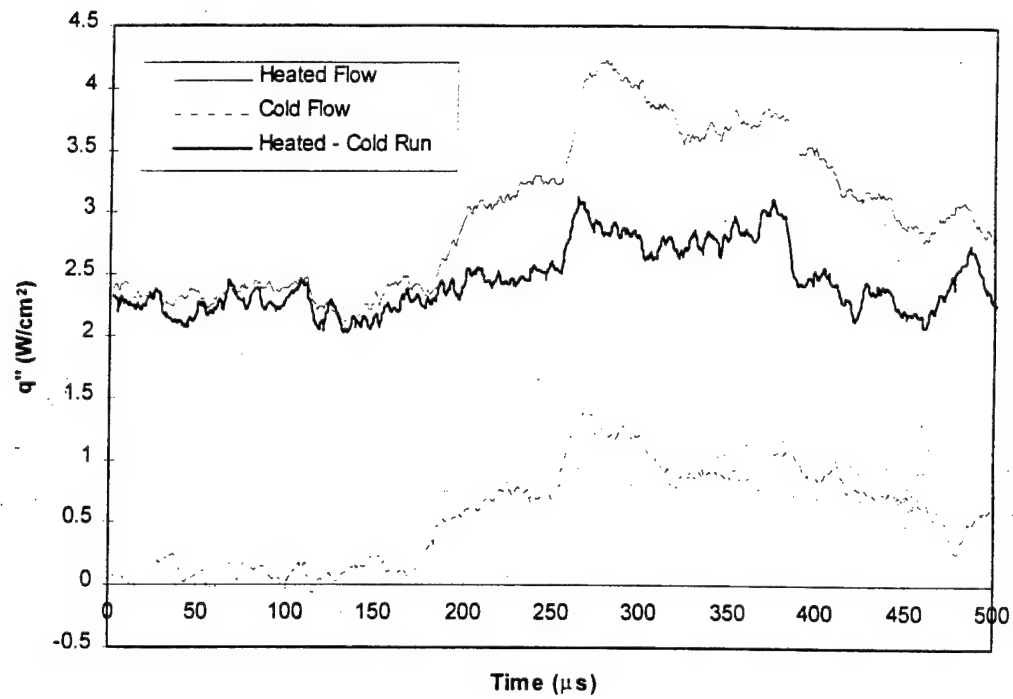**Gage # 3**

Figure 6.5  Plot of Heat Flux for Heated Runs, Unheated runs, and Difference for HFM-6
Gage #3

$$\overline{\Delta q''} \text{ (Unheated Flow)} = \overline{q''_{\Delta T_s}} \qquad\qquad [6.4]$$

$$\overline{\Delta q''} \text{ (Heated Flow)} = \overline{q''_{\Delta T_s} + q''_{BL_f}} \qquad\qquad [6.5]$$

$$\overline{\Delta q''} \text{ (Heated - Unheated Flow)} = \overline{q''_{BL_f}} \qquad\qquad [6.6]$$

Tables 6.3-6.5 present the data averaged over 200 µs for gages #2 and #3 and over 100 µs for gage #1 along with the flow temperature difference for the heated run:

Table 6.3  Heat Transfer Analysis Results for HFM-6 Gage #1

(Unheated Runs, Heated Runs, and Difference, 100 µs averaging period)

| HFM Gage # 1 | | | | | | |
|---|---|---|---|---|---|---|
| | Cold Flow | | Heated Flow | | Heated-Cold Flow (BL Disturbance Effects) | | |
| Run # | $\Delta T_f$ (K) | $\Delta q''$ (W/cm²) | $\Delta T_f$ (K) | $\Delta q''$ (W/cm²) | $\Delta q''$ (W/cm²) | $\Delta h$ (W/m²K) | $\Delta h/h$ (%) (h=1000 W/m²K) |
| 1 | -3.65 | 1.0689 | 28.88 | 1.0860 | 0.0171 | 5.92 | 0.59% |
| 2 | -3.26 | 1.1676 | 32.69 | 1.2836 | 0.1160 | 35.48 | 3.55% |
| 3 | -3.65 | 1.0689 | 32.69 | 1.2836 | 0.2147 | 65.68 | 6.57% |

Table 6.4  Heat Transfer Analysis Results for HFM-6 Gage #2

(Unheated Runs, Heated Runs, and Difference, 200 µs averaging period)

| HFM Gage #2 | | | | | | |
|---|---|---|---|---|---|---|
| | Cold Flow | | Heated Flow | | Heated-Cold Flow (BL Disturbance Effects) | | |
| Run # | $\Delta T_f$ (K) | $\Delta q''$ (W/cm²) | $\Delta T_f$ (K) | $\Delta q''$ (W/cm²) | $\Delta q''$ (W/cm²) | $\Delta h$ (W/m²K) | $\Delta h/h$ (%) (h=820 W/m²K) |
| 1 | -1.96 | 1.0081 | 38.77 | 1.4846 | 0.4765 | 122.90 | 14.63% |
| 2 | -3.23 | 0.7870 | 31.85 | 1.2049 | 0.4179 | 131.21 | 15.62% |
| 3 | -3.65 | 0.7236 | 27.98 | 0.9475 | 0.2239 | 80.02 | 9.53% |
| 4 | -2.06 | 0.8308 | 22.19 | 0.9671 | 0.1363 | 61.42 | 7.31% |
| 5 | -2.04 | 0.8311 | 42.44 | 1.3505 | 0.5194 | 122.38 | 14.57% |
| 6 | -2.31 | 0.8540 | 35.82 | 1.0736 | 0.2196 | 61.31 | 7.30% |
| 7 | -2.3 | 0.9444 | 30.91 | 1.0785 | 0.1341 | 43.38 | 5.16% |

Table 6.5  Heat Transfer Analysis Results for HFM-6 Gage #3

(Unheated Runs, Heated Runs, and Difference, 200 μs averaging period)

| | HFM Gage #3 | | | | | | |
|---|---|---|---|---|---|---|---|
| | Cold Flow | | Heated Flow | | Heated-Cold Flow (BL Disturbance Effects) | | |
| Run # | $\Delta T_f$ (K) | $\Delta q"$ (W/cm²) | $\Delta T_f$ (K) | $\Delta q"$ (W/cm²) | $\Delta q"$ (W/cm²) | $\Delta h$ (W/m²K) | $\Delta h/h$ (%) (h=840 W/m²K) |
| 1 | -1.65 | 0.7398 | 37.93 | 1.2012 | 0.4614 | 121.65 | 14.14% |
| 2 | -1.89 | 0.7133 | 33.04 | 0.8556 | 0.1423 | 43.07 | 5.01% |
| 3 | -2.33 | 0.6311 | 29.03 | 0.7929 | 0.1618 | 55.74 | 6.48% |
| 4 | -1.74 | 0.7370 | 21.93 | 0.9262 | 0.1892 | 86.27 | 10.03% |
| 5 | -1.83 | 0.7478 | 41.69 | 1.0144 | 0.2666 | 63.95 | 7.44% |
| 6 | -2.03 | 0.6649 | 35.16 | 0.9896 | 0.3247 | 92.35 | 10.74% |

The data was converted to an average increase in heat transfer coefficient ($\Delta h$) by dividing the value of $\overline{\Delta q"}$ by $\Delta T_f$. The percentage increase this represents over the heat transfer coefficient for each particular gage location was calculated by dividing by the undisturbed heat transfer coefficient ($\overline{h}$) for each location. These heat transfer coefficients were determined in previous work. It can be seen from these results that the percentage increase in heat transfer due to boundary layer disturbance from shock passing with the flow temperature difference ($\Delta T_f$) as the driving force is between 5-10% for both pressure and suction surface gage locations. This suggests that the shock does not have a large effect on the boundary layer and heat transfer increase due to shock wave passing is primarily a result of shock heating. This does not agree with the findings of Doorly and Oldfield (1985), where it was reported that direct shock impingement had little effect on heat transfer, rather the propagation of a turbulent patch caused by a boundary layer separation bubble had the most profound effect on heat transfer.

The theoretical model developed and described in Chapter 4 was applied to unheated and heated flow cascade tests to check the models applicability in predicting heat transfer due to shock heating. Figures 6.6 and 6.7 show the model applied to

unheated and heated flow cascade tests, respectively. The plots demonstrate that the theoretical model does not agree well with experimental data. This could be due to the fact that heat transfer in the flow cascade tests is by forced convection, while the theoretical model is based on conduction in a semi-infinite medium. Also, one of the primary assumptions in the theoretical model is that heat transfer is from a stagnant gas to the blade wall, while the cascade tests were performed with transonic flow, violating the stagnant gas assumption. Johnson Et al. (1989) developed a similar model employing conduction through the boundary layer as the principal heat transfer mechanism and applied this model to cases with flow through the cascade. Heat transfer fluctuations by conduction from the hot gas immediately next to the blade surface were estimated using this model. In addition, a model of the compression and expansion of the embedded time mean temperature gradient profile in the boundary layer which gives rise to modulations of heat transfer rate by the surface pressures was developed. These two models of heat transfer increase mechanisms were added together to give the total increase in heat transfer due to shock passing and were then compared to experimental data with good results.

## 6.4 Application to Gas Turbine Engines

The results presented in Chapter 5 and discussed here may be applied to full scale gas turbine engines with some considerations. The shock heating effect, heat transfer increase due to temperature ratio of the shock, was determined experimentally to be the primary mechanism by which passing shock waves increase the time-averaged heat transfer in the cascade experiments. The driving force behind this heat transfer increase is the temperature ratio of the shock wave. The shocks used in experimentation have a pressure ratio similar to the shock waves in a real gas turbine, therefore, the temperature ratio of the shocks in a gas turbine will be similar to the shocks in this work. The temperature difference across a shock wave of this strength will scale according to the flow temperature as follows:

$$\frac{T_2}{T_1} \approx 1.05 \qquad\qquad [6.7]$$

where $T_1$ is the flow temperature (temperature before shock passing) and $T_2$ is the temperature after shock passing. The temperature difference across the shock, $\Delta T_s$, is as follows:

$$\Delta T_s = T_2 - T_1 = 0.05 \cdot T_1 \qquad\qquad [6.8]$$

The heat flux increase due to shock passing is proportional to the shock temperature difference which depends on the flow temperature before shock passing ($q''_s \propto \Delta T_s \propto 0.05 \cdot T_1$). The heat flux before shock passing is as follows:

$$q''_f = h \cdot (T_r - T_s) = h \cdot T_s \cdot (\frac{T_r}{T_s} - 1) \qquad\qquad [6.9]$$

where $T_r$ is the recovery temperature and is calculated from the flow temperature $T_1$ (Eq. 2.10). The temperature ratio ($T_r/T_s$) for a typical gas turbine is approximately 1.4 (Johnson and Diller, 1995), while typical values used in this work were approximately 1.1. Since the temperature ratio is lower for the experiments performed in this work, $q''_f$ is lower than it would be in a full scale gas turbine at similar flow temperatures. Therefore, the percent increase in heat flux due to shock passing ($\overline{\Delta q''_s}/q''_f$) will be lower in a full scale gas turbine than the values presented in this work.

The shock progression analysis presented in Appendix C is believed to be similar to that present in a real gas turbine, since the results of this work, numerical work by Saxer and Felici (1996), and work by Johnson et al. (1990) (using a rotating bar rig) all agree on the progression of shock waves and their reflections through the cascade. The real gas turbine would, however, present a slightly more complex series of shock waves, since this analysis was done for an isolated shock wave, while a full scale turbine would see a new shock wave each time a new turbine blade passes upstream of the blade passages.

# Chapter 7.0

## Conclusions and Recommendations

### 7.1 Conclusions

The effects of the passing of a relatively weak shock on heat flux in a transonic cascade have been measured using new thin-film HFM-6 heat flux microsensors. The procedure described in this work for producing and introducing shocks into a stationary cascade is unique, and has definite advantages over the rotating bar method. The biggest advantage is the ability to introduce an isolated shock or to introduce a series of traveling shocks, without the presence and complications of a wake. The work was designed to understand the heat transfer processes which occur in a gas turbine engine and are applicable to a full scale turbine under real operating conditions.

The results show an average increase in heat flux of 1.1581 $W/cm^2$ and 0.8541 $W/cm^2$, for heated and unheated flow, respectively, at gage location #2 (suction surface near the leading edge) over a period of 200 µs. This represents an average of 59.6% increase in the steady state value of heat flux for heated flow. The effects of shock-boundary layer interaction on the mean heat transfer were, through an analysis coupling heated and unheated results, determined to be minimal, with a maximum average increase in heat transfer of 10.6% at gage location #2.

A theoretical model for predicting the heat transfer due to shock wave passing or impingement in the absence of flow and without complications of a boundary layer was developed. The model employed a semi-infinite medium conduction assumption to predict the time-resolved heat flux history due to shock passing. The theoretical model results demonstrated good agreement with experimental tests for both a series of simplified flat plate bench tests and no-flow cascade tests. It was determined, however, that the model does not give good results when applied to cascade runs with flow.

The progression of shock waves and their corresponding reflections were analyzed and tracked over time (Appendix C). This shock progression also agrees well with the progression seen in numerical results reported by Saxer and Felici (1996). The documentation of the progression of shocks through the cascade blade passages is a useful tool to be applied to continuing work in shock heat transfer studies in stationary turbine cascades.

## 7.2 Recommendations

Recommendations for future work are summarized as follows:

The unsteady heat flux history for pressure surface HFM gages #2 and #3 was shown to have a significant amount of residual heat flux 200 μs after the initial increase in heat flux due to shock impact. The period of 200 μs was determined through analysis of the Strouhal number for the cascade blades to be the period between individual shock events entering the blade passages. This residual heat flux suggests that the effects of shock impact on pressure surface heat transfer will persist while another shock enters the passage. Therefore, the effects of consecutive shocks could combine to create a further increase in unsteady heat flux than that measured for a single shock event. It is recommended, therefore, that continuing research should focus on the introduction of multiple shock waves, separated by a time period of approximately 200 μs, and the effects that this series of shocks have on heat transfer in the cascade. The test facility described in this work has the capability of producing and introducing up to three shock waves separated in time. The set-up and procedure for the production of multiple shock waves with the shock tube-shock shaper configuration is outlined in previous work by Doughty (1994).

# References

Ashworth, D. A., LaGraff, J. E., Schultz, D. L., and Grindrod, K. J., "Unsteady Aerodynamic and Heat Transfer Processes in a Transonic Turbine Stage." ASME Paper 85-GT-128, 1985.

Baker, K. I. and Diller, T. E., "Unsteady Heat Flux and Temperature Measurements." ASME/AIChE National Heat Transfer Conference, 1993.

Diller, T. E., "Advances in Heat Flux Measurements." Advances in Heat Transfer, Vol. 23, Academia Press, New York, 1993, pp. 279-368.

Doorly, D. J. and Oldfield, M. L. G., "Simulation of the Effects of Shock Wave Passing on a Turbine Rotor Blade." ASME Paper 85-GT-112, 1985.

Doughty, R. L., Schetz, J. A., and Moses, H. L., "Multiple Shock Wave Generation for Cascade Testing." Presented at the 33rd Aerospace Sciences Meeting and Exhibit, January 9-12, 1995.

Doughty, R. L., "Effects of Multiple Incident Shock Waves on the Flow in a Transonic Cascade." Ph.D. Dissertation, Virginia Polytechnic Institute and State University, Blacksburg, VA, 1994.

Hager, J. M., Onishi, S., Langley, L. W., and Diller, T. E., "High Temperature Heat Flux Measurements." AIAA Paper 91-0165, 1991a.

Hager, J. M., Simmons, S., Smith, D., Onishi, S., Langley, L. W., and Diller, T. E., "Experimental Performance of a Heat Flux Microsensor." *ASME Journal of Engineering for Gas Turbines and Power*, Vol. 113, 1991b, pp. 246-250.

Hale, J. H., "Effects of Stationary Wake on Turbine blade Heat Transfer in a Transonic Cascade." M.S. Thesis, Virginia Polytechnic Institute and State University, Blacksburg, VA, 1996.

Hayashi, H., Aso, S., and Tan, A., "Fluctuation of Heat Transfer in Shock Wave/Turbulent Boundary Layer Interaction." *AIAA Journal*, Vol. 27, 1989, pp. 399-404.

Holmberg, D.G., and Diller, T. E., "High Frequency Heat Flux Sensor Calibration and Modeling." *ASME Journal of Fluids Engineering*, Vol. 117, December 1995, pp. 659-664.

Holmberg, D. G. et al. "Effects of Shock Wave Passing on Heat Transfer in a Transonic Turbine Cascade." Presented at the 39th ASME/IGTI Congress and Exposition, June 13-16, 1994.

Incropera, F. P., and DeWitt, D. P., Fundamentals of Heat and Mass Transfer, John Wiley and Sons, New York, 1990, p. 259-262.

Johnson, A. B., Oldfield, M., Rigby, M., and Giles, M. "Nozzle Guide vane Shock Wave Propagation and Bifurcation in a Transonic Turbine Rotor." ASME Paper 90-GT-310, 1990.

Johnson, A., Rigby, M., Oldfield, M., Ainsworth, R. and Oliver, M., "Surface Heat Transfer Fluctuations on a Turbine Rotor Blade Due to Upstream Shock Wave Passing." *ASME Journal of Turbomachinery*, Vol. 111, 1989, pp. 105-115.

Johnson, L. P., and Diller, T. E., "Effects of Freestream Turbulence on Turbine Blade Heat Transfer in Transonic Flow." M.S. Thesis, Virginia Polytechnic Institute and State University, Blacksburg, VA, 1995.

Johnson, L. P., and Diller, T. E., "Measurements with a Heat Flux Microsensor Deposited on a Transonic Turbine Blade." IEEE Paper 95CH3482-7, 1995.

Peabody, H., FORTRAN Code - RESP2REV.FOR, Virginia Tech, 1996.

Rigby, M . J., Johnson, A. B., and Aldfield, M. L. G., "Gas Turbine Rotor Blade Film Cooling With and Without Simulated NGV Shock Waves and Wakes." ASME Paper 90-GT-78, 1990.

Saxer, A. P., and Felici, H. M., "Numerical Analysis of Three-Dimensional Hot Streak Migration and Shock Interaction in a Turbine Stage.", *ASME Journal of Turbomachinery*, Vol. 118, April 1996, pp. 268-277.

Seiverding, C. H., and Cicatelli, G., "A Review of the Research on Unsteady Turbine Blade Wake Characteristics." AGARD Conference 1995.

Shapiro, A. H., The Dynamics and Thermodynamics of Compressible Fluid Flow, Vol. I, Roland Press Co., New York, 1953, pp. 59-68.

Shapiro, A. H., The Dynamics and Thermodynamics of Compressible Fluid Flow, Vol. II, Roland Press Co., New York, 1954, pp. 995-998.

Shelton, M. L. Personal communication with R. Doughty.

Simmons, S. G., Hager, J. M., and Diller, T. E., "Simultaneous Measurements of Time-Resolved Surface Heat Flux and Freestream Turbulence at a Stagnation Point." *ASME Journal of Engineering for Gas Turbines and Power*, Vol. 112, 1990, pp. 375-380.

Zucker, R. D., Fundamentals of Gas Dynamics, Matrix Publishers, Inc., Chesterland, OH, 1977, pp. 172-176.

# Appendix A

## Data Runs

This appendix contains the data for all runs, both bench test and cascade no-flow, unheated and heated runs. The Appendix is broken up into sections as follows:

1. **Bench Tests**
2. **No-Flow Cascade Runs**
3. **Unheated Cascade Runs**
4. **Heated Cascade Runs**
5. **Comparison of Heated and Unheated Runs**

# 1. Bench Tests

# 2. No-Flow Cascade Runs

**No Flow Cascade Shock Passing
Pressure Data (K1 - 9/12 - Run 2)**
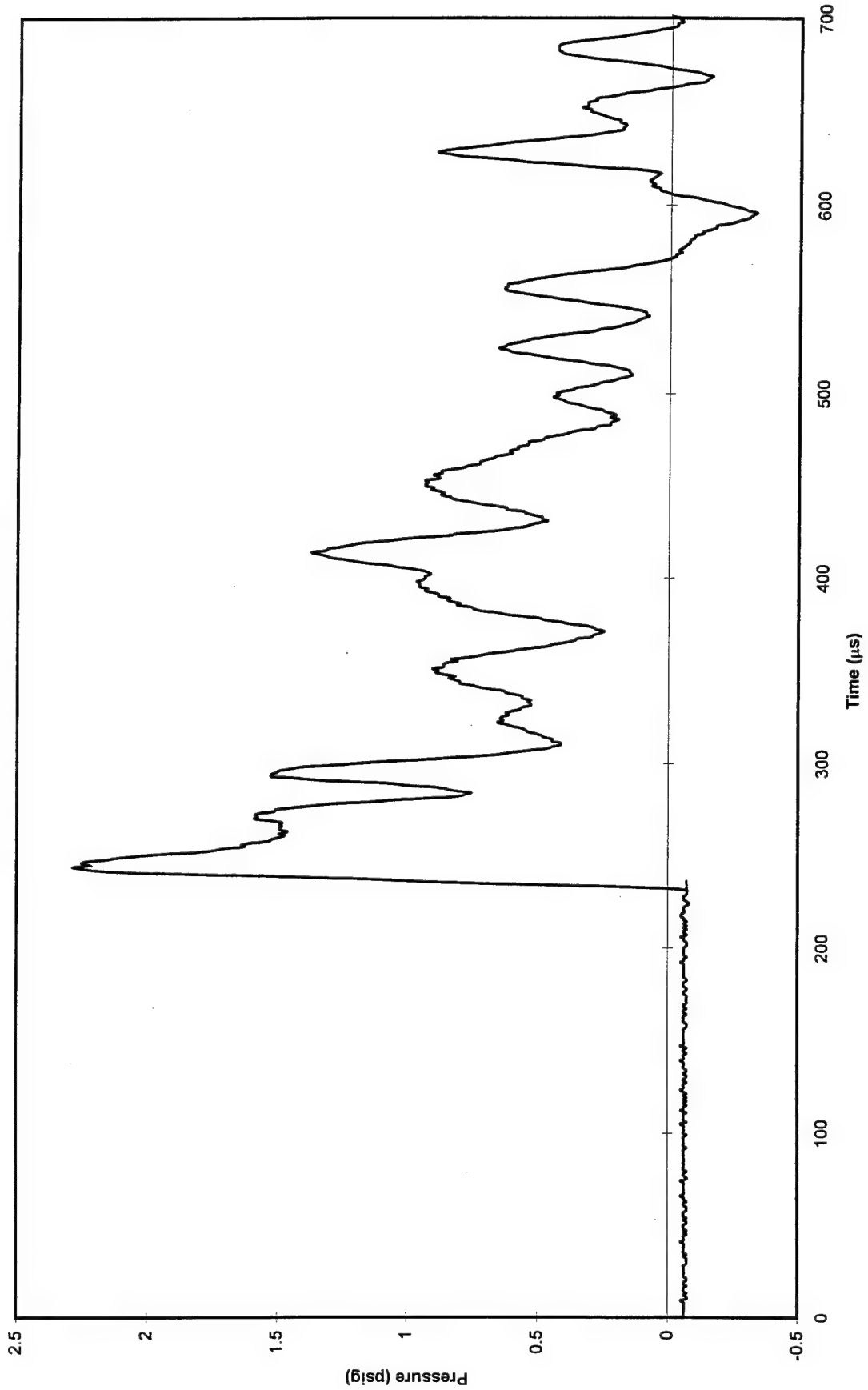
Figure A.7  No Flow Cascade Run - Pressure Data - Kulite #1 - Run 1

No Flow Cascade Shock Passing
Heat Flux Data (H1 - 9/12 - Run 2)
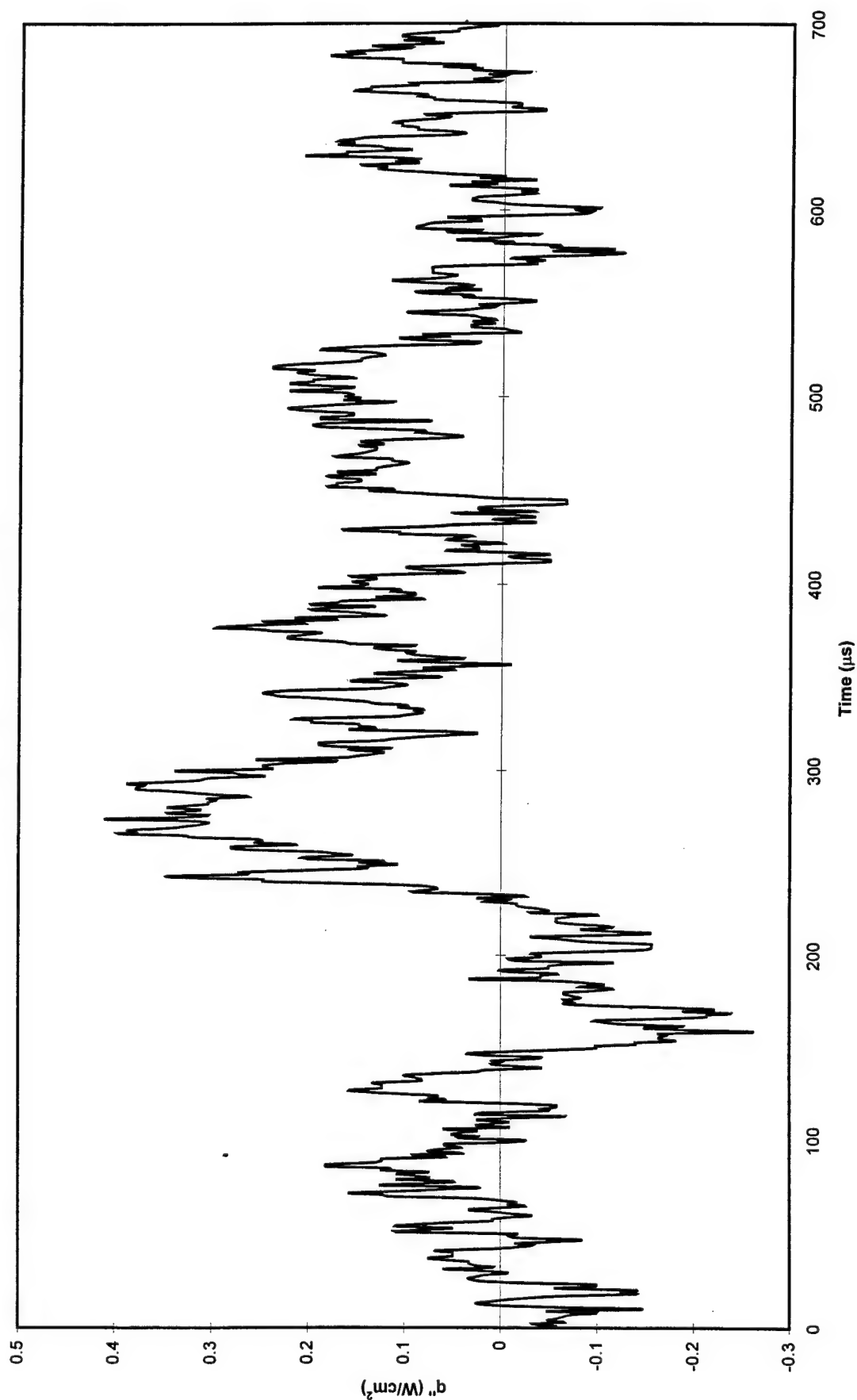
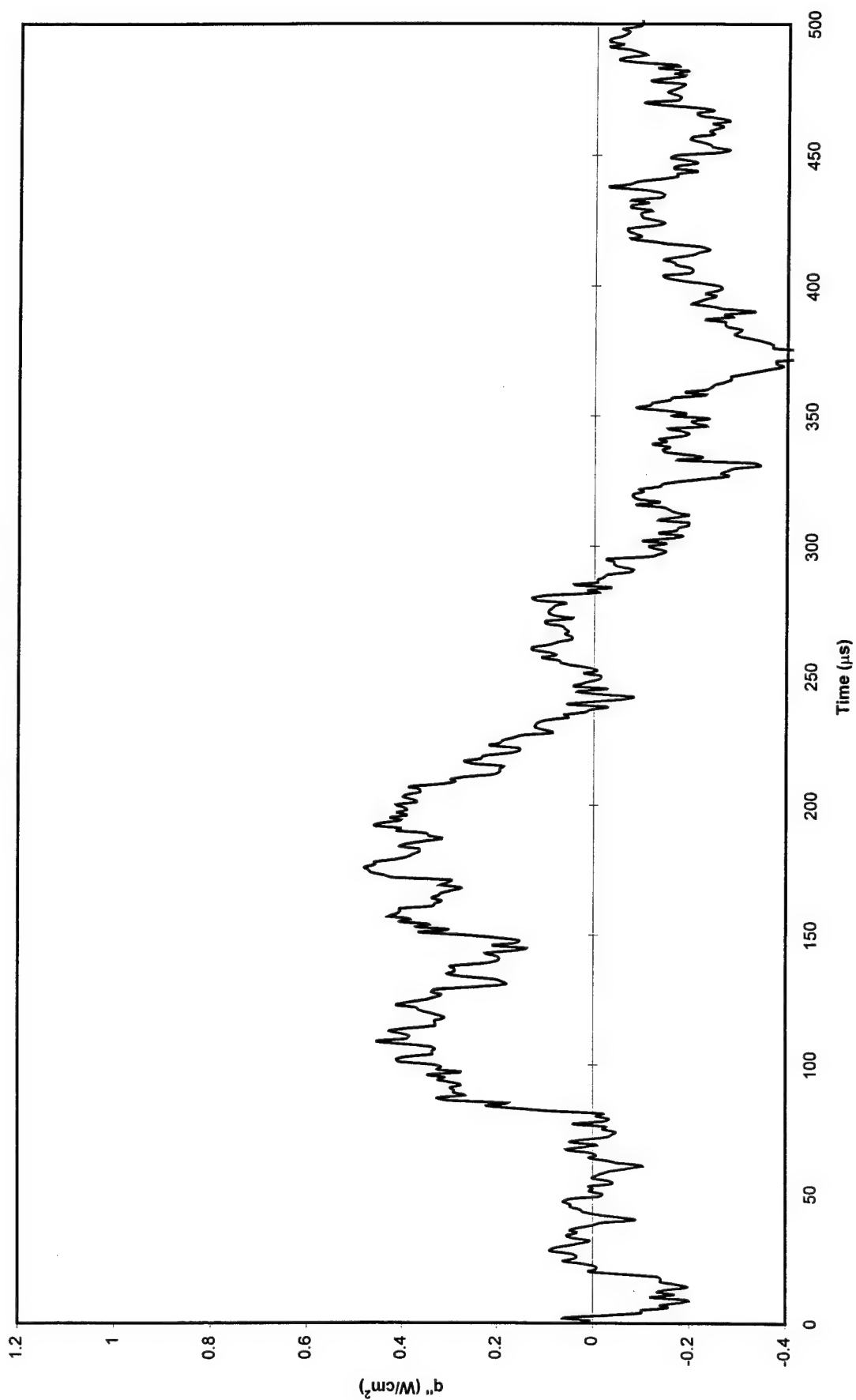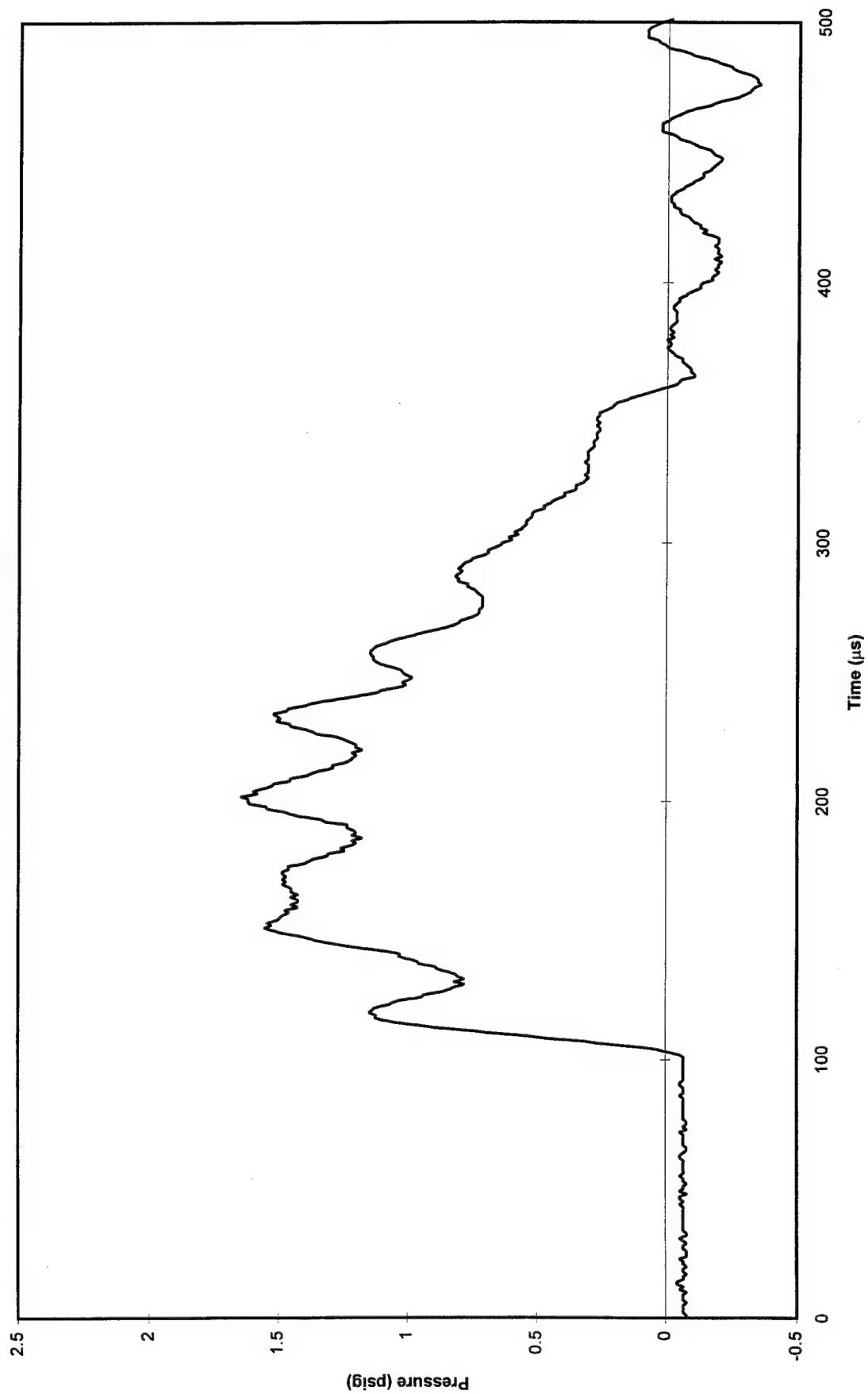Figure A.8 No Flow Cascade Run - Heat Flux Data - HFM-6 #1 (Sputtered) - Run 1

Figure A.9  No Flow Cascade Run - Heat Flux Data - HFM-6 #2 - Run 1

No Flow Cascade Shock Passing
Pressure Data (K3 - 9/12 - Run 2)
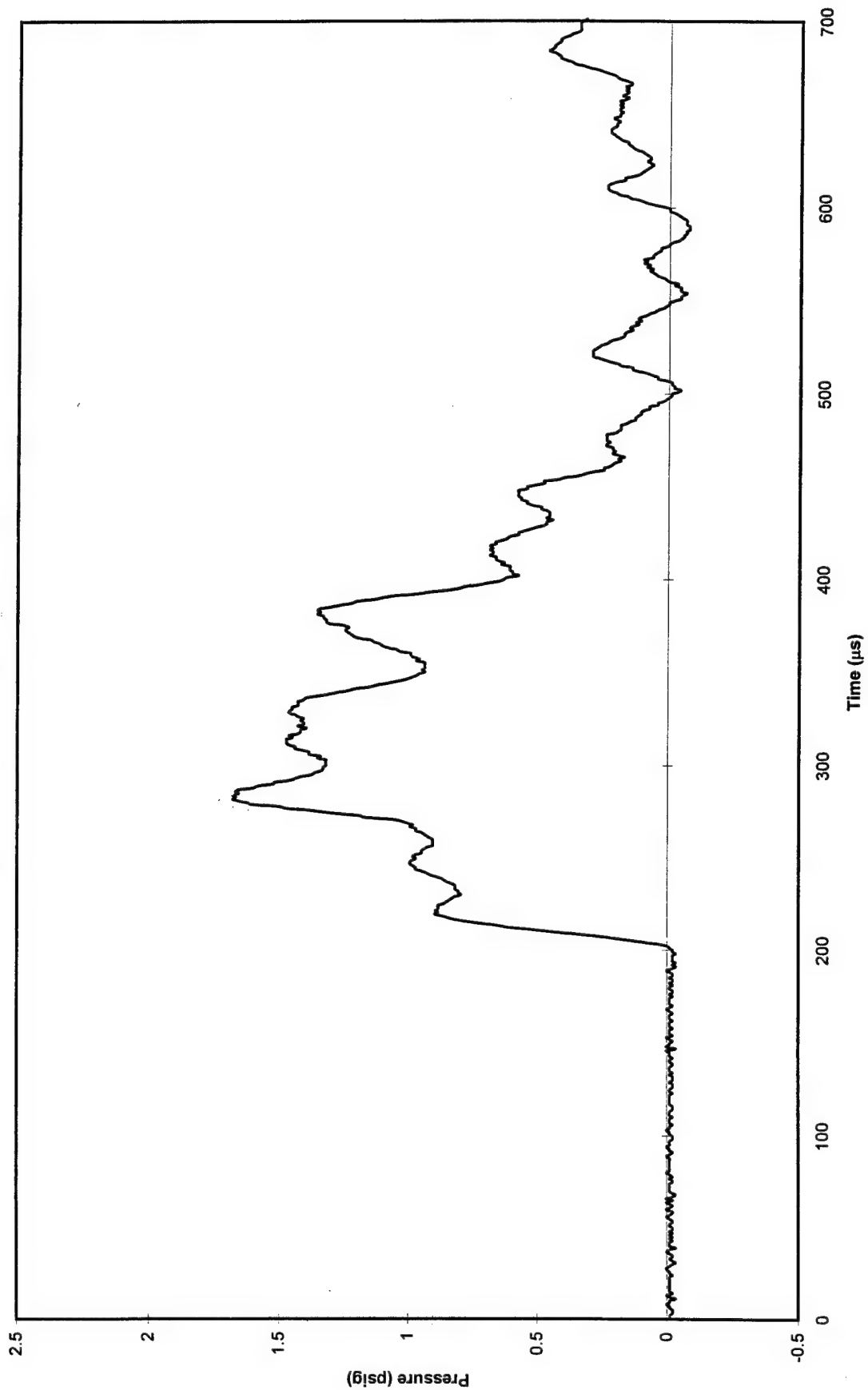
Figure A.10  No Flow Cascade Run - Pressure Data - Kulite #3 - Run 1

**No Flow Cascade Shock Passing
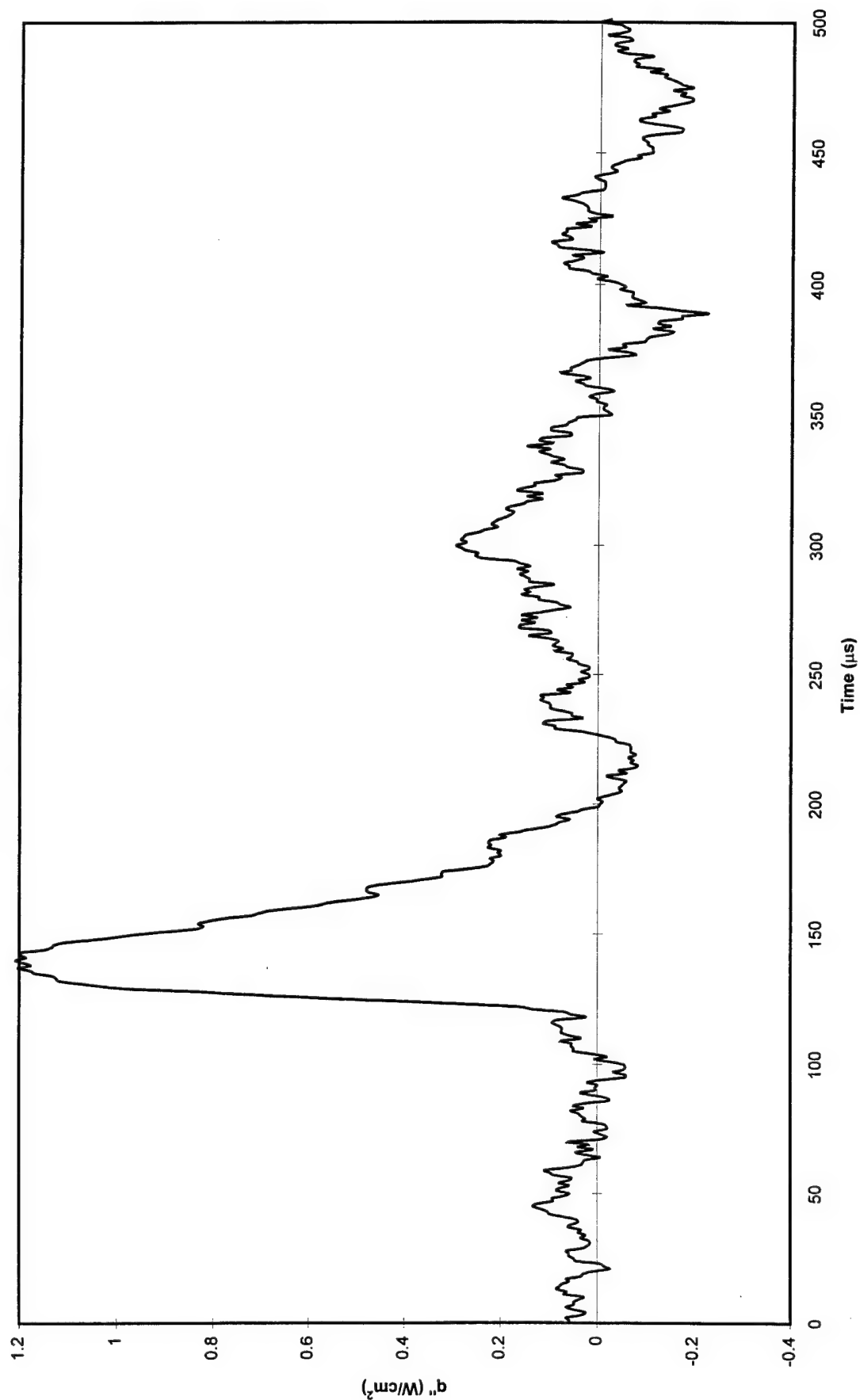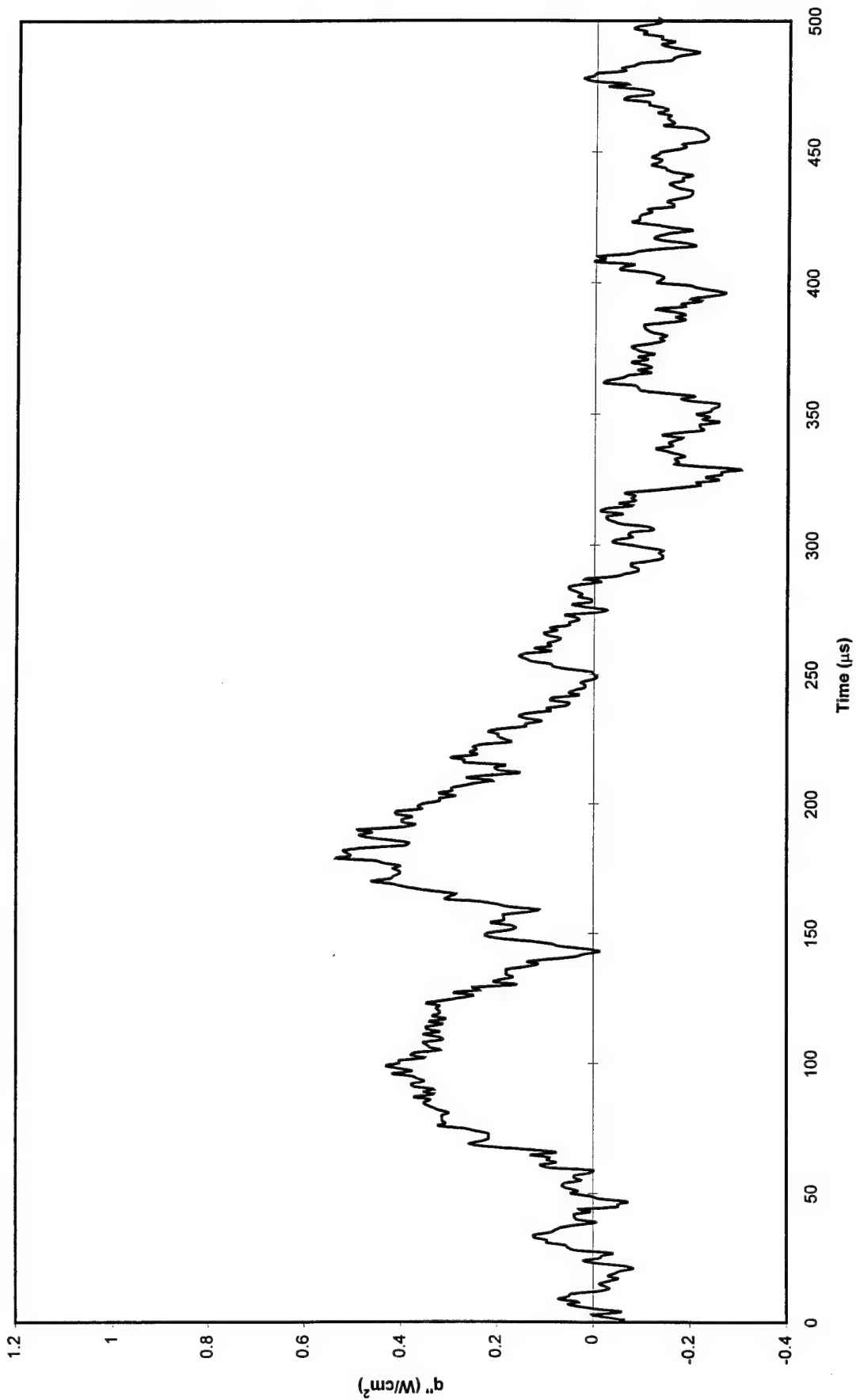Heat Flux Data (H3 - 9/12 - Run 2)**
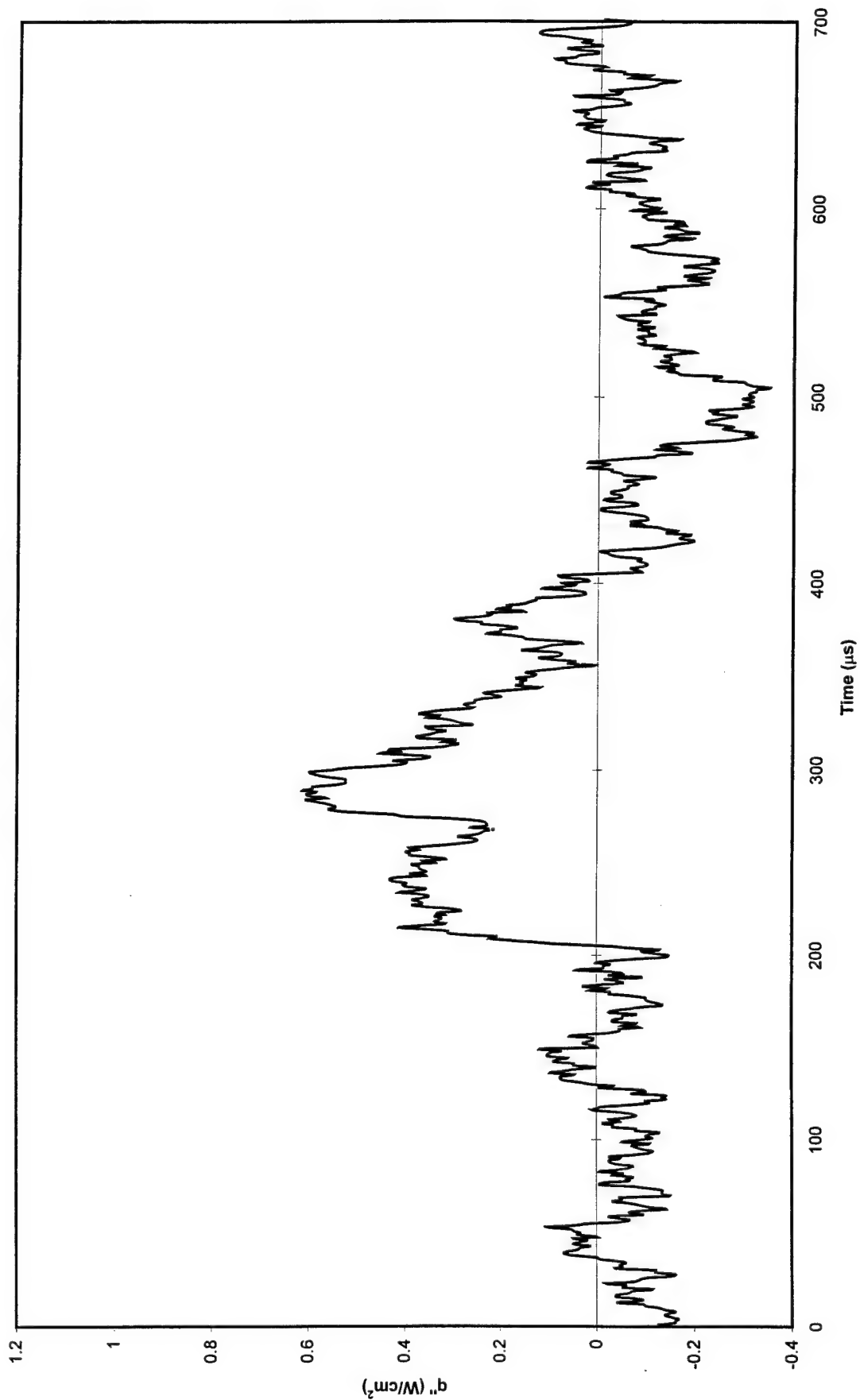


Figure A.11  No Flow Cascade Run - Heat Flux Data HFM-6 #3 - Run 1

No Flow Cascade Shock Passing
Pressure Data (K4 - 9/12 - Run 2)
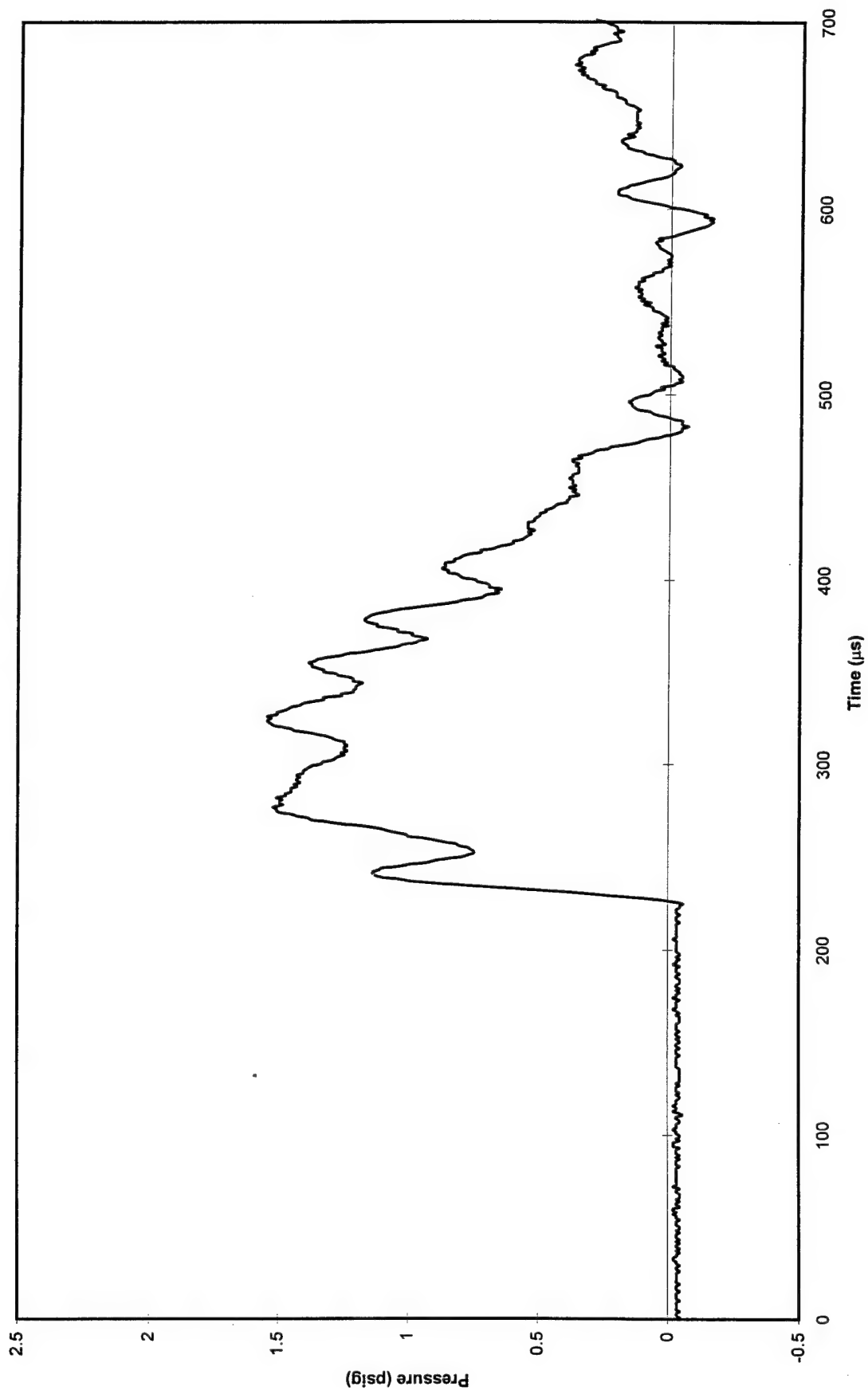
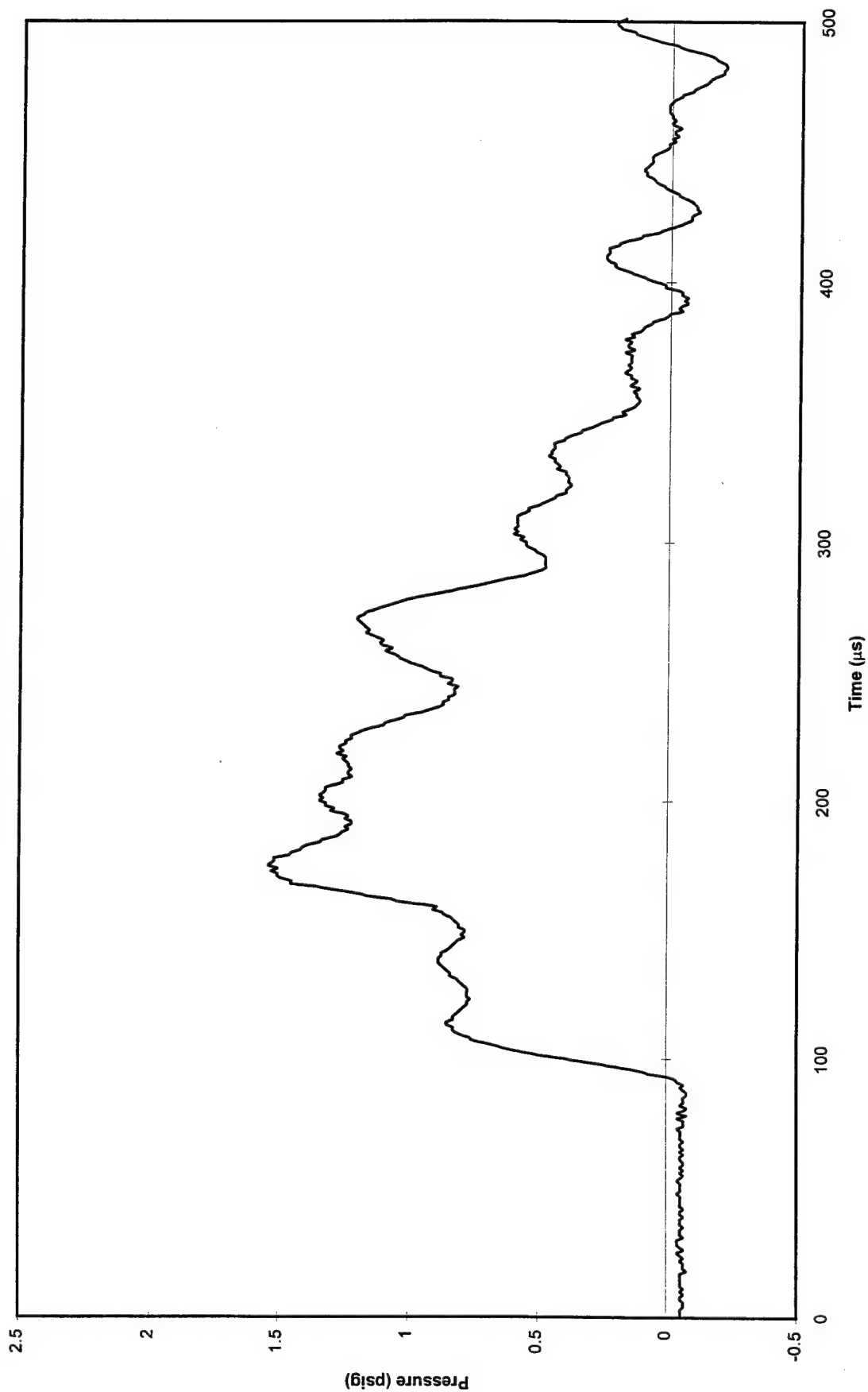Figure A.12  No Flow Cascade Run - Pressure Data Kulite #4 - Run 1

Figure A.13  No Flow Cascade Run - Pressure Data Kulite #1 - Run 2

No Flow Cascade Shock Passing
Heat Flux Data (H1 - 9/12 - Run 3)
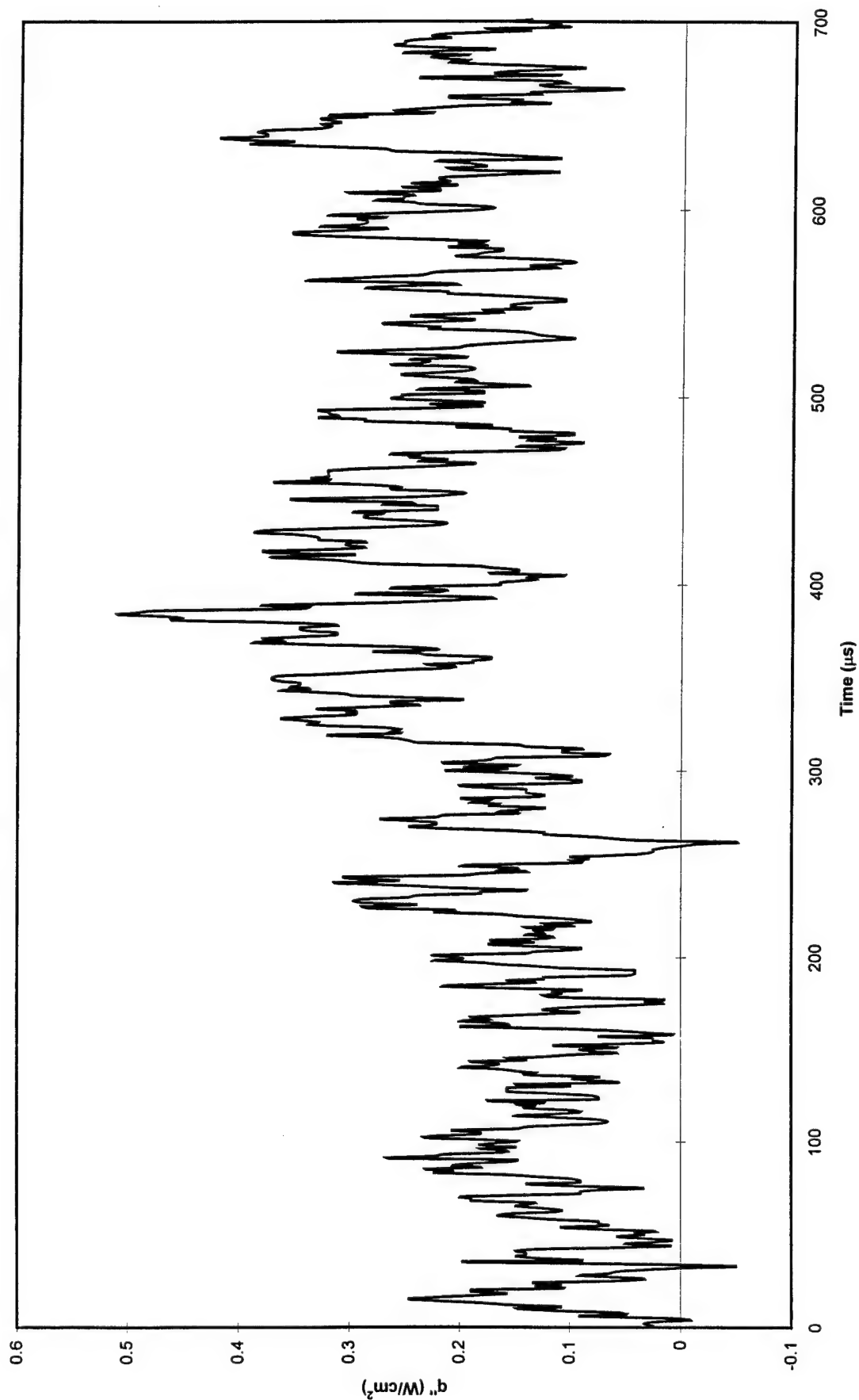
Figure A.14  No Flow Cascade Run - Heat Flux Data HFM-6 #1 (Sputtered) - Run 2

No Flow Cascade Shock Passing
Heat Flux Data (H2 - 9/12 - Run 3)
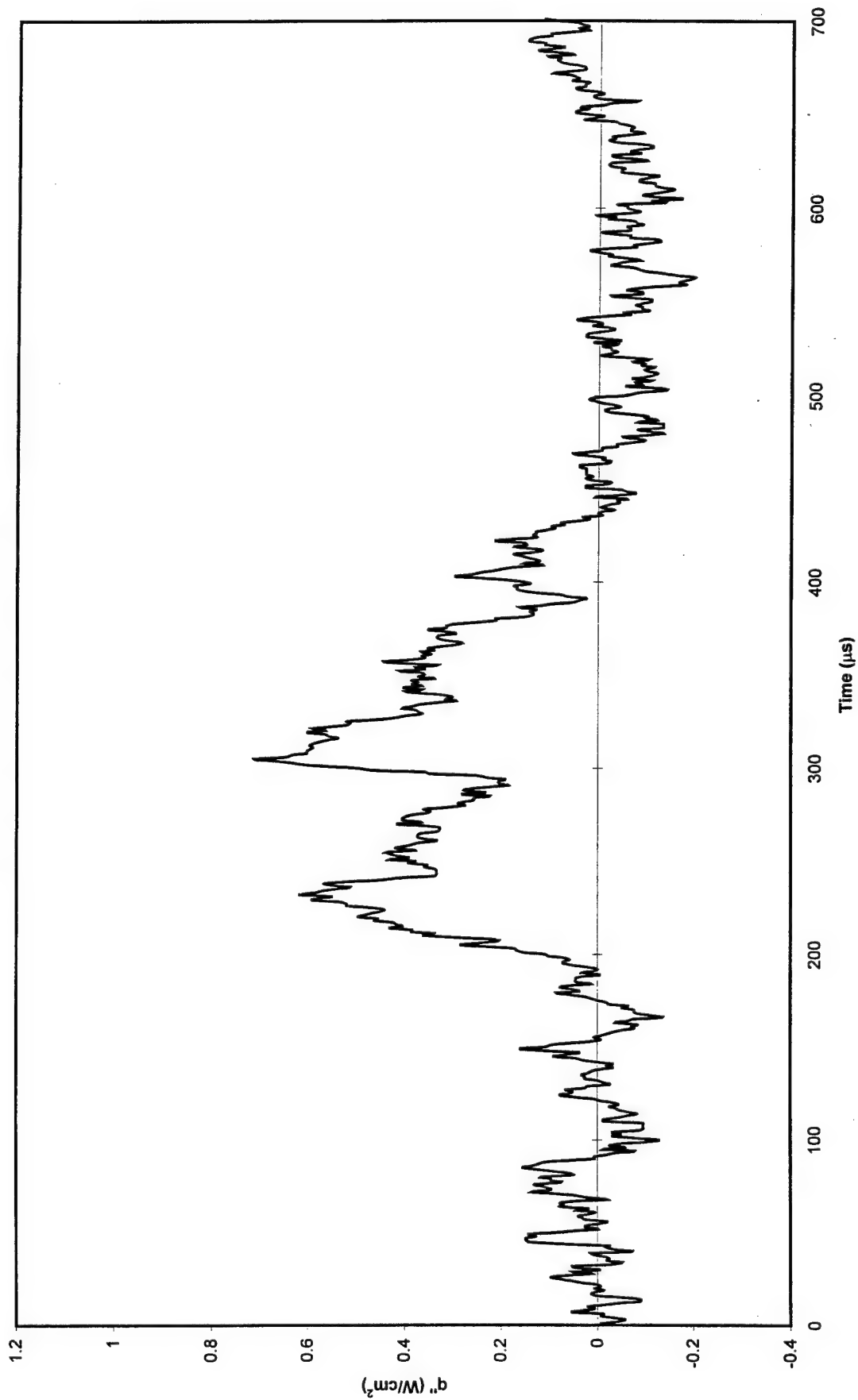
Figure A.15  No Flow Cascade Run - Heat Flux Data - HFM-6 #2 - Run 2

No Flow Cascade Shock Passing
Pressure Data (K3 - 9/12 - Run 3)
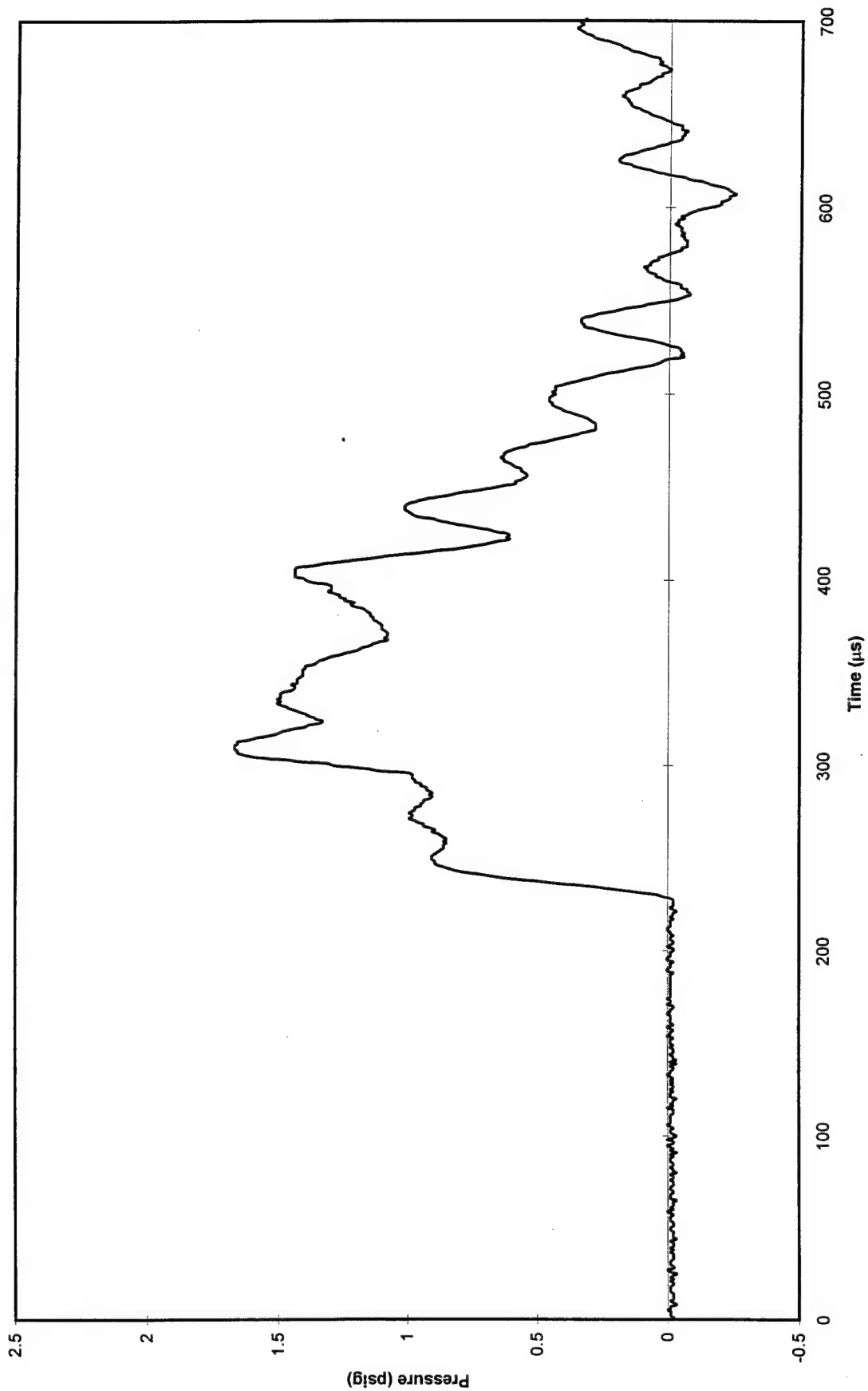
Figure A.16 No Flow Cascade Run - Pressure Data Kulite #3 - Run 2

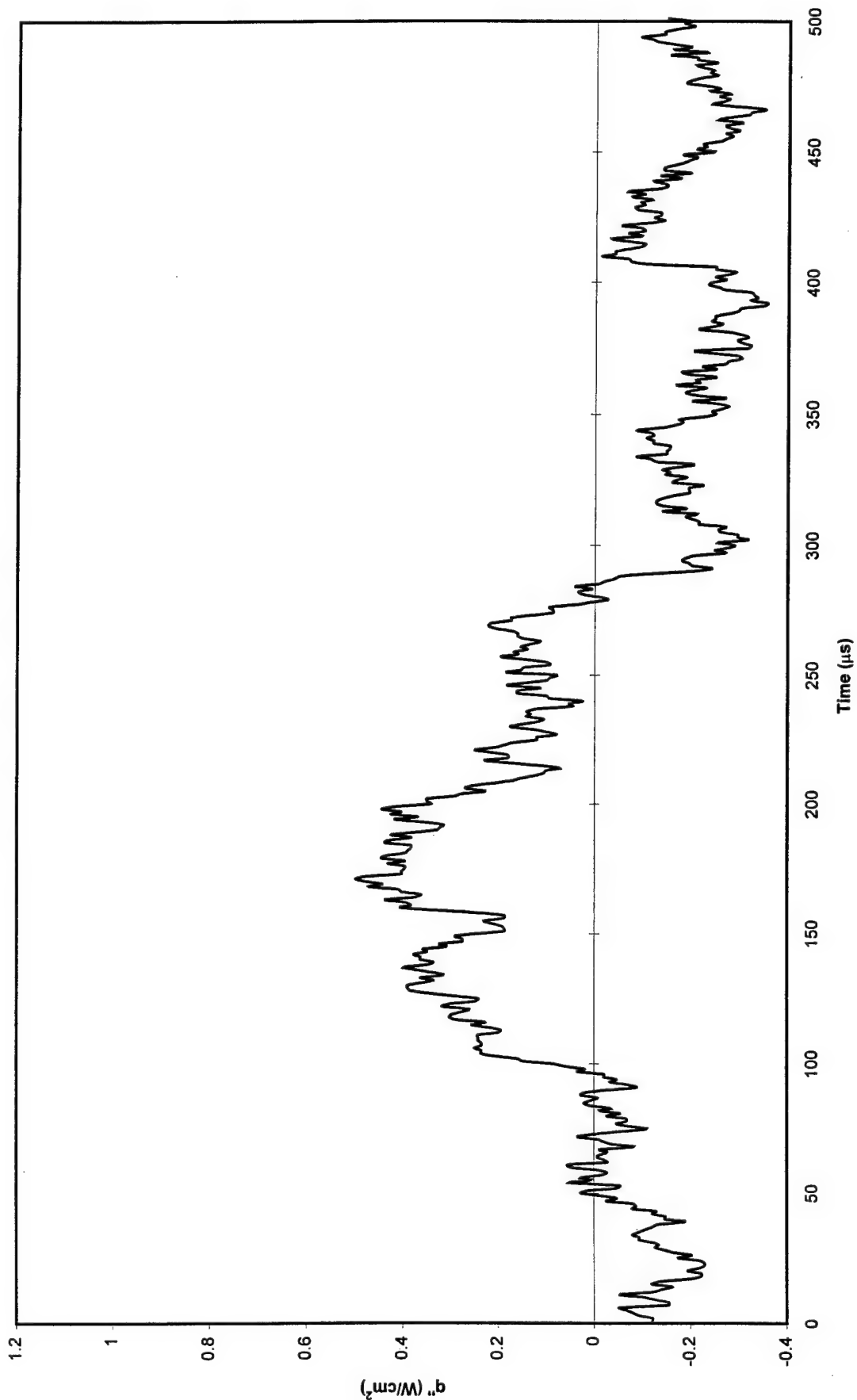No Flow Cascade Shock Passing
Heat Flux Data (H3 - 9/12 - Run 3)
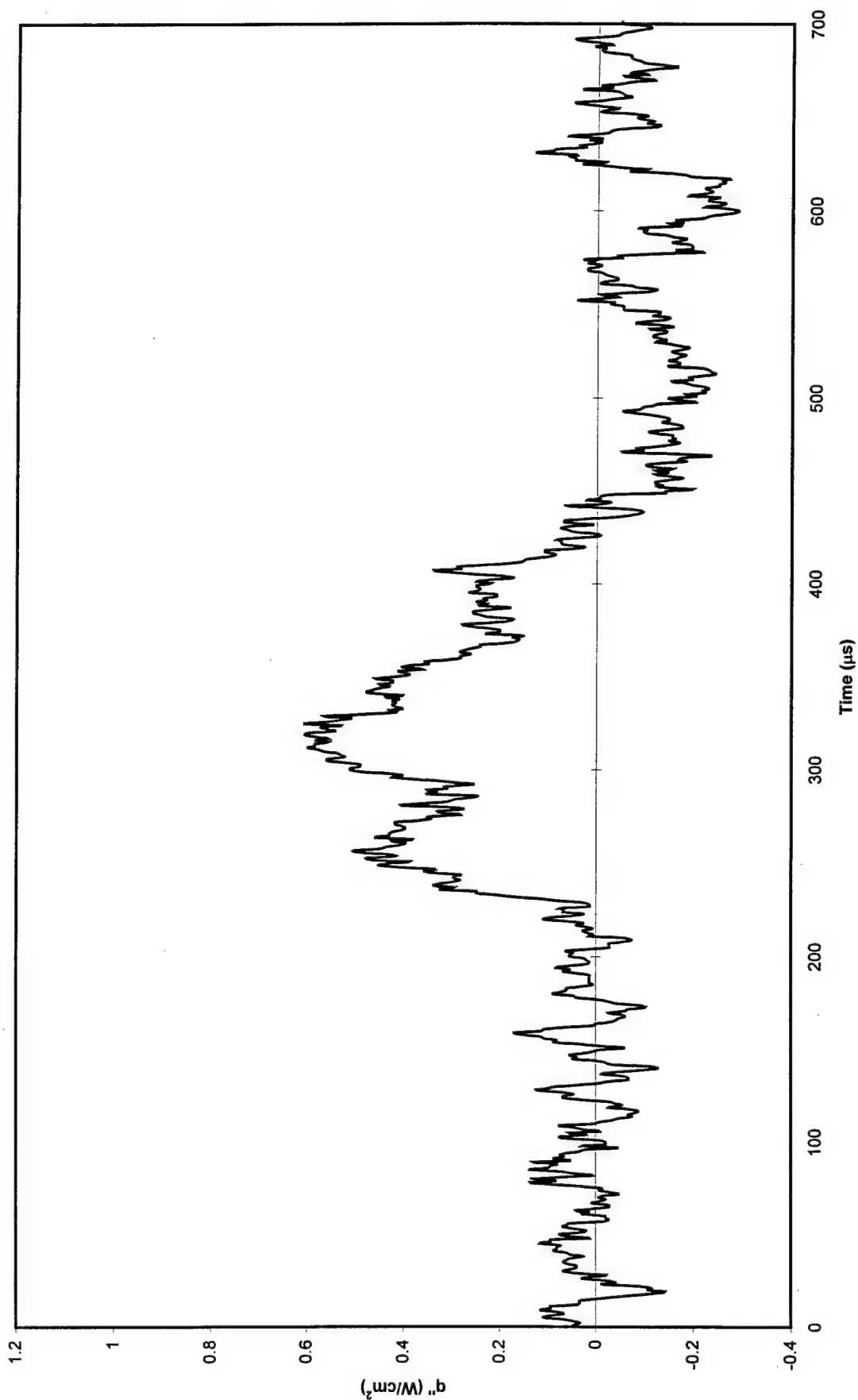
Figure A.17  No Flow Cascade Run - Heat Flux Data HFM-6 #3 - Run 2

No Flow Cascade Shock Passing
Pressure Data (K4 - 9/12 - Run 3)
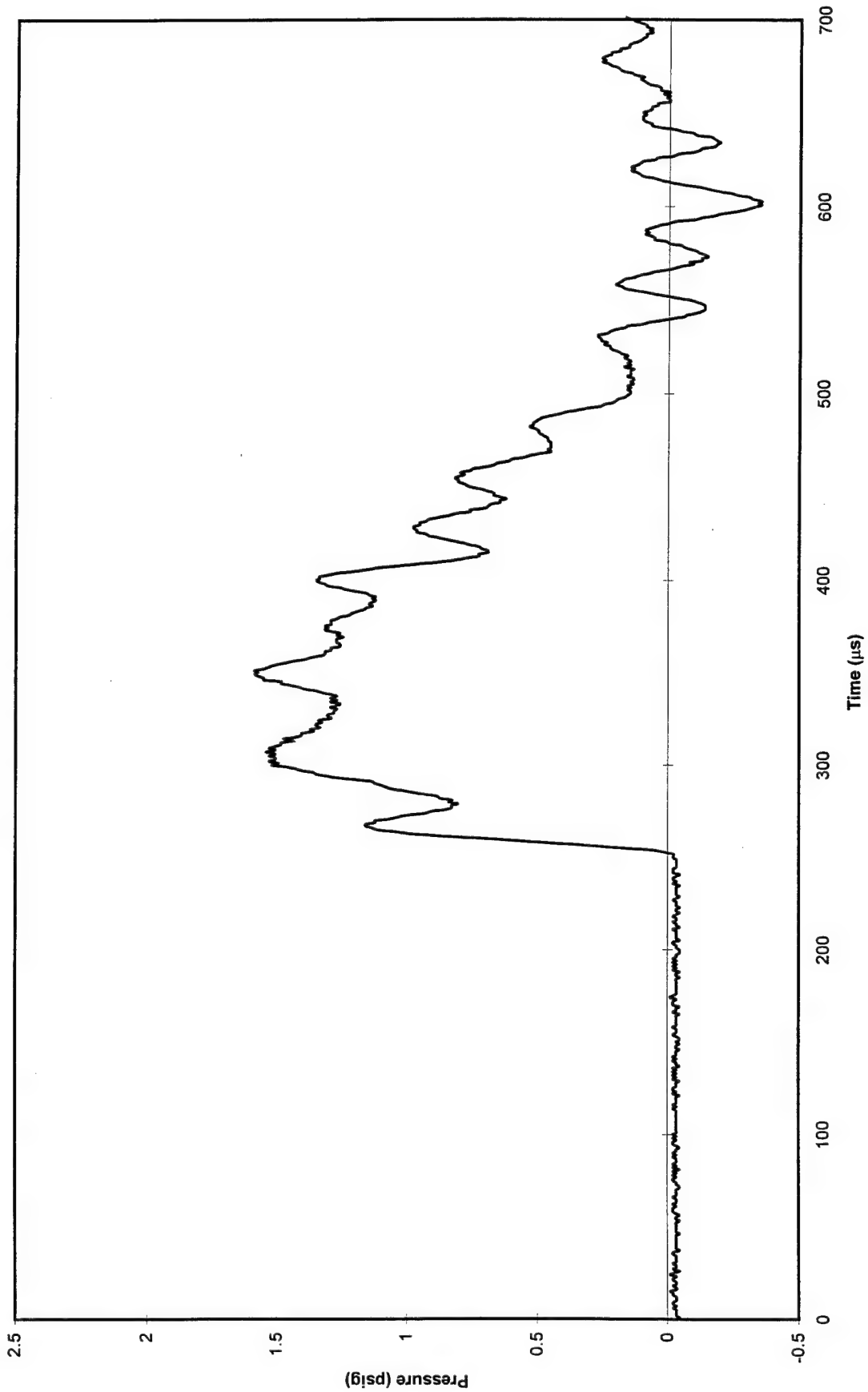
Figure A.18  No Flow Cascade Run - Pressure Data Kulite #4 - Run 2
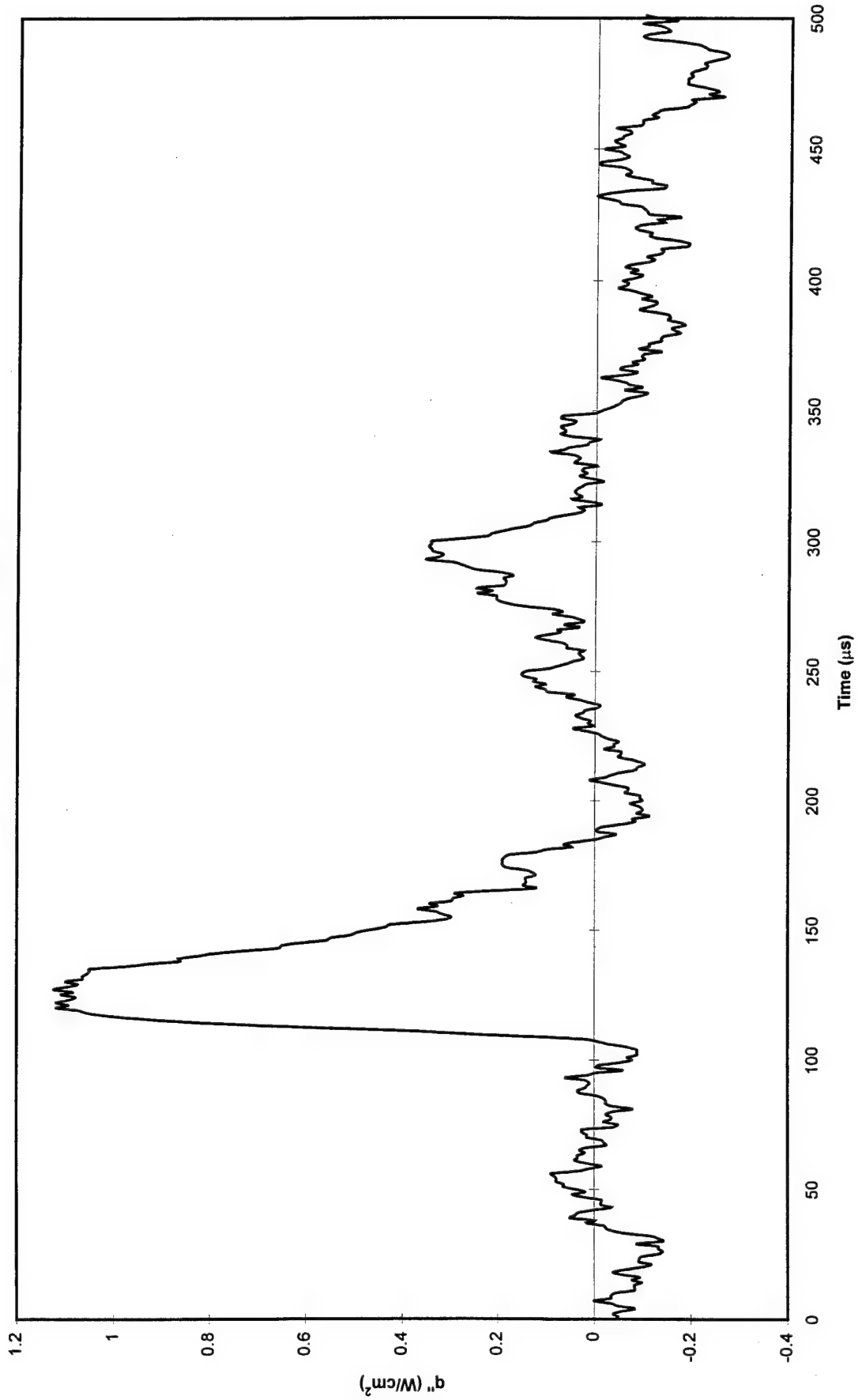
Figure A.19 No Flow Cascade Run - Heat Flux Data HFM-6 #1 (Insert) - Run 3

Figure A.20  No Flow Cascade Run - Heat Flux Data HFM-6 #2 - Run 3

Figure A.21  No Flow Cascade Run - Pressure Data Kulite #3 - Run 3

Cascade Shock Passing - No Flow
Heat Flux Data (H3 - 10/2 - Run 1)

Figure A.22  No Flow Cascade Run - Heat Flux Data HFM-6 #3 - Run 3

133

134



Figure A.23  No Flow Cascade Run - Pressure Data Kulite #4 - Run 3

Figure A.24  No Flow Cascade Run - Heat Flux Data HFM-6 #1 (Insert) - Run 4

Cascade Shock Passing - No Flow
Heat Flux Data (H2 - 10/2 - Run 2)

Figure A.25  No Flow Cascade Run - Heat Flux Data HFM-6 #2 - Run 4

Cascade Shock Passing - No Flow
Pressure Data (K3 - 10/2 - Run 2)

Figure A.26  No Flow Cascade Run - Pressure Data Kulite #3 - Run 4

Cascade Shock Passing - No Flow
Heat Flux Data (H3 - 10/2 - Run 2)

Figure A.27  No Flow Cascade Run - Heat Flux Data HFM-6 #3 - Run 4

138
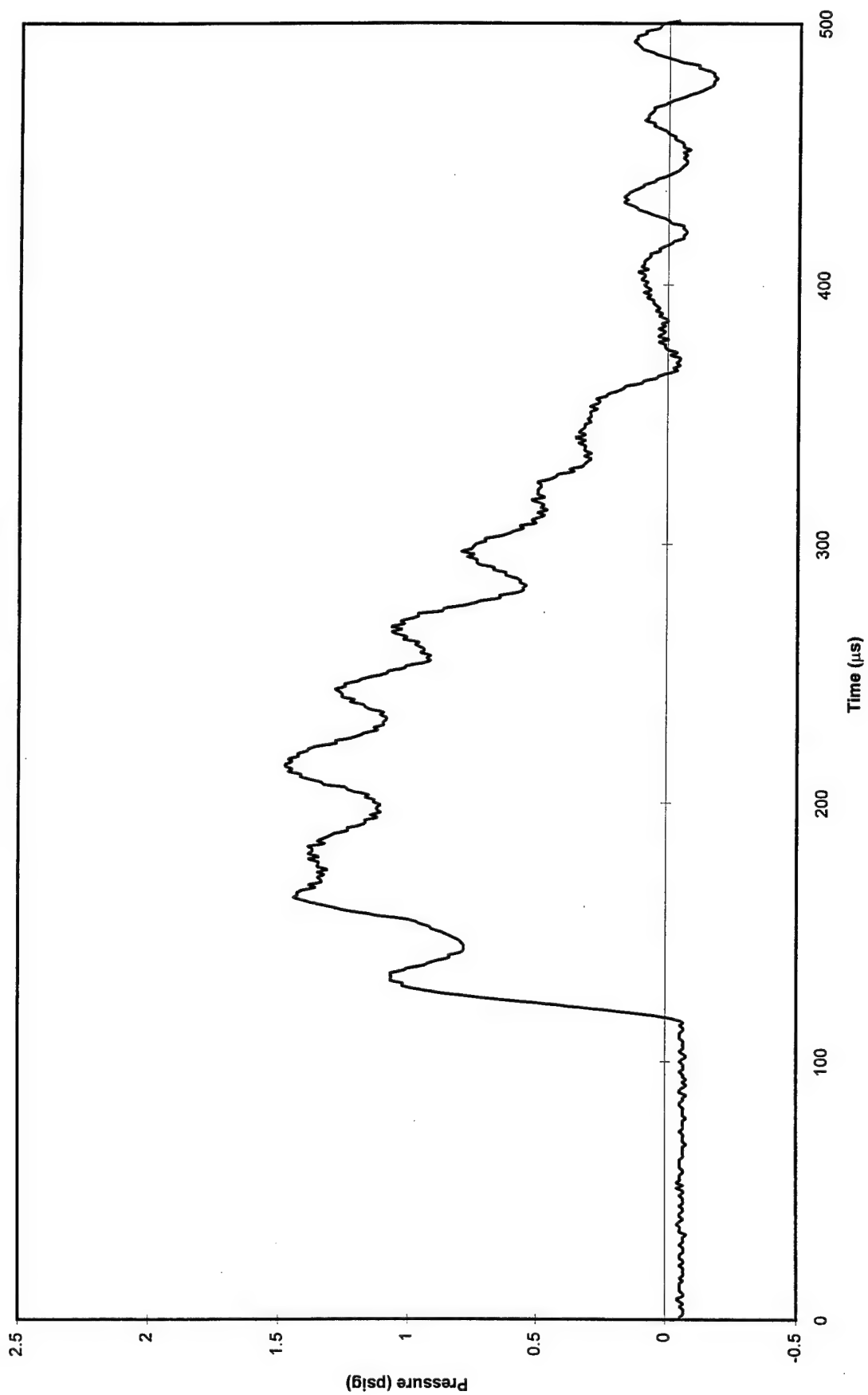
Figure A.28  No Flow Cascade Run - Pressure Data Kulite #4 - Run 4

139

# 3. Unheated Cascade Runs

# 4. Heated Cascade Runs

# 5. Comparison of Heated and Unheated Runs

# Appendix B

## Heat Flux Microsensor Response Plots

This appendix contains the results for the theoretical semi-infinite model applied to several bench tests runs. The results are presented for both tangentially passing and normally impacting shock bench tests.
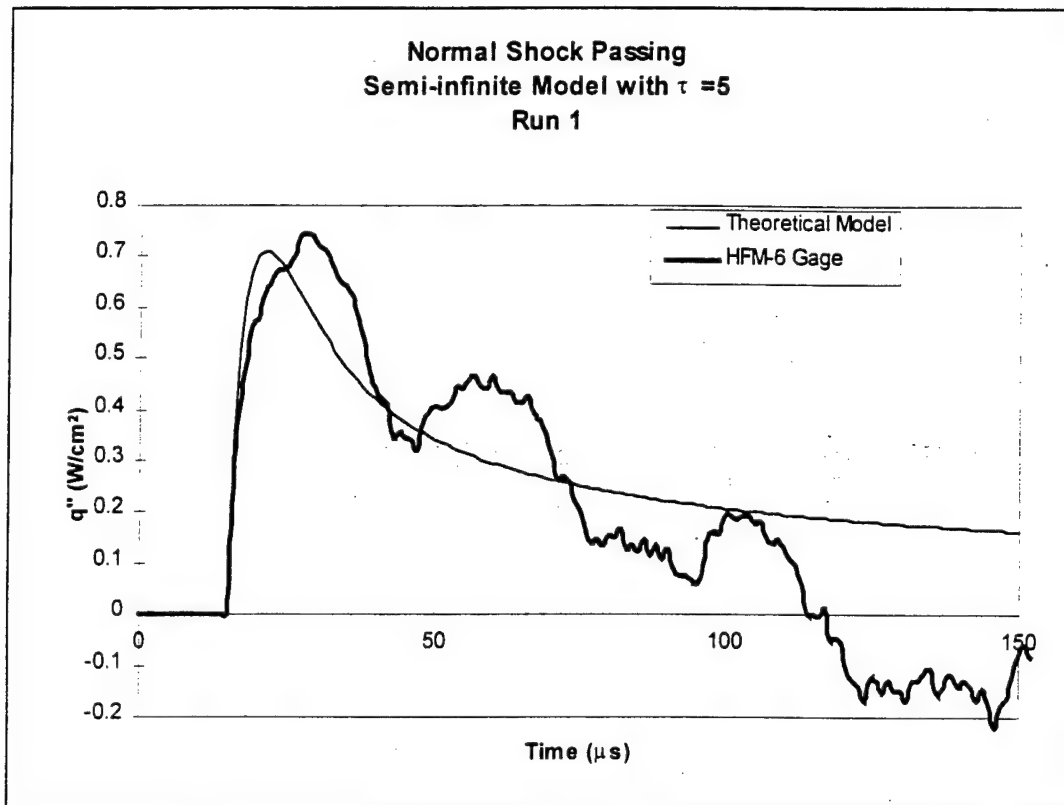
Figure B.1  Theoretical Response Model for Normally Impacting Shock Bench Test - Run 1
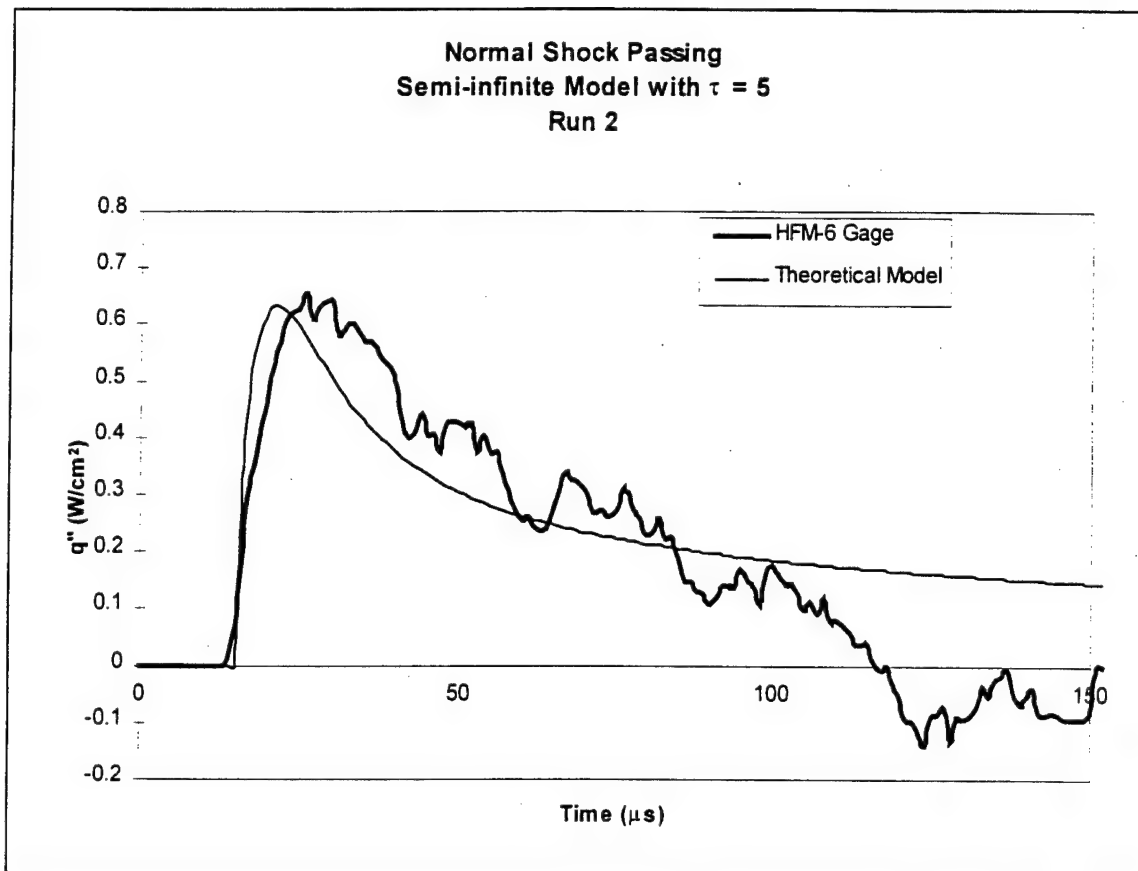
Figure B.2  Theoretical Response Model for Normally Impacting Shock Bench Test -
Run 2
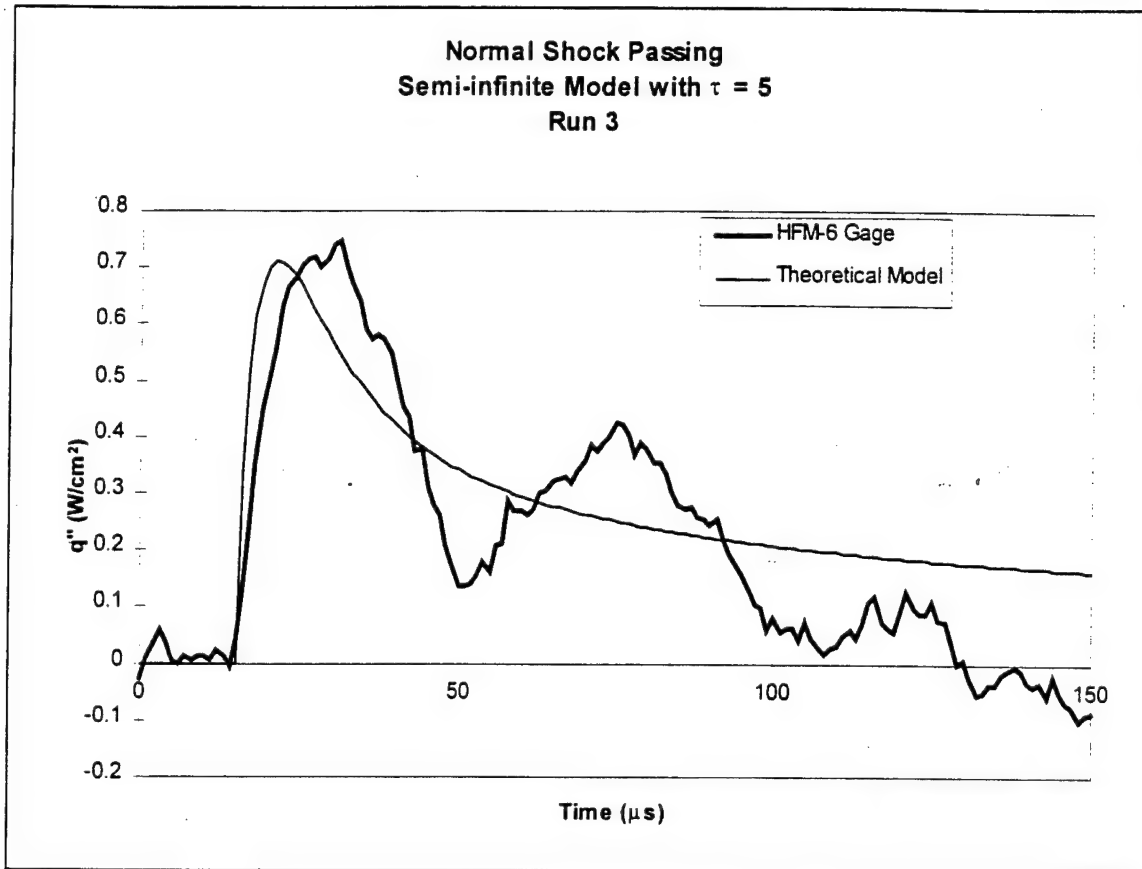
Figure B.3  Theoretical Response Model for Normally Impacting Shock Bench Test - Run 3
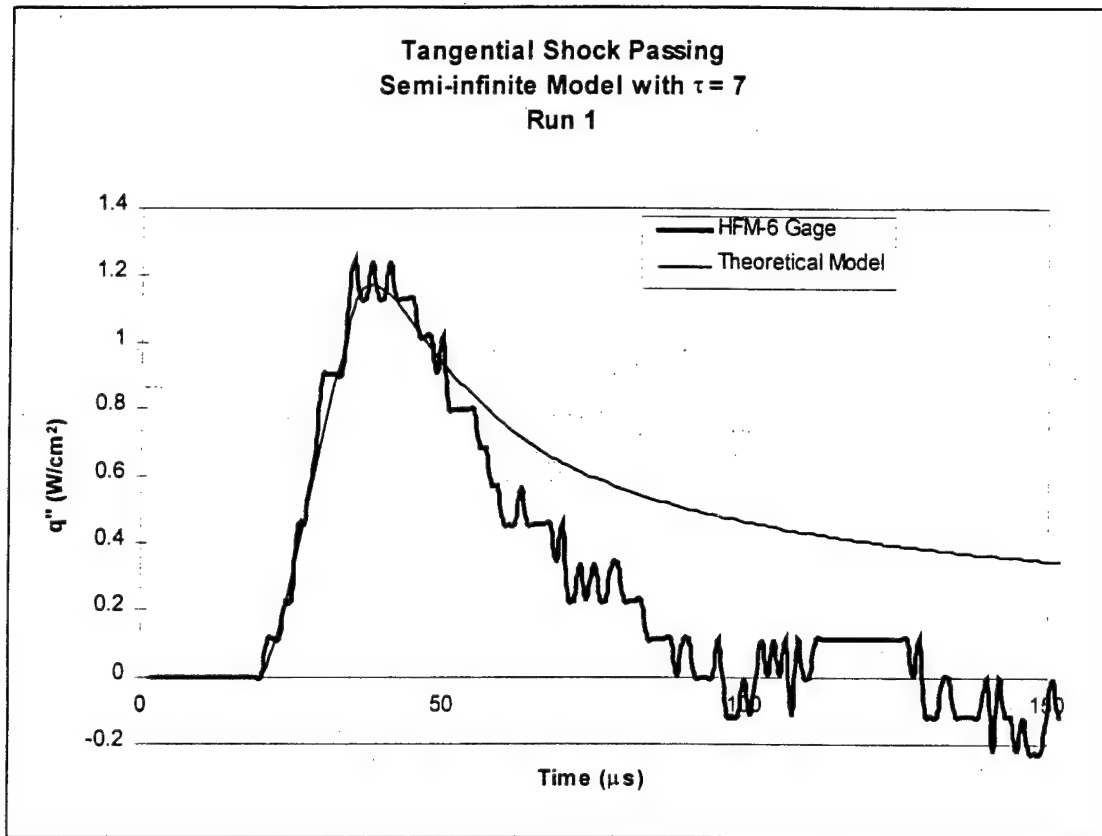
Figure B.4  Theoretical Response Model for Tangentially Passing Shock Bench Test -
Run 1
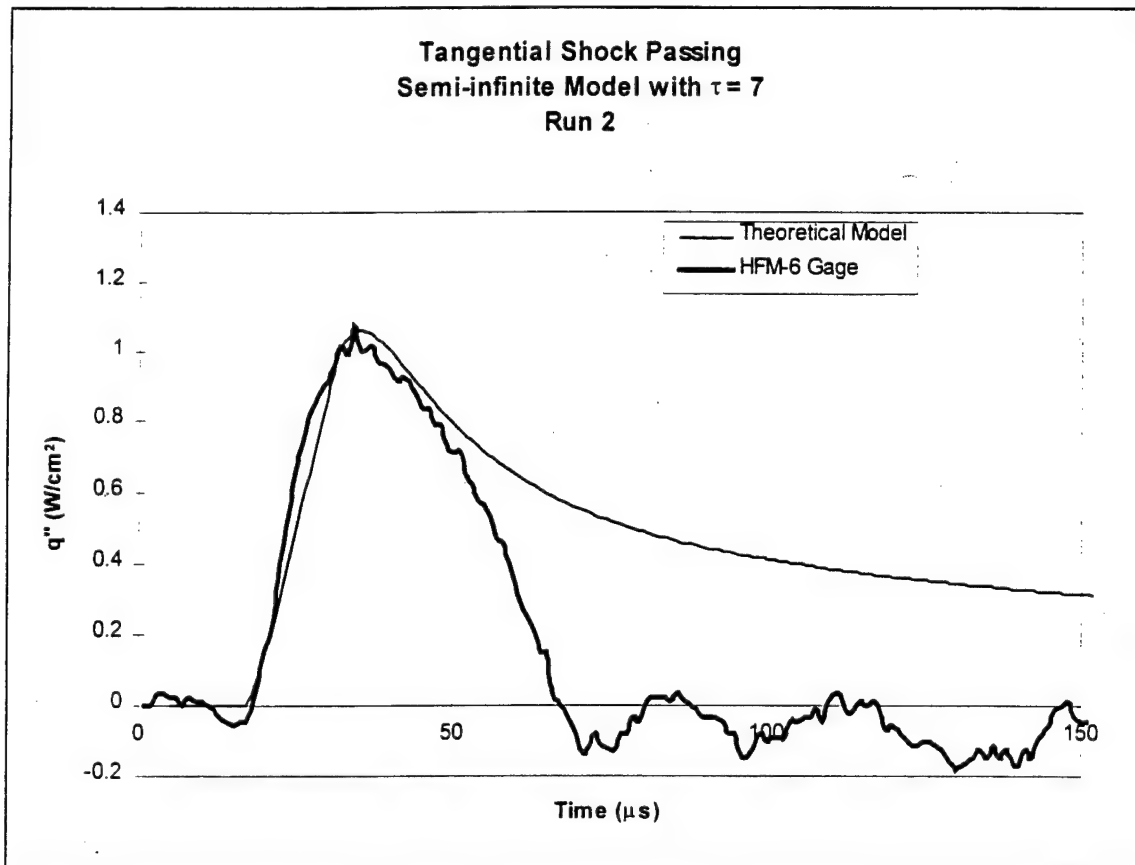
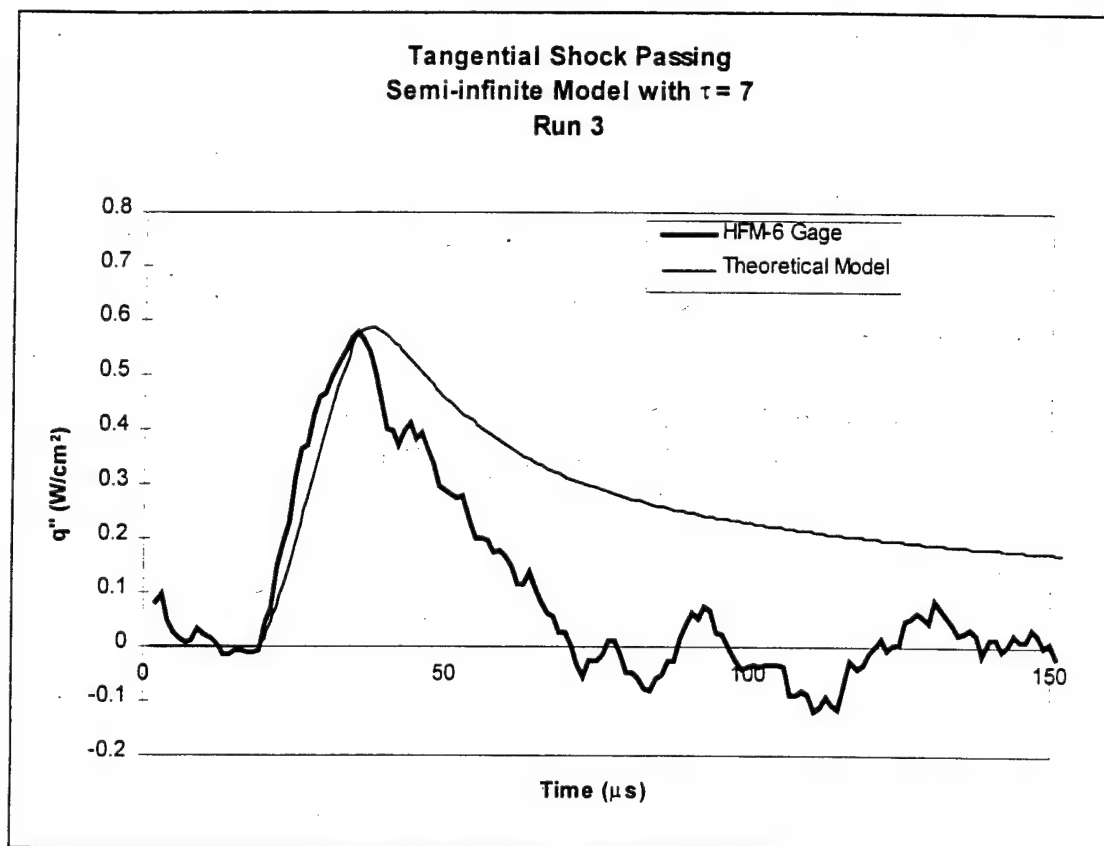Figure B.5  Theoretical Response Model for Tangentially Passing Shock Bench Test - Run 2

Figure B.6  Theoretical Response Model for Tangentially Passing Shock Bench Test - Run 3

# Appendix C

# Shock Progression Analysis

Before analyzing the pressure and heat flux traces resulting from a passing shock, the progression of the shock and its reflections through the blade passage need to be understood. Due to the geometry of the blade passage and since the passage essentially captures the shock between the blading, the shock will reflect between the blades several times before losing strength significant enough to effect the pressure and temperature in the passage and the boundary layer on the blade surfaces. This appendix presents a detailed discussion of the progression of shock waves in the turbine cascade and correlates the shocks to peaks in heat flux measured experimentally (plots shown in Chapter 5). The shock progression was performed using shadowgraphs taken at specific time delays from an initial trigger point from a gage upstream of the instrumented passage. This initial analysis suggested that the pressure surface would see the greatest overall effect from the shock passing event, therefore the majority of the gages were placed on the pressure surface for this work. Following is a detailed discussion of the shock progression through the cascade correlating each shock or reflection to heat flux peaks at each gage location. Also included is a segment of a presentation of the shock progression analysis which has gage locations different from those used in this work, but is useful in demonstrating the progression of shock waves through the cascade and their effects on heat transfer.

Gage location # 1 (suction surface) is affected by two events of shock impact in the time period discussed above (Figure 5.10 and Figure 5.17). The first impact is from a tangentially passing shock propagating through the test section above the blade row (Figure C.1). This shock is the strongest seen by the gages in the blade passage, as it is the original shock introduced into the test section along with reflections from previous blade passages. After impacting the suction surface, this shock and the reflections which "bubble" up behind it continue to propagate through the cascade to the next blade passage, as seen in Figure C.1. The second peak impacting gage location #1 is also a tangentially passing shock, but this shock is a reflection within the passage and is considerably weaker (Figure C.2).

Gage location #2 (pressure surface) is affected by 3 shock events, the first being a tangentially passing shock (Figure 5.11 and Figure 5.18). This shock is the same unreflected shock that will impact gage location #1 initially, except the shock is wrapped around the blade and one edge propagates along the pressure surface of the blade passage (Figure C.3). The second shock event is a normally impacting shock, which is a
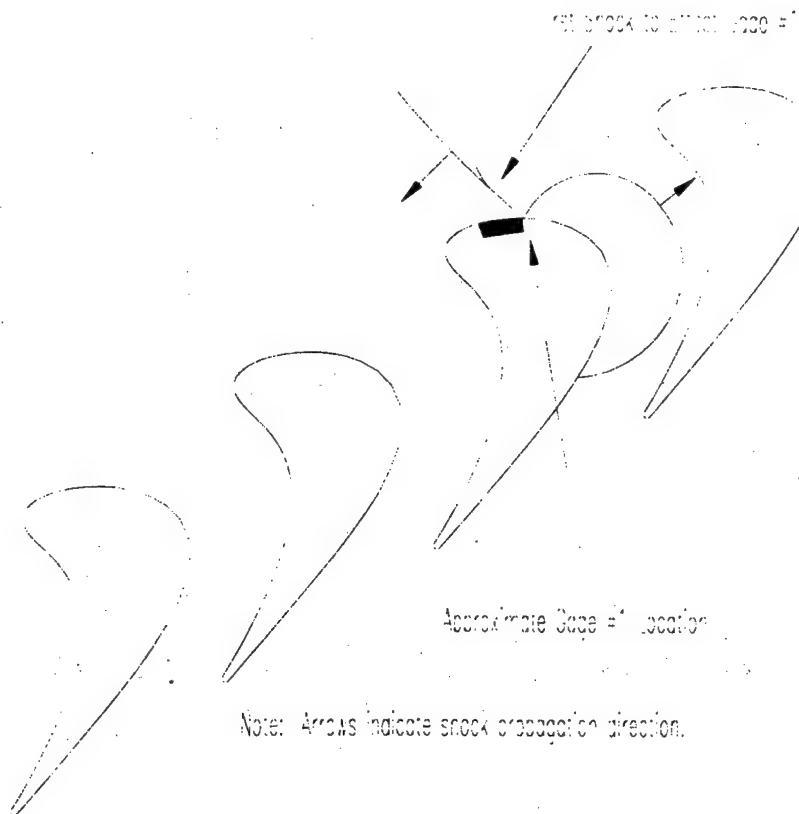
1st shock to either edge #1

Approximate Gage #1 Location

Note: Arrows indicate shock propagation direction.

Figure C.1  Illustration of First Shock Affecting HFM-6 Gage #1

Figure C.2  Illustration of Second Shock Affecting HFM-6 Gage #1
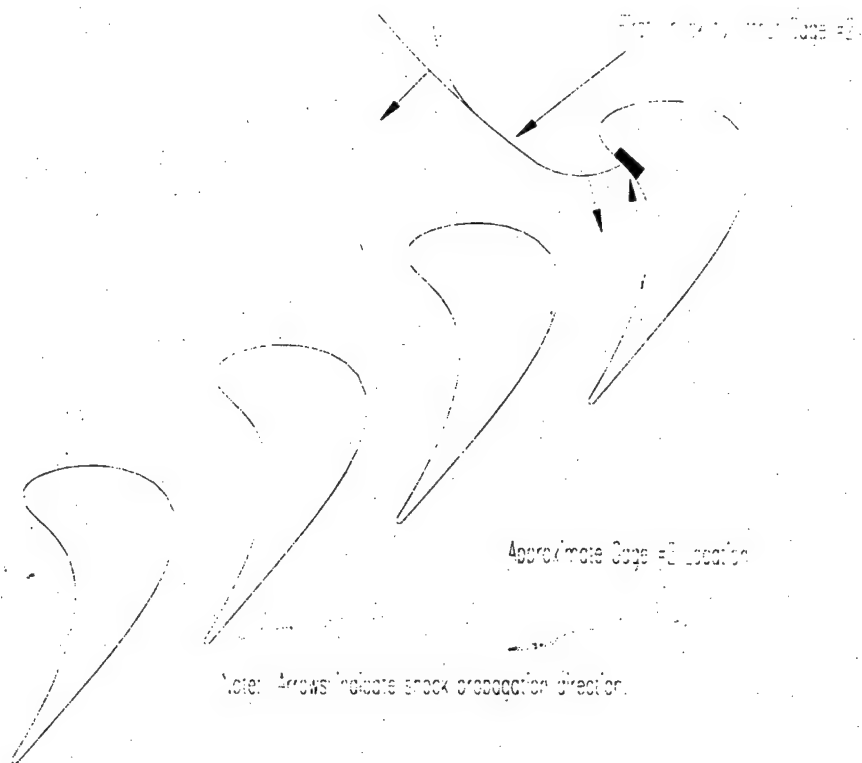
Figure C.3  Illustration of First Shock Affecting HFM-6 Gage #2

reflection of the original shock, propagating across the blade passage from the suction surface towards the pressure surface (Figure C.4). The heat flux between these two peaks can be seen to rise slightly, suggesting that the first shock impact (tangentially passing shock) has some continuing effect on the boundary layer on the pressure surface. This effect was not present on the suction surface gage. Also, it can be seen that the heat flux rise time for the first shock event (tangentially passing) is much slower than the second (normally impacting), which agrees with the earlier analysis of rise time (Chapter 6). The third shock event is a normally impacting reflection of the previous shock (also a reflection) again propagating across the blade passage (Figure C.5) and is much weaker. The continuing increase in heat flux seen between the first two peaks is not present between the second and third peaks, suggesting that the boundary layer is not significantly effected by normally impacting shocks. This is probably due to the fact that tangentially passing shocks are continually in contact with the blade surface and are in contact with, and passing through, the boundary layer for a longer period of time.

Due to the close proximity of their locations, gages #2 and #3 see the same series of shock reflections, with a small delay in time (Figure 5.13 and Figure 5.20). Gage location #2 is affected by the first shock before gage #3 as it is upstream of gage #3 on the pressure surface. However, gage #3 is affected by the reflected shock waves before gage #2 (second and third peaks). This can be seen in Figure C.4 and Figure C.5. The reflected shock waves move across the blade passage propagating in a direction slightly opposing the inlet flow and will impact gage #3 before gage #2.

The progression of shocks through the blade passage is similar between unheated and heated runs with a small time delay due to different shock speeds. The speed of the shock waves in the heated runs is slightly higher due to the fact that the shocks are propagating through a higher temperature flow. The heat flux traces for the heated flow can be seen to demonstrate very similar behavior in terms of peaks as the unheated flow cases. The shock progression analysis presented here agrees with numerical results reported by Saxer and Felici (1996) and with experimental results reported by Johnson et al. (1990) using Schlieren photographs in a stationary, linear cascade.
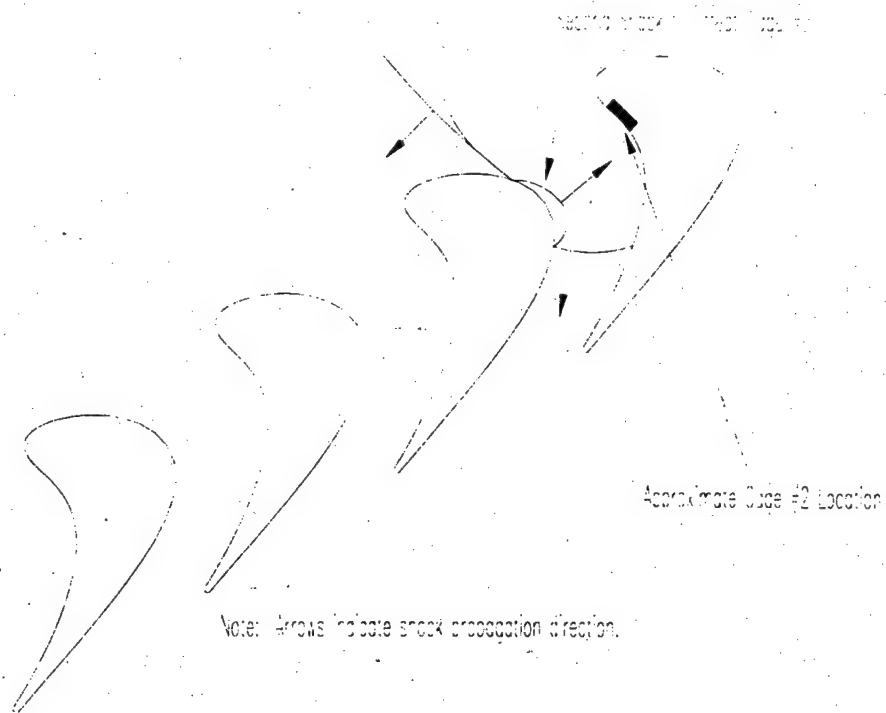
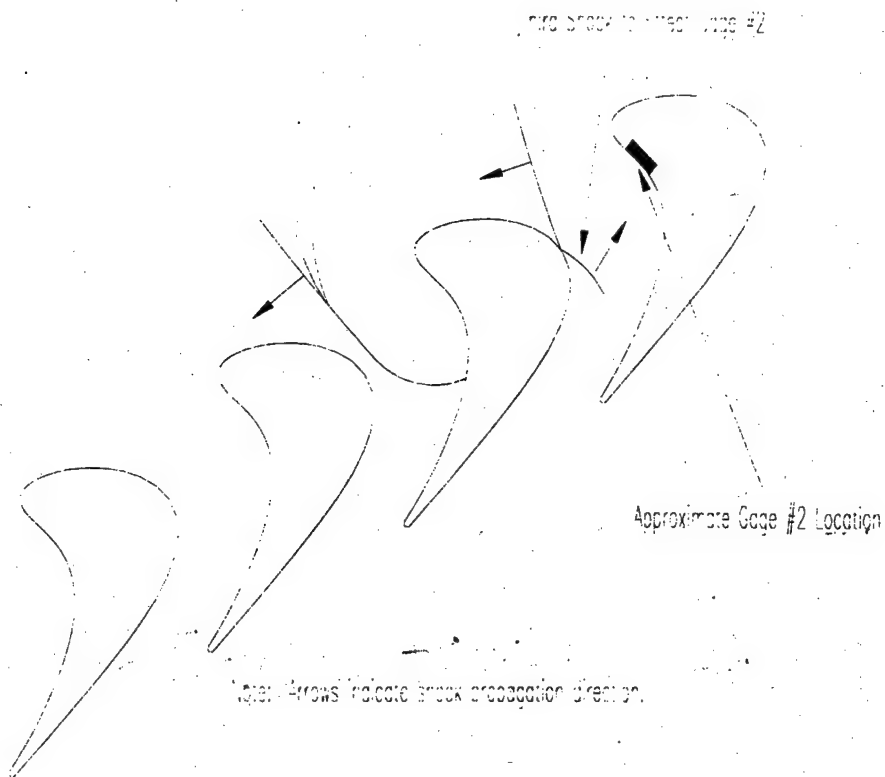Figure C.4 Illustration of Second Shock Affecting HFM-6 Gage #2

Third Shock to affect Gage #2

Approximate Gage #2 Location

Lighter Arrows Indicate Shock Propagation Direction

Figure C.5  Illustration of Third Shock Affecting HFM-6 Gage #2

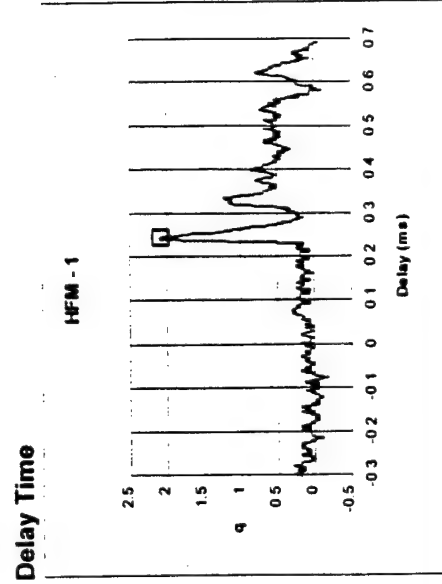# Effects of Shock Wave Passing on Turbine Blade Heat Transfer
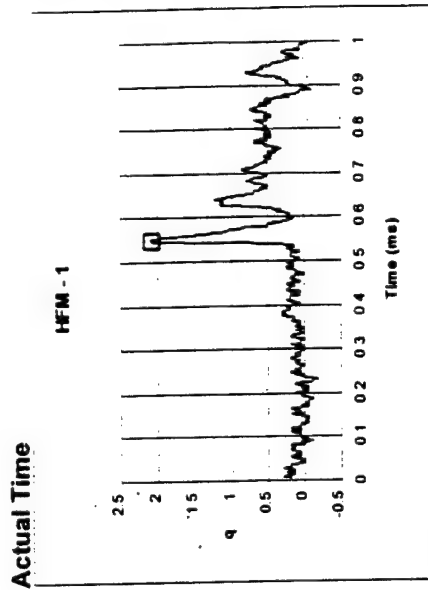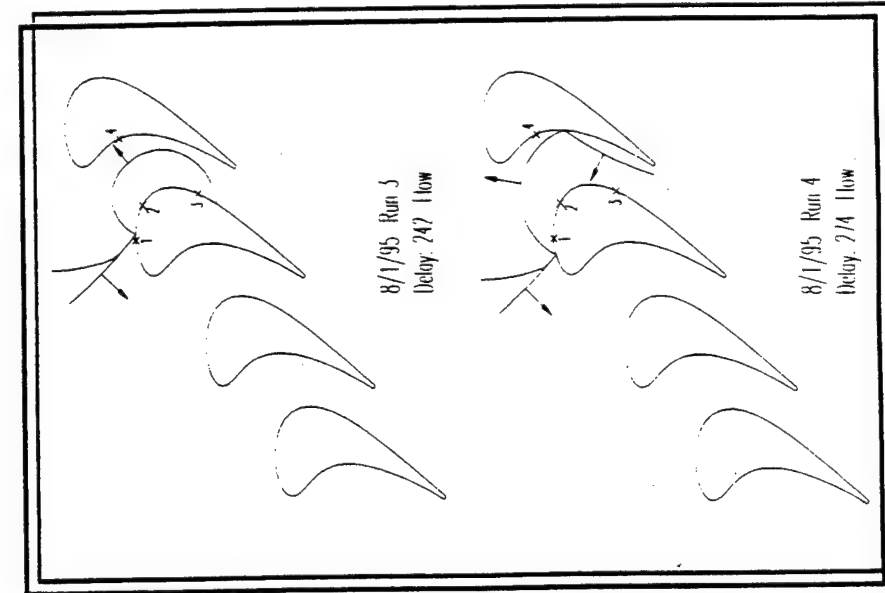
Presented by:

Hume Peabody

Andrew Nix

AFOSR Research Group
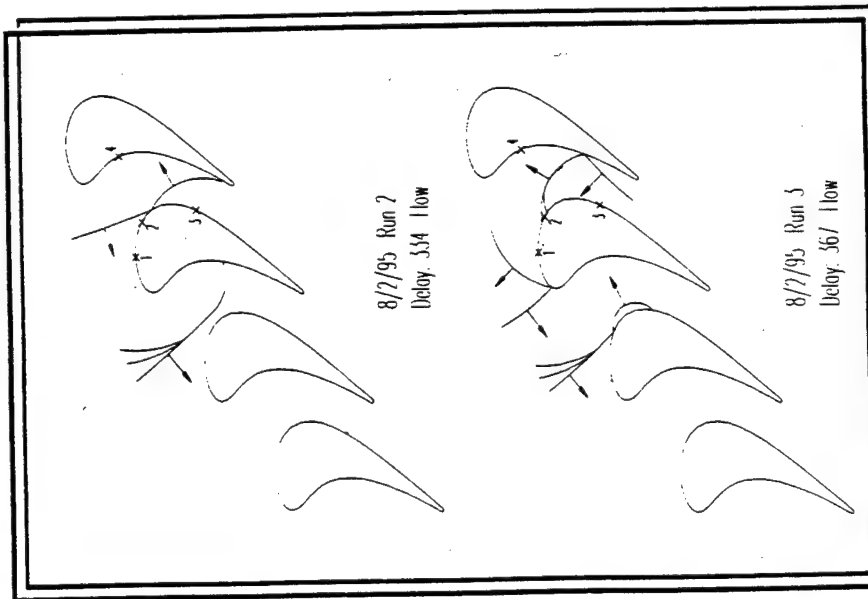
Department of Mechanical Engineering

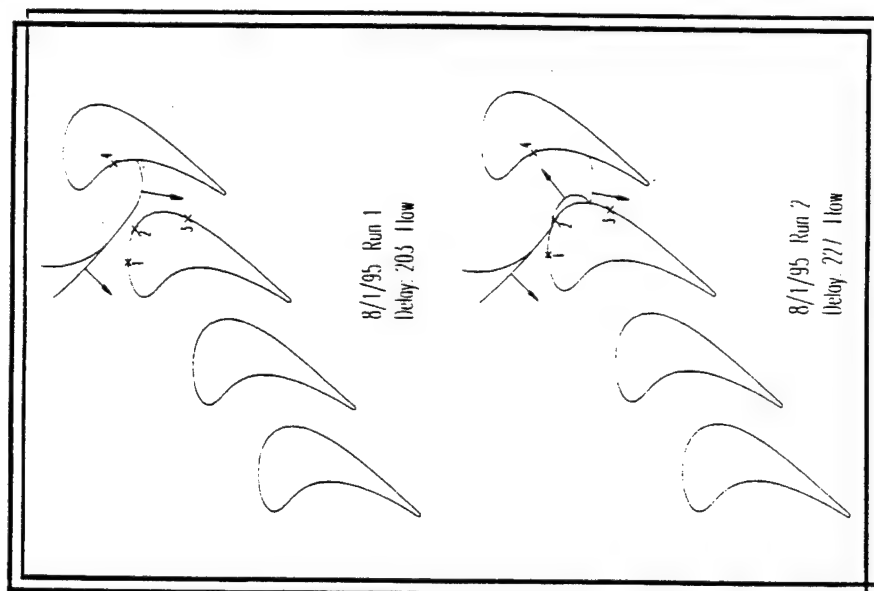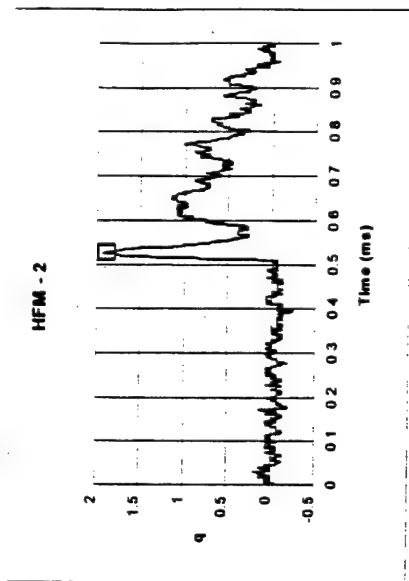Virginia Polytechnic Institute and State University

June 6, 1996

# Gage 1 - Peak 1
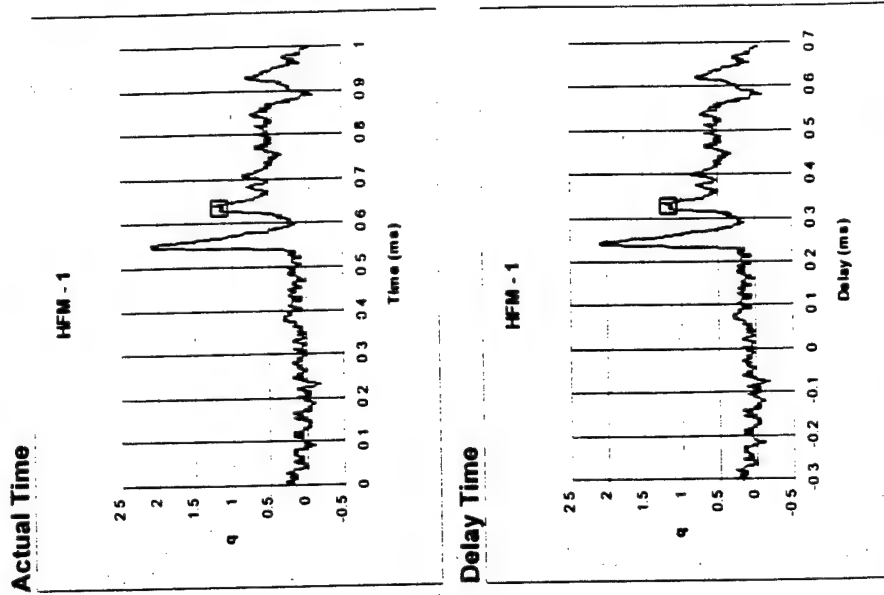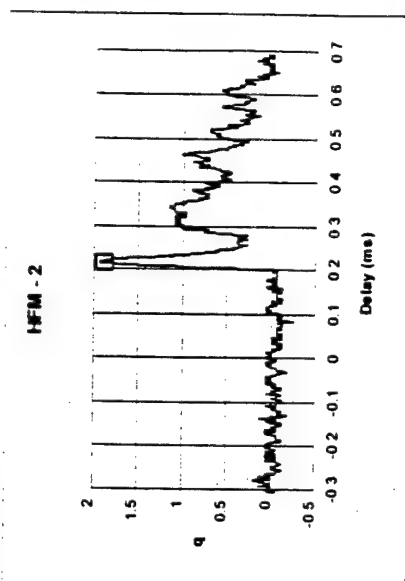


**Actual Time**

HFM - 1

**Delay Time**

HFM - 1



8/1/95 Run 3
Delay: 242 Flow

8/1/95 Run 4
Delay: 274 Flow

# Gage 1 - Peak 2

**Actual Time**

HFM - 1

Time (ms)

**Delay Time**

HFM - 1

Delay (ms)

8/2/95 Run 2
Delay: 5.54  Flow

8/2/95 Run 3
Delay: 56/  Flow

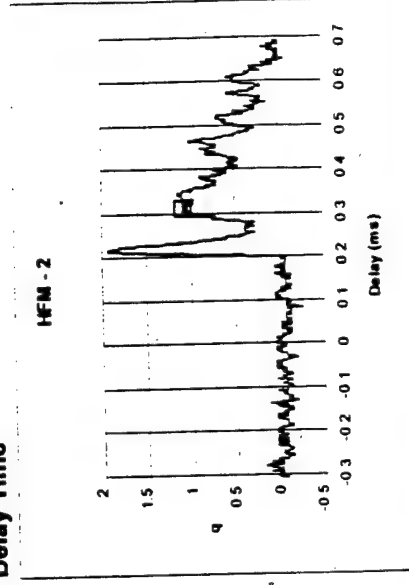# Gage 2 - Peak 1

# Gage 2 - Peak 2

**Actual Time**



HFM - 2

Time (ms)

**Delay Time**

HFM - 2

Delay (ms)

8/2/95 Run 2
Delay .334 Flow

8/2/95 Run 3
Delay .56/ Flow

# Gage 3 - Peak 1



**Actual Time**

HFM - 3

Time (ms)

**Delay Time**

HFM - 3

Delay (ms)

8/1/95 Run 2
Delay 22/ flow

8/1/95 Run 5
Delay 74/ flow

Gage 3 - Peak 2

**Actual Time**

HFM - 3

Time (ms)

**Delay Time**

HFM - 3

Delay (ms)

8/1/95 Run 4
Delay: 2/4 flow

8/2/95 Run 1
Delay: 313 flow

# Gage 3 - Peak 3

**Actual Time**



HFM - 3

**Delay Time**



HFM - 3



8/2/95  Run 3
Delay: 36/  1low
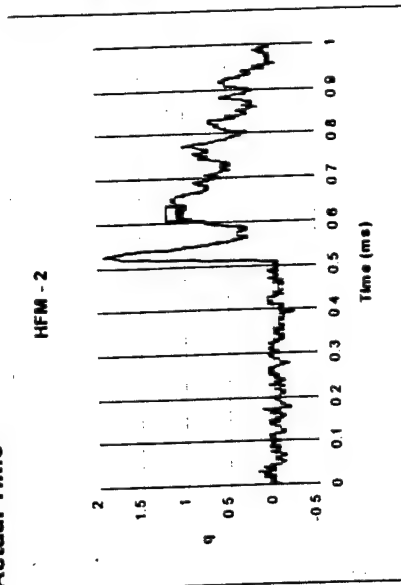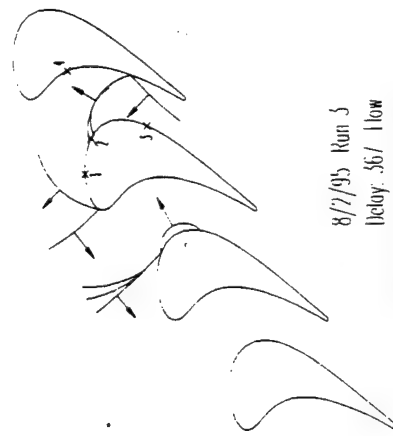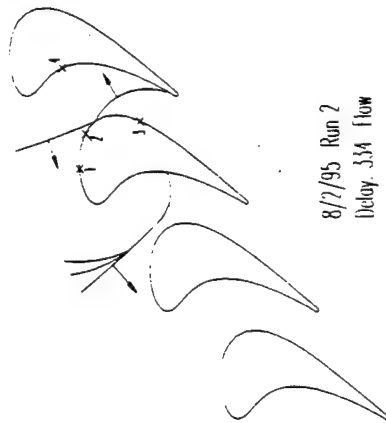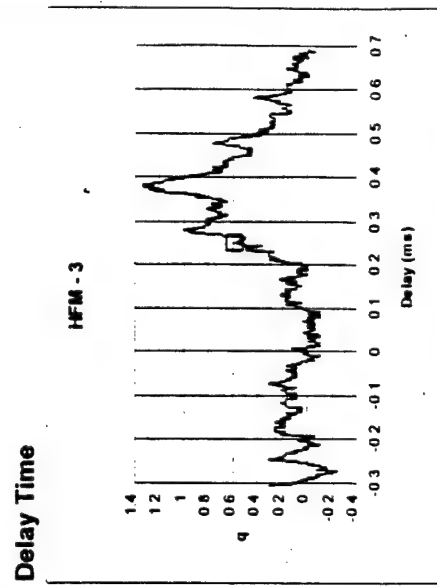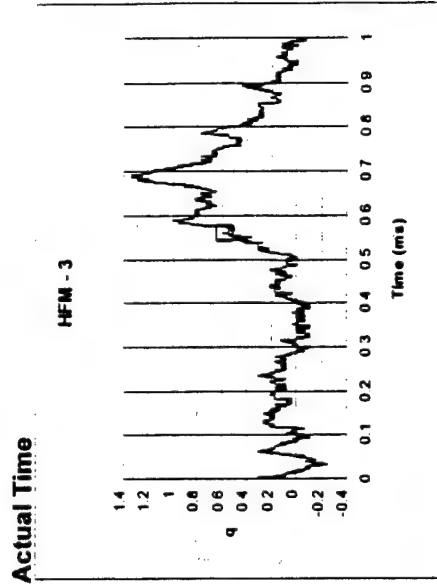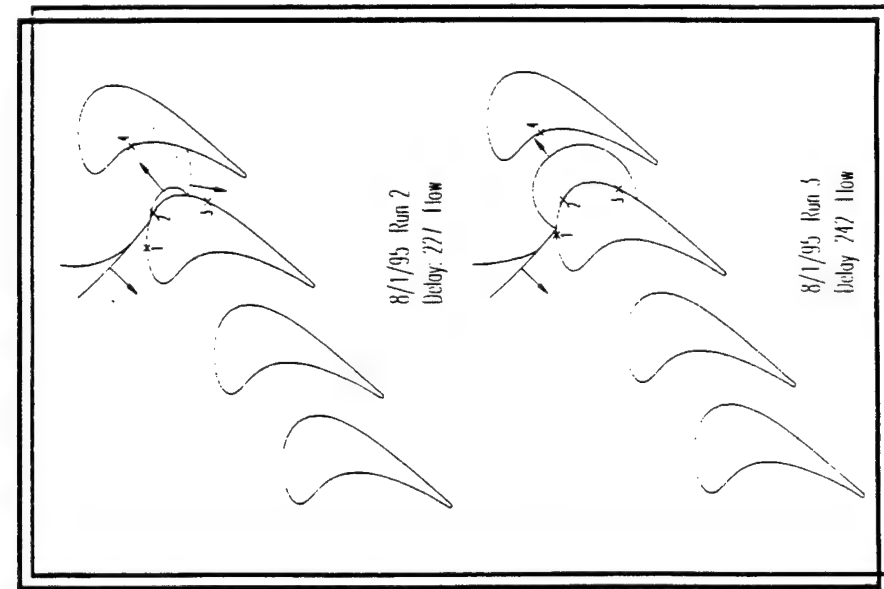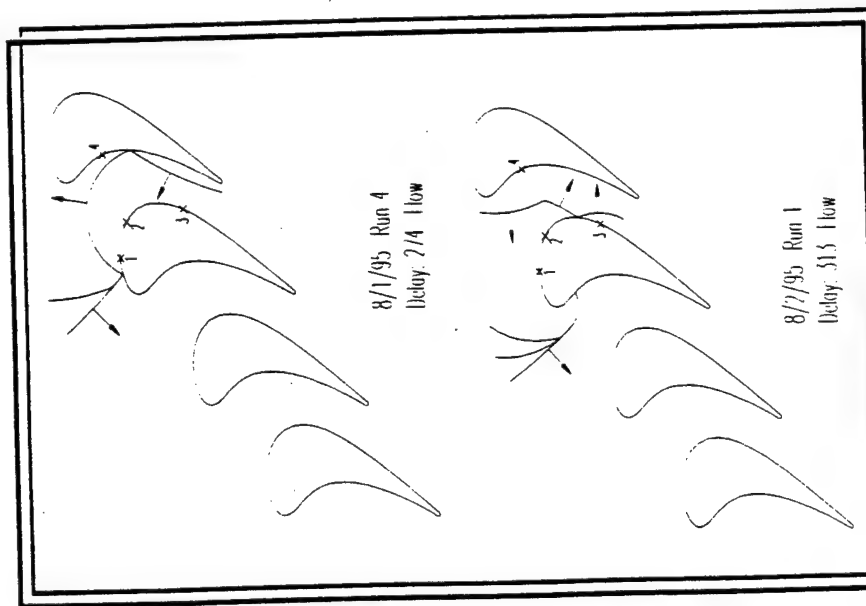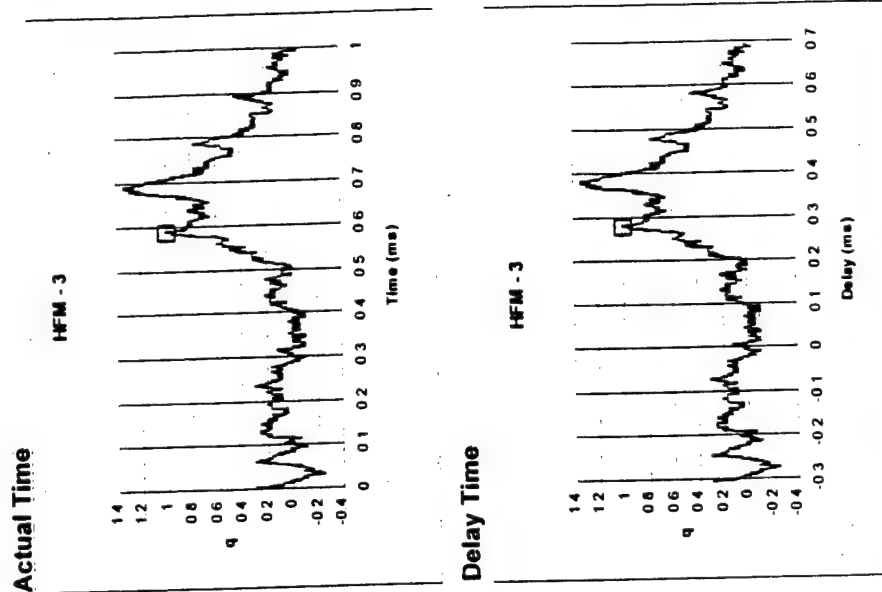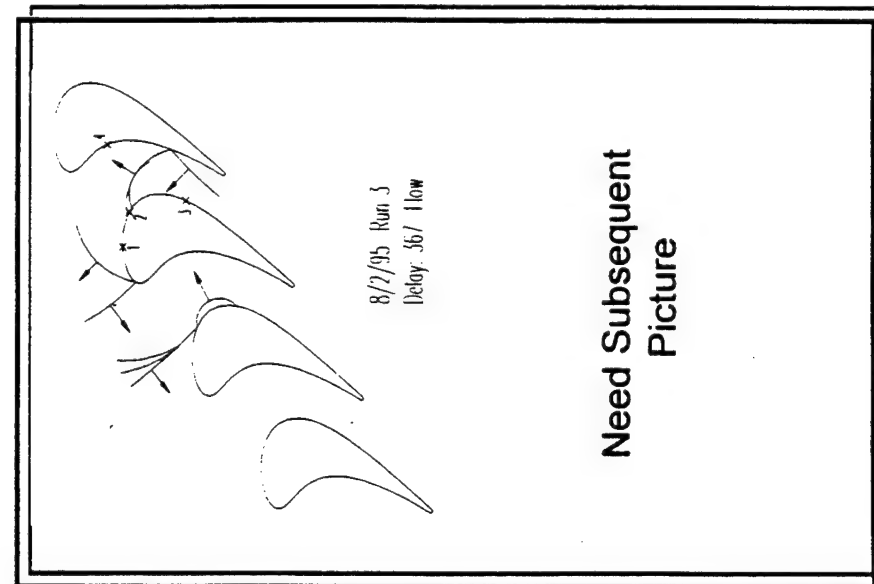
**Need Subsequent
Picture**

Gage 4 - Peak 1

# Gage 4 - Peak 2

**Actual Time**

HFM - 4

**Delay Time**

HFM - 4

**Need Intermediate Picture**

8/1/95 Run 4
Delay: 274 flow

8/2/95 Run 1
Delay: 313 flow

# Gage 4 - Peak 3

**Actual Time**



HFM - 4

**Delay Time**



HFM - 4

8/7/95 Run 3
Delay: 367 flow
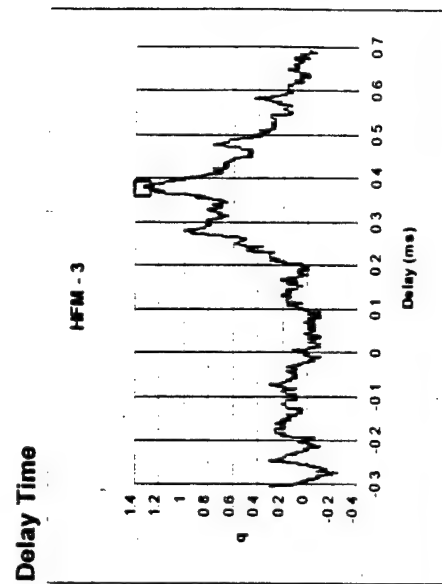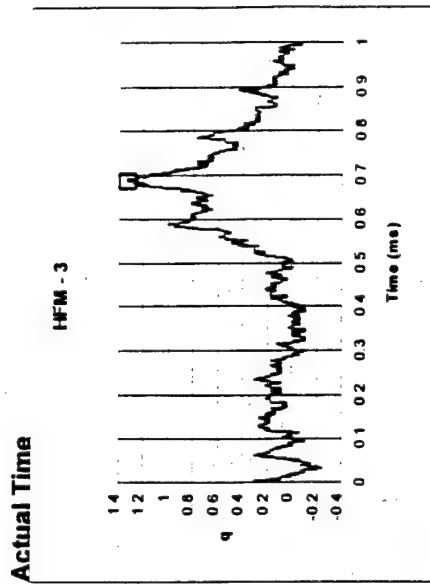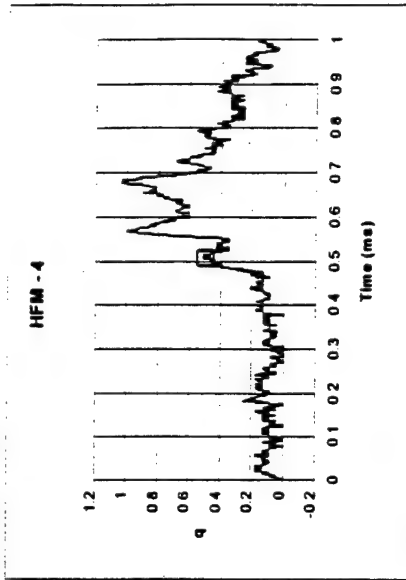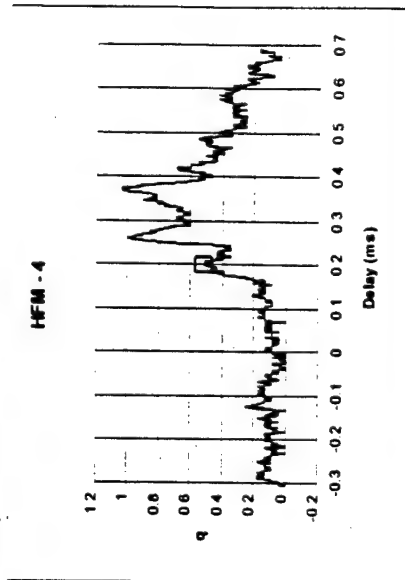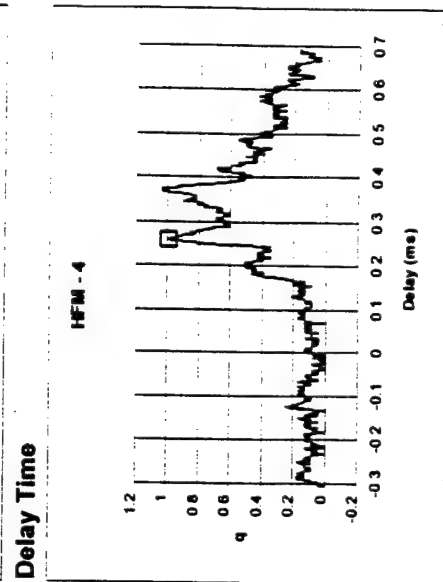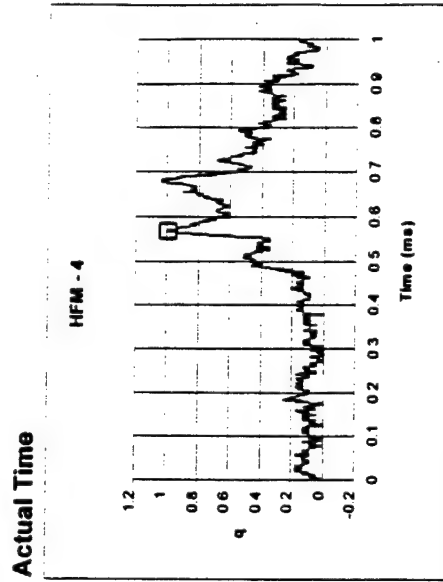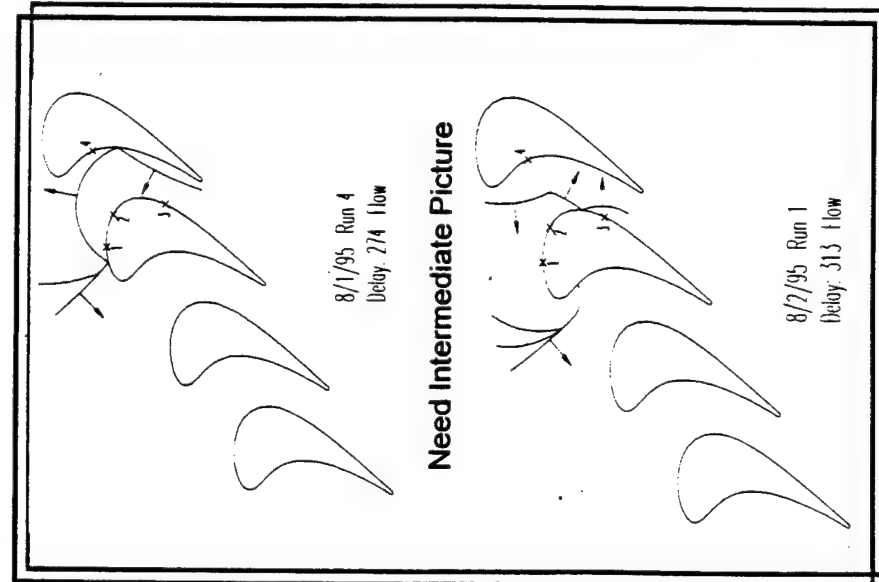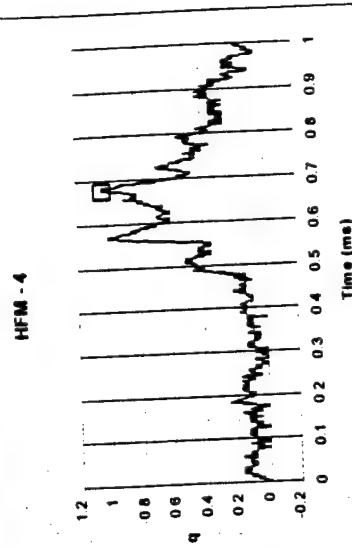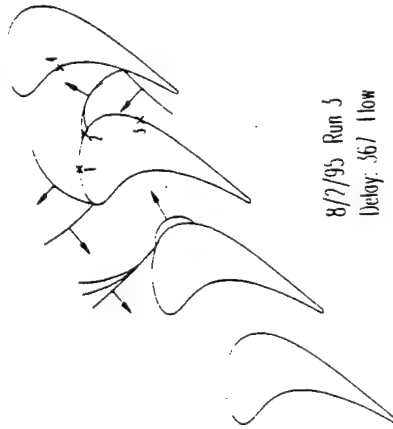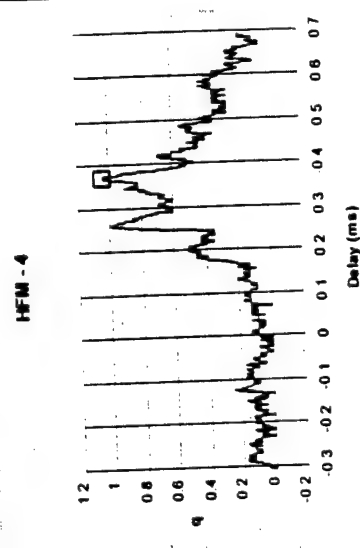
**Need Subsequent Picture**

SHOCK PROGRESSION

8/1/95 Run 3
Delay 242 Flow

8/2/95 Run 4
Delay 525.? Flow

8/2/95 Run 3
Delay 567 Flow

8/1/95 Run 2
Delay 221 Flow

8/2/95 Run 1
Delay 313 Flow

8/2/95 Run 2
Delay 334 Flow

8/1/95 Run 1
Delay 203 Flow

8/1/95 Run 4
Delay 274 Flow
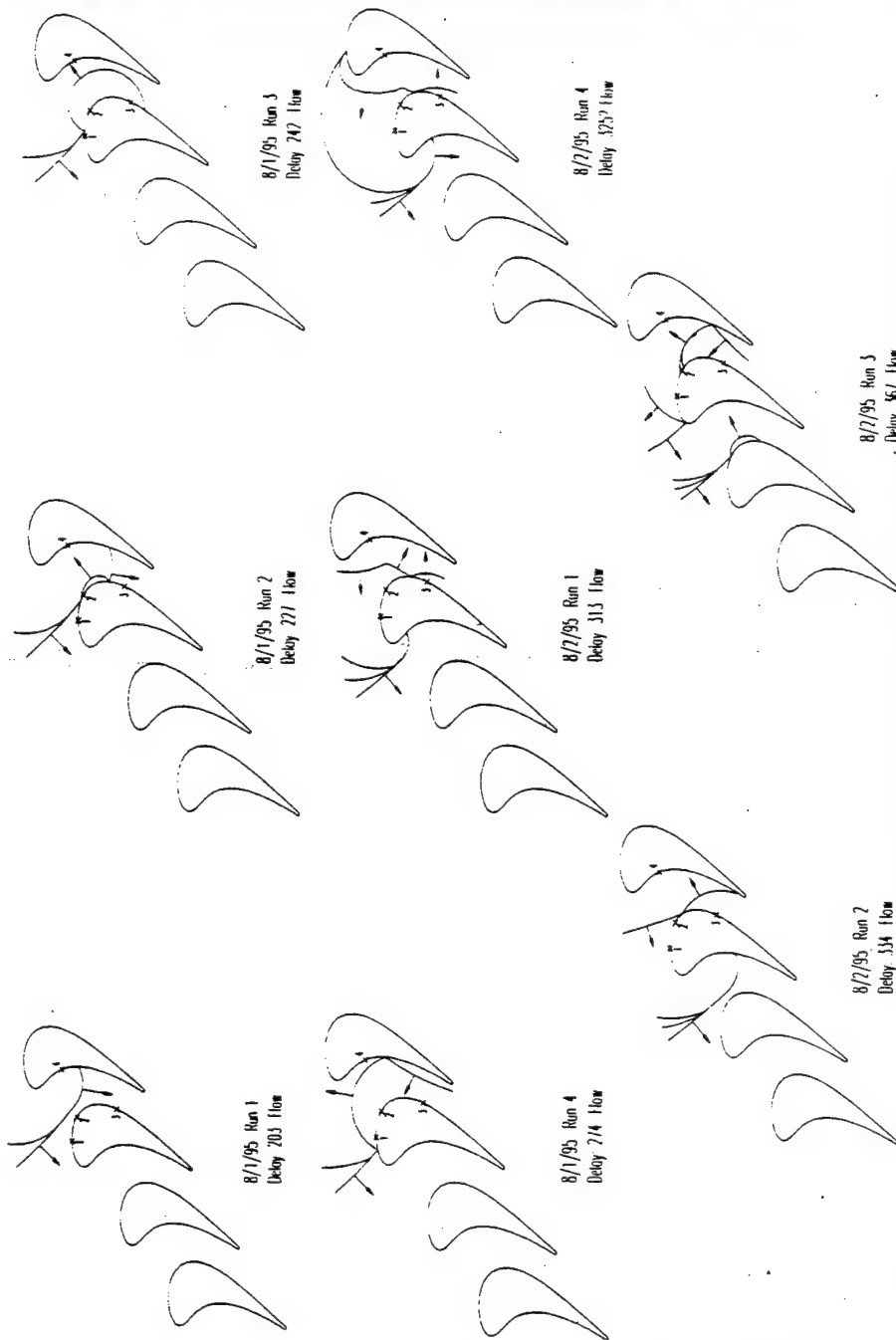
# Appendix D

## FORTRAN Programs

This appendix contains the FORTRAN program(s) used in the shock heat transfer data analysis section. The program(s) contained are as follows:

1. **RESP2REV.FOR**

# RESP2REV.FOR

```
C--------------------------------------------------------------------------------- C
C   Hume Peabody, 1995.                                                            C
C                                                                                  C
C  THIS PROGRAM READS FROM AN INPUT FILE AND MODELS THE INPUT AS A                 C
C  FIRST ORDER TIME RESPONSE (I.E. 1-E^(t/T))  THE INPUT IS A MODEL                C
C  REPRESENTING THE EFFECTS OF A SHOCK ON HEAT TRRASFER.  IT REPRESENTS C
C  A TANGENTIALLY PASSING SHOCK AS THE RESPONSE OF MANY SMALLER                    C
C  RECTANGULAR, EQUALLY WEIGHTED PIECES.  THE USER MUST INPUT THE                  C
C  INPUT AND OUTPUT FILENAMES, THE NUMBER OF POINTS, AND THE TIME                  C
C  CONSTANT AS WELL AS WHETER TO REPRESENT A NORMAL OR TANGENTIAL                  C
C  SHOCK.                                                                          C
C                                                                                  C
C--------------------------------------------------------------------------------- C

      REAL S,QINP(2050),QGAG(2050), QCALC(2050),QTAN(2050),INIT,DT
      INTEGER TIMEF,counter, time(2050)
      character inp*12, outp*12, choice1*1, tstch*1, SHOCK*1
      PARAMETER (PI=3.141592654)


      write(*,*)'enter the data file name.'
      read(*,11) inp
      write(*,*)'enter the desired output file name'
      read(*,11) outp
11    format(a12)
      write(*,*)'enter the number of data points to use up to 2100'
      read(*,13) counter
13    format(i4)
      write(*,*)'enter the value of time constant'
      read*, T
      write(*,*)'normal or tangential shock? (n/T)'
12    format(a1)
      read(*,12) shock

      inittemp=0.0

      OPEN (9, FILE = inp)

* READS INPUT FILE AND STORES DATA

      S=1.
      TIMEF = counter
      DO 1 I = 1, TIMEF
        READ (9, 1000) TIME(I), QINP(I), QGAG(I)
1000    FORMAT(I8,1X,F8.6,F9.7)
        QINP(I) = QINP(I)*S
        IF (I.EQ.1) INIT=TIME(1)
```

```
        TIME(I)=TIME(I)-INIT
1    CONTINUE

     DT=TIME(2)-TIME(1)

* CALCULATES 1-e^t/T ADJUSTMENT

     DO 2 M = 1, TIMEF
       QCALC(M) = 0.
       DO 3 L = 2, M
       QCALC(M)=QCALC(M)+(QINP(L)-QINP(L-1))*(1.-EXP(-(M-L)*DT/T))
3    CONTINUE
2    CONTINUE

* ADJUSTS FOR TANGENTIAL PASSING OVER GAGE SURFACE

     IF ((SHOCK.EQ.'T').OR.(SHOCK.EQ.'t')) THEN

       QTAN(1) = QCALC(1)*.05
       DO 10 K=2,TIMEF
         SUM = 0
         IF (K.LE.15) THEN
           DO 15 J=1,K
           SUM=SUM + QCALC(J)*0.05
15         CONTINUE
           QTAN(K) = SUM
         ELSE
           DO 16 J=1,15
           SUM=SUM + QCALC(K+J-15)*.05
16         CONTINUE
           QTAN(K) = SUM
         ENDIF
10   CONTINUE
     END IF

* WRITES OUTPUT FILE

     OPEN (6, FILE = OUTP)
     DO 4 N = 1, TIMEF
       IF ((SHOCK.EQ.'N').OR.(SHOCK.EQ.'n')) THEN
20       FORMAT (I3,1X,F9.7,1X,F9.7,1X,F10.7)
         WRITE (6,20) TIME(N),QINP(N),QGAG(N),QCALC(N)
       ELSE
21       FORMAT (I3,1X,F9.7,1X,F9.7,1X,F10.7,1X,F10.7)
         WRITE (6,21) TIME(N),QINP(N),QGAG(N),QCALC(N),QTAN(N)
       END IF
4    CONTINUE

     STOP
     END
```

# Vita

Andrew Nix was born in Ankara, Turkey in an American military hospital on July 4, 1972. He lived with his family while his father was stationed at several military assignments in Arizona, Pennsylvania, and Germany before settling in Smithsburg, Maryland where he went to middle and high school. Growing up near the Potomac River and the Blue Ridge Mountains, the author has developed a love for fishing and a great appreciation for nature and the outdoors. After graduating from Smithsburg High School in June, 1990, he began his undergraduate studies in Mechanical Engineering at the University of Maryland, Baltimore County that Fall. He worked as an undergraduate for four years as an Atmospheric Scientist/Engineering Technician for Versar, Inc., an environmental consulting firm in Columbia, MD. He received his Bachelor of Science in Engineering in the Spring of 1995, graduating summa cum laude. The following Fall, he began his graduate studies at the Virginia Polytechnic Institute and State University in Blacksburg, VA as a graduate assistant for Dr. W. F. Ng studying heat transfer in gas turbines. The author defended his work on December 19, 1996, and will be working for Dominion Engineering, Inc. in McLean, VA as an Associate Engineer.

Andrew C. Nix